

**NANOFABRICATION OF METAL/POLYMER  
STRUCTURES FOR SURFACE ENHANCED RAMAN  
SPECTROSCOPY BASED BIOSENSING**

By

**DANIEL ALEJANDRO PÁEZ CORREA**

A thesis submitted in partial fulfillment of the requirements for the degree of

**MASTER OF SCIENCE**

in

**MECHANICAL ENGINEERING**

**UNIVERSITY OF PUERTO RICO  
MAYAGÜEZ CAMPUS**

December, 2009

Approved by:

---

Pedro Quintero, Ph.D  
Member, Graduate Committee

---

Date

---

Jayanta Banerjee, Ph.D  
Member, Graduate Committee

---

Date

---

Rubén Díaz Rivera, Ph.D  
President, Graduate Committee

---

Date

---

Omar Molina Bas, Ph.D  
Representative of Graduate Studies

---

Date

---

Gustavo Gutierrez, Ph.D  
Chairperson of the Department

---

Date

Abstract of MASTER OF SCIENCE Presented to the Graduate School  
of the University of Puerto Rico in Partial Fulfillment of the  
Requirements for the Degree of Master of Science

**NANOFABRICATION OF METAL/POLYMER  
STRUCTURES FOR SURFACE ENHANCED RAMAN  
SPECTROSCOPY BASED BIOSENSING**

By

DANIEL ALEJANDRO PÁEZ CORREA

December 2009

Chair: RUBEN DÍAZ RIVERA

Major Department: MECHANICAL ENGINEERING

Raman spectroscopy is a powerful tool for detection because the Raman spectra yields information about the molecular structure of a given analyte and the technique is commonly used as a molecular fingerprint. However the Raman signal is very weak, making the process inefficient. Surface Enhanced Raman Spectroscopy (SERS), has the advantage of increasing the Raman signal by several orders of magnitude, making the technique very attractive and is becoming increasingly popular in the fields of biotechnology and chemistry. Effective techniques for nanofabrication are essential in SERS, taking into account that the particles sizes conforming the SERS substrate, must be in the range of 5 – 100 nm to exhibit a maximum enhancement, with shape and interparticle spacing affecting its performance. In this project a series of hexagonal, elliptical, and square shaped arrays of nanopillars were produced using electron beam lithography. The nanopillars were patterned in poly(methylmetacrylate), a commonly used electron beam resist. These arrays were used to test their performance as SERS substrates as a result of the different shapes of the nanostructured surface, using the model molecule, 4-aminobenzoic acid

(PABA). The results show that the elliptical-shaped nanopillars gave the maximum SERS signal for a given concentration of PABA, when a 15 nm thick layer of silver was deposited over the nanostructured surface, which was used as the enhanced metal surface.

Resumen de Disertación Presentado a Escuela Graduada  
de la Universidad de Puerto Rico como requisito parcial de los  
Requerimientos para el grado de Maestría en Ciencias

**NANOFABRICACIÓN DE ESTRUCTURAS  
METAL/POLIMERO PARA BIOSENSORES BASADOS  
EN ESPECTROSCOPIA DE RAMAN MEJORADA POR  
SUPERFICIE**

Por

**DANIEL ALEJANDRO PÁEZ CORREA**

Diciembre 2009

Consejero: RUBEN DÍAZ RIVERA  
Departamento: INGENIERIA MECÁNICA

La espectroscopía de Raman es una técnica poderosa de detección, ya que el espectro Raman provee información estructural de cierto analito dado, y la técnica además es comúnmente usada como huella digital de las moléculas. Sin embargo, la señal Raman es débil, lo que hace el proceso ineficiente. La espectroscopía de Raman de superficie, más conocida como SERS por sus siglas en inglés (Surface Enhanced Raman Spectroscopy) tiene la ventaja de incrementar la señal de Raman en varios ordenes de magnitud, haciendo a esta técnica bastante atractiva y se está volviendo cada vez más popular en los campos de biotecnología y química. Técnicas efectivas de nanofabricación son esenciales en SERS, teniendo en cuenta que el tamaño de las partículas que conforman el sustrato para SERS, deben estar en un rango entre 5 – 100nm para que exhiban un incremento máximo en la señal, con la forma y espacio entre partículas afectando también su desempeño. En este proyecto se han fabricado, por medio de Litografía con rayo de Electrones (EBL), una serie de arreglos con nanopilares en forma hexagonal, elíptica, y cuadrada. Los nanopilares fueron

hechos usando el comunmente usado PMMA (polimetilmetacrilato) como material resistivo. Los arreglos fueron usados para probar su desempeño como substratos para SERS, en funcion de las diferentes formas geometricas de las nanoestructuras en la superficie, utilizando como molecula de prueba 4 ácido aminobenzoico (PABA). Los resultados muestran que los pilares con forma elíptica dieron la máxima señal de SERS para una concentración dada de PABA, cuando una capa de 15 nm de plata fue depositada sobre la superficie nanoestructurada, la cual fue usada como la superficie de mejoramiento de la señal de Raman.

Copyright © 2009

by

DANIEL ALEJANDRO PÁEZ CORREA

I dedicate this thesis to God, my essence and inspiration. without Him, this work would have not been possible.

To my parents for their infinite love, guidance and unconditional support, making possible all my achievements.

To my brothers, which have been an example to follow, and for always been there.

To Ruth Hidalgo, who was an inexhaustible source of support necessary for the realization of this thesis.

## ACKNOWLEDGMENTS

I want to acknowledge the support and guidance provided by my advisor Rubén Díaz, who was always at the forefront of this project. I want to thank Professor Marcos De Jesús and graduate student Jenifer Olavarria from the Chemistry Department of the University of Puerto Rico at Mayaguez, for their help which was always available when needed. My acknowledgements go also to the members of my graduate committee, Pedro Quintero and Jayanta Banerjee, for their valuable recommendations for the proper structuring of this thesis. This material is based upon work supported by the Institute for Functional Nanomaterials (IFN) and the Bio Science and Engineering Initiative (BioSEI)

## TABLE OF CONTENTS

	<u>page</u>
ABSTRACT ENGLISH . . . . .	ii
ABSTRACT SPANISH . . . . .	iv
ACKNOWLEDGMENTS . . . . .	viii
LIST OF TABLES . . . . .	xi
LIST OF FIGURES . . . . .	xii
<b>1 INTRODUCTION . . . . .</b>	<b>1</b>
1.1 Motivation . . . . .	2
1.2 Objectives and Tasks . . . . .	3
1.3 Theoretical Background . . . . .	3
1.3.1 The Raman Effect . . . . .	3
1.3.2 Raman Instrumentation . . . . .	10
1.4 The SERS Effect . . . . .	15
1.4.1 SERS Enhancement Mechanism . . . . .	16
1.5 Review of SERS Substrates . . . . .	23
1.6 Structure of Thesis . . . . .	27
<b>2 ELECTRON BEAM LITHOGRAPHY BASICS . . . . .</b>	<b>28</b>
2.1 Lithography . . . . .	28
2.2 Types of Lithography . . . . .	29
2.2.1 Optical Lithography . . . . .	29
2.2.2 X-ray Lithography . . . . .	30
2.3 Introduction to Electron Beam Lithography . . . . .	31
2.3.1 Electron Optics . . . . .	33
2.3.2 Electron-Solid Interaction: Proximity Effect . . . . .	40
2.3.3 Proximity effect correction . . . . .	41
2.3.4 Writing Strategies . . . . .	43
2.3.5 Exposure Parameters . . . . .	44
2.3.6 Nanometer Pattern Generation System . . . . .	47
2.4 Resists . . . . .	48
2.4.1 Positive Resists . . . . .	50
2.4.2 Negative Resists . . . . .	52
2.5 Pattern Processing . . . . .	53
2.5.1 Coating and Lift Off . . . . .	53

	2.5.2	Sputtering . . . . .	54
	2.5.3	Evaporation . . . . .	55
3		EBL NANOFABRICATION OF PROPOSED METAL/POLYMER SUB- STRATES FOR SERS . . . . .	57
	3.1	Materials . . . . .	57
	3.2	Experimental procedure . . . . .	57
	3.2.1	PMMA Spin Coating . . . . .	57
	3.2.2	Patterns Design and Processing . . . . .	59
	3.2.3	Microscope optimization . . . . .	63
	3.2.4	Exposure Details . . . . .	66
	3.2.5	PMMA Developing . . . . .	68
	3.3	EBL patterns results . . . . .	68
	3.3.1	Patterns Observation . . . . .	75
4		Raman Spectra Acquisition Using Proposed SERS Substrates . . . . .	84
	4.1	Materials and Methods . . . . .	86
	4.1.1	Thin Film Silver Evaporation . . . . .	87
	4.2	SERS Results . . . . .	88
	4.2.1	Study with Hexagonal Patterns . . . . .	89
	4.2.2	Study with Square Patterns . . . . .	92
	4.2.3	Study with Elliptical Patterns . . . . .	95
	4.2.4	Nanostructures Shape Comparison . . . . .	100
	4.3	Discussion . . . . .	100
5		CONCLUSIONS AND FUTURE WORKS . . . . .	103
	5.1	Conclusions . . . . .	103
	5.2	Future Work . . . . .	104

LIST OF TABLES

<u>Table</u>		<u>page</u>
2-1	Properties of the electron sources commonly used in electron beam lithography[35]. . . . .	37
3-1	Final dose requirements for hexagons and squares. . . . .	71
3-2	Final dose requirements for ellipses. . . . .	72
3-3	Final dose requirements for different elliptical configurations. . . . .	72
3-4	Final dose requirements for stars and triangles. . . . .	73
3-5	Final dose requirements for rectangles. . . . .	73

## LIST OF FIGURES

<u>Figure</u>	<u>page</u>
1-1 <b>Energy level diagram describing the Rayleigh (A), Stokes Raman scattering (B), and anti-Stokes Raman scattering (C) processes.</b> [9] . . . . .	7
1-2 <b>Raman Spectrum of CCl<sub>4</sub> (488.0 nm excitation)</b> [9] . . . . .	9
1-3 Schematic diagram of the major components in a Raman Spectrometer.	11
1-4 <b>Top:light polarized perpendicular to the interparticle axis. Bottom:light polarized parallel to the interparticle axis</b> [15]	20
1-5 E-field enhancement contours external to monomers with different shapes. a) and b) are the E-field enhancement contours external to a triangular prism polarized along the two different primary axes, c) and d) are the E-fields enhancement contours for a rod and spheroid polarized along their long axes. The arrows show where is the maximum E-field[16]. . . . .	22
1-6 E-field enhancement contours external dimer of Spheres(top), head to head triangles configuration(middle) and head to tail triangles configuration(bottom)[16]. . . . .	24
2-1 Basic photolithography steps. . . . .	30
2-2 Block diagram showing the major components of a typical EBL system[36] . . . . .	33
2-3 Components of a typical SEM column[37] . . . . .	34
2-4 A)Electrostaic lens configuration. B)Magnetic lens configuration. . . .	38
2-5 Monte Carlo simulation of electron scattering in resist on a silicon substrate at a) 10 kV and b) 20 kV[36]. . . . .	41
2-6 Schematic showing how the GHOST technique can be used to correct for the proximity effect. The top curves show the energy distribution in the resist for a group of seven lines from the primary exposure and from the GHOST exposure. The bottom curve is the resulting final energy distribution, showing the dose equalization for all the lines.[36] . . . . .	43

2-7	Typical electron beam writing strategies . . . . .	44
2-8	Exposure condition for EBL direct writing[39]. . . . .	45
2-9	Definition of dose for area, line and dot exposure.[39] . . . . .	46
2-10	Film thickness versus exposure dose for (a) positive and (b) negative resist. Contrast is defined as the slope of the linear portion of the falling (or rising) section of the curve [37]. . . . .	49
2-11	(a) Is a schematic representation of the sputtering process and (b) shows a cross section view of a pattern after sputtering coating[41].	55
2-12	(a) Shows a schematic of a filament-style evaporation process; a boat is similar except that the sample is above the source material; and (b) shows a cross section view of the pattern after it has been coated using evaporation[41]. . . . .	56
3-1	950K (A) and 495K (B) PMMA thickness vs rpm curve. . . . .	58
3-2	Design CAD drawing of University of Puerto Rico at Mayaguez seal (left) and a SEM image of the lithographically defined pattern on PMMA (right). . . . .	60
3-3	Hexagons design for EBL writing. . . . .	61
3-4	Sequence of the ellipses design for EBL writing. A shape modification was utilized to make the patterns. . . . .	62
3-5	Run file configuration. All parameters are introduced here to make the EBL writing. . . . .	63
3-6	Scratch made on the polymer substrate to take as reference point. . .	64
3-7	Example of a spot continuation for a non optimized beam (A) and a focused beam with astigmatism correction (B). . . . .	65
3-8	A)Pattern that shows the effect os astigmatism. B) Pattern performed by a well optimized beam. . . . .	66
3-9	Square patterns design for 150nm in features gap. The yellow lines are assigned a dose, and the red ones are assigned a different dose to develop away the gap between the squares. . . . .	67
3-10	Rectangles design. The top line is set to a different color to change the dose. . . . .	68
3-11	Honey Comb patten writen with a beam current of 25pA . . . . .	69

3-12	Sequence of the hexagonal pattern optimization.	
	.....	70
3-13	Field of hexagons written with a bilayer system.	74
3-14	Difference in patterns adhesion at a baking time of 90s (A) and 180s (B).	74
3-15	Hexagons with 50nm in spacing	75
3-16	Hexagons with 100nm in spacing	76
3-17	Hexagons with 150nm in spacing	76
3-18	Hexagons with 200nm in spacing	77
3-19	Squares with 50nm in spacing	77
3-20	Squares with 100nm in spacing	78
3-21	Squares with 150nm in spacing	78
3-22	Squares with 200nm in spacing	79
3-23	Ellipses 3:1 with 50nm in spacing	79
3-24	Ellipses 4:1 with 100nm in spacing	80
3-25	Ellipses 4:1 with 150nm in spacing	80
3-26	Ellipses 4:1 with 200nm in spacing	81
3-27	Ellipses 5:1 with 150nm in spacing	81
3-28	Ellipses 5:1 with 200nm in spacing	82
3-29	Stars with 50nm in spacing	82
3-30	Triangles with 50nm in spacing	83
3-31	rectangles 2:1 with 50nm in spacing	83
4-1	Rayleigh and Raman bands of solid naphthalene excited with a 632.8nm line [9].	85
4-2	Raman spectrum of PABA in solid state. The inset shows the molecular structure of the substance.	86
4-3	Picture of the EDWARDS FL 400/AUTO 306 Physical Vapor Deposition (PVD) system used to evaporate silver over the nanostructured polymer.	88

4-4	Effect of the dose used for the hexagonal pattern fabrication on the $411\text{cm}^{-1}$ band signal of PABA ( $1 \times 10^{-4}\text{M}$ ). The silver layer thickness corresponding to these intensities is 15nm. . . . .	90
4-5	Raman spectra of PABA acquired using the Hexagons array fabricated with a dose of $0.45\text{nC/cm}$ . The excitation line used was 785nm with a silver layer thickness of 15nm. . . . .	91
4-6	Raman spectra of PABA acquired using the Hexagons array fabricated with a dose of $0.35\text{nC/cm}$ . The excitation line used was 785nm with a silver layer thickness of 15nm. . . . .	91
4-7	Effect of the dose used for the square pattern fabrication on the $411\text{cm}^{-1}$ band signal of PABA ( $1 \times 10^{-4}\text{M}$ ). The silver layer thickness corresponding to these intensities is 15nm. . . . .	93
4-8	Effect of the dose used for the square pattern fabrication on the $411\text{cm}^{-1}$ band signal of PABA ( $1 \times 10^{-4}\text{M}$ ). The silver layer thickness corresponding to these intensities is 25nm. . . . .	94
4-11	Raman spectra of PABA acquired using the Squares array fabricated with a dose of $0.5\text{nC/cm}$ . The excitation line used was 785nm with a silver layer thickness of 25nm. . . . .	94
4-9	Raman spectra of PABA acquired using the Squares array fabricated with a dose of $0.5\text{nC/cm}$ . The excitation line used was 785nm with a silver layer thickness of 15nm. . . . .	95
4-10	Raman spectra of PABA acquired using the Squares array fabricated with a dose of $0.45\text{nC/cm}$ . The excitation line used was 785nm with a silver layer thickness of 15nm. . . . .	96
4-12	Effect of the dose used for the elliptical pattern fabrication on the $411\text{cm}^{-1}$ band signal of PABA ( $1 \times 10^{-4}\text{M}$ ). The silver layer thickness corresponding to these intensities is 15nm. . . . .	96
4-13	Effect of the dose used for the elliptical pattern fabrication on the $411\text{cm}^{-1}$ band signal of PABA ( $1 \times 10^{-4}\text{M}$ ). The silver layer thickness corresponding to these intensities is 25nm. . . . .	97
4-14	Effect of the dose used for the elliptical pattern fabrication on the $411\text{cm}^{-1}$ band signal of PABA ( $1 \times 10^{-4}\text{M}$ ). The silver layer thickness corresponding to these intensities is 35nm. . . . .	97
4-15	Influence of the deposited layer thickness over the elliptical nanostructures on the SERS intensity of the $411\text{cm}^{-1}$ present in PABA. . . . .	98

4-16 Raman spectra of PABA acquired using the elliptical array fabricated with a dose of 0.35nC/cm . The excitation line used was 785nm with a silver layer thickness of 15nm. . . . .	99
4-17 Raman spectra of PABA acquired using the elliptical array fabricated with a dose of 0.35nC/cm . The excitation line used was 785nm with a silver layer thickness of 25nm. . . . .	99
4-18 Influence of the nanostructures shape on the SERS intensity of the 411cm <sup>-1</sup> present in PABA. The silver layer thickness is 15nm. . . .	101
5-1 Nanostructures with triangles and cluster like particles configuration .	105
5-2 Ellipses arrange in a circular array . . . . .	105
5-3 Rectangles arranged in a circular array . . . . .	106

# CHAPTER 1

## INTRODUCTION

Since Raman scattering was first observed by C. V. Raman, this spectroscopic technique is increasingly being used as a material characterization method and a detection tool for molecules, owing to the fact that Raman spectra represent the vibrational frequencies of functional chemical bonds in molecules[1, 2]. This is of particular interest for bio-applications, where specificity of detection is important. However, spontaneous Raman effect is very weak and inefficient, making difficult the process of spectra acquiring. Surface Enhanced Raman Spectroscopy (SERS) has the advantage of greatly increasing Raman scattering[3]. The mechanisms involved in SERS enhancement are nowadays matter of study, but it is generally agreed that two different mechanisms dominate in the phenomenon - a classical electromagnetic effect and a chemical effect[4, 5]. Most studies show a chemical enhancement factor much lower than that of electromagnetic theory[6], being the latter effect the most explored contribution to SERS enhancement. When a metal surface is rough on a nanometric scale, incident light radiation excites resonant surface plasmon that induces

a strong electromagnetic field in the surface, generating a high Raman signal[7]. This roughness consists in a distribution of metal nanoparticles over the surface, being size, geometry, and homogeneous distribution of these metal nanoparticles important variables affecting the substrate sensitivity for SERS[2]. In the present work, Electron Beam Lithography (EBL) is used as the nanofabrication tool to strictly control the aforementioned variables, and test the final substrate performance for SERS.

### 1.1 Motivation

Surface Enhanced Raman Spectroscopy (SERS) is one of the most sensitive tool for molecules detection, and has gained interest in the technique for chemical and biological applications. Substrates play an important role in SERS mechanism, and the development of quantitative, highly sensitive ones requires control over size, shape, and particles interspacing. Despite the fact that SERS has been established as an information-rich spectroscopy for analyte detection, issues of substrates limitations, such as reproducibility and dynamic range, have lagged the general acceptance of SERS for routine analytical applications, and its future development depends critically on techniques for nanofabrication. Lithographic techniques have emerged as promising tools for the fabrication of new substrates with nanoscale patterns.

EBL, ensures the creation of substrates with controlled geometry and interparticle features coupling.

This work presents an optimization of a nanofabrication process for creating sensitive, effective SERS substrates, that would lead to more specific and effective studies in environmental and bioengineering fields.

## **1.2 Objectives and Tasks**

The main objective is the design and fabrication of well-defined metal/polymer nanostructures by employing Electron Beam Lithography to enhance the Raman spectra in SERS.

In order to reach this objective the following tasks will be performed:

- Characterization of PMMA spin coating process.
- Optimization of the photoresist e-beam exposure conditions, in order to get the optimum nanoparticles coupling and dimensions for SERS.
- Implement an effective thin film metal deposition method.
- Test Raman spectra intensity using the nanostructured substrates.

## **1.3 Theoretical Background**

### **1.3.1 The Raman Effect**

When monochromatic light interacts with a molecule, the scattered light consists of two types: Rayleigh scattering and Raman scattering. Rayleigh scattering is strong and has the same frequency as

the incident beam  $\nu_0$ , and the other, Raman scattering, is very weak ( $\sim 10^{-5}$  of the incident beam) and has frequencies  $\nu_0 \pm \nu_m$ , where  $\nu_m$  is a vibrational frequency of a molecule. The  $\nu_0 - \nu_m$  and  $\nu_0 + \nu_m$  lines are called the Stokes and anti-Stokes lines, respectively. Thus, in Raman spectroscopy, we measure the vibrational frequency  $\nu$  as a shift from the incident beam frequency  $\nu_0$ . In contrast to IR spectra, Raman spectra are measured in the UV-visible region where the excitation as well as Raman lines appear. The inelastic collisions in Raman scattering induce an energy-transfer between the incident photons and the molecules of the analyte. The energy of the photons after these events can be expressed as:

$$E_s = h\nu_0 \pm \Delta E_v \quad (1.1)$$

where:

$h$  = the planck's constant

$\nu_0$  = incident light frequency

$\Delta E_v$  = difference in the vibrational energy states.

According to classical theory, Raman scattering can be explained by a wave model that is an extension of a quantum mechanical model. The electric field strength (E) of the electromagnetic wave (laser beam)

fluctuates with time (t) as shown:

$$E = E_0 \cos(2\pi\nu_0 t) \quad (1.2)$$

where  $E_0$  is the vibrational amplitude and  $\nu_0$  is the frequency of the laser. If a diatomic molecule is irradiated by this light, an electric dipole moment  $P$  is induced:

$$P = \alpha E = \alpha E_0 \cos(2\pi\nu_0 t) \quad (1.3)$$

Here,  $\alpha$  is a proportionality constant and is called *polarizability*. If the molecule is vibrating with a frequency  $\nu_0$ , the nuclear displacement  $q$  is written as

$$q = q_0 \cos(2\pi\nu_0 t) \quad (1.4)$$

where  $q_0$  is the vibrational amplitude. For a small amplitude of vibration,  $\alpha$  is a linear function of  $q$ . Thus we can write:

$$\alpha = \alpha_0 + \left( \frac{\partial \alpha}{\partial q} \right)_0 q_0 \quad (1.5)$$

Here,  $\alpha_0$  is the polarizability at the equilibrium position, and  $(\partial \alpha / \partial q)_0$  is the rate of change of  $\alpha$  with respect to the change in  $q$ , evaluated at the equilibrium position.

Combining (1.3) with (1.4) and (1.5), we obtain:

$$\begin{aligned}
P &= \alpha E_0 \cos(2\pi\nu_0 t) \\
&= \alpha_0 E_0 \cos(2\pi\nu_0 t) + \left(\frac{\partial\alpha}{\partial q}\right)_0 q E_0 \cos(2\pi\nu_0 t) \\
&= \alpha_0 E_0 \cos(2\pi\nu_0 t) + \left(\frac{\partial\alpha}{\partial q}\right)_0 q_0 E_0 \cos(2\pi\nu_0 t) \cos(2\pi\nu_m t) \\
&= \alpha E_0 \cos(2\pi\nu_0 t) + \frac{1}{2} \left(\frac{\partial\alpha}{\partial q}\right)_0 q_0 E_0 \\
&\quad [\cos\{2\pi(\nu_0 + \nu_m)t\} + \cos\{2\pi(\nu_0 - \nu_m)t\}] \tag{1.6}
\end{aligned}$$

According to classical theory, the first term represents an oscillating dipole that radiates light of frequency  $\nu_0$  (Rayleigh scattering), while the second term corresponds to the Raman scattering of frequency  $\nu_0 - \nu_m$  (anti-Stokes) and  $\nu_0 + \nu_m$  (Stokes). If  $\left(\frac{\partial\alpha}{\partial q}\right)_0 q$  is zero, the vibration is not Raman-active. Namely, to be Raman-active, the rate of change of polarizability  $\alpha$  with the vibration must not be zero. Figure 1-1 illustrates Raman scattering in terms of a simple diatomic energy level. The incident beam creates a virtual energy state  $\phi_1$  that is a function of the frequency of the laser source. In normal Raman spectroscopy, the exciting line  $\nu_0$  is chosen so that its energy is far below the first electronic excited state[8]. The dotted line indicates a virtual state to distinguish it from the real excited state. The exposure of the sample to this electromagnetic field results in the transition of a fraction of the irradiated molecules from their ground state

to  $\phi_1$ . Once at this virtual state, molecules participate in a series of energy-transfer interactions with the incident photons. In some cases a portion of the energy of the photon is absorbed by the analyte allowing the molecule to return to its first vibrational level. As a result, the scattered photon has less energy than the incident beam resulting in what is known as a Stokes band (Figure 1-1B)[9].

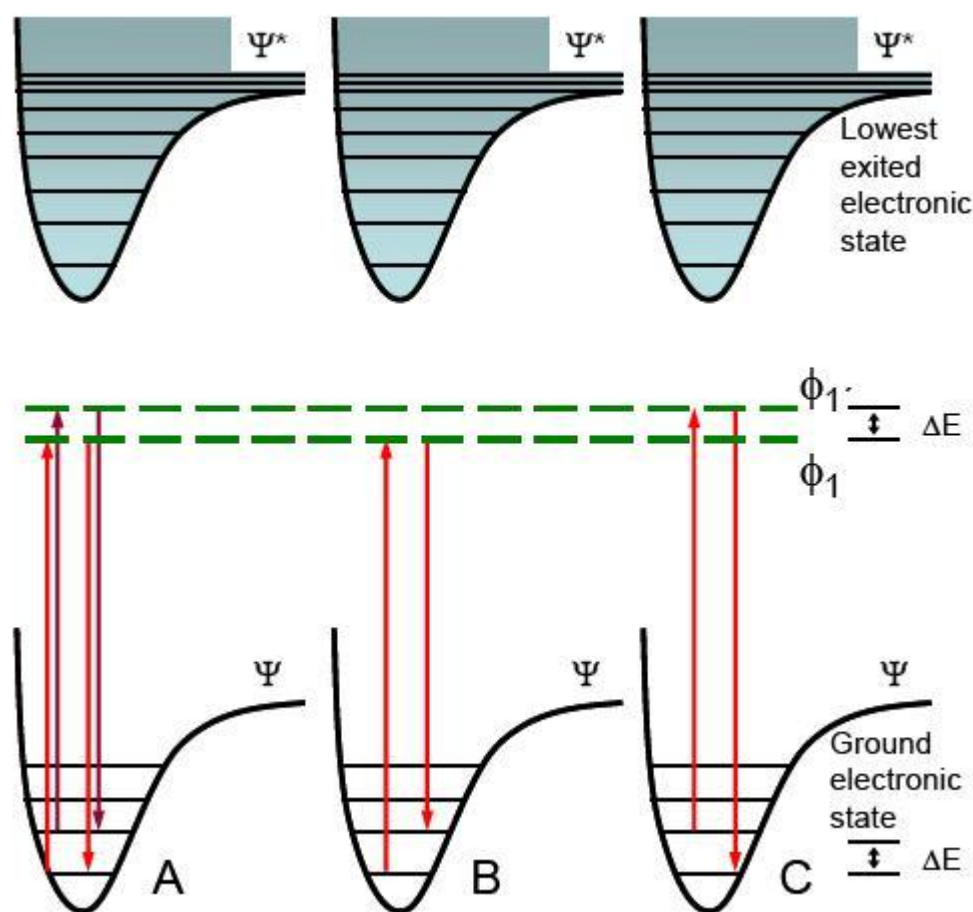


Figure 1-1: Energy level diagram describing the Rayleigh (A), Stokes Raman scattering (B), and anti-Stokes Raman scattering (C) processes.[9]

According to the Boltzmann's distribution (Eq. 1.7), a small fraction of the molecules are at the first vibrational state during the irradiation. Under these conditions, the scattered photons absorb part

of the energy of the molecule, allowing the molecule to return to its ground state. Consequently, the scattered photons are more energetic than the incoming ones, which result in an anti-Stokes band (Figure 1.1 C). From equation 1.7 we can also infer that most of the molecules exist in the ground state. Thus, the Stokes lines are stronger than the anti-Stokes lines under normal conditions. Since both give the same information, it is customary to measure only the Stokes side of the spectrum. Figure 1-2 shows the Raman spectrum of  $CCl_4$ [10].

$$\frac{N_1}{N_2} = \text{Exp} \left[ -\frac{(E_2 - E_1)}{kT} \right] = e^{-(h\nu/kT)} \quad (1.7)$$

Where:

$N_1$  = number of molecules in the lower energy state

$N_2$  = number of molecules in the excited state

$E_1$  = energy of the first state

$E_2$  = energy of the second state

$k$  = Boltzmann's constant

$T$  = Temperature (kelvins)

Equation 1.7 predicts the same intensities for the Stokes and the anti-Stokes bands. A quantum mechanical analysis of the Raman effect shows that the intensity-ratio of these bands is a function of the Boltzmann's distribution:

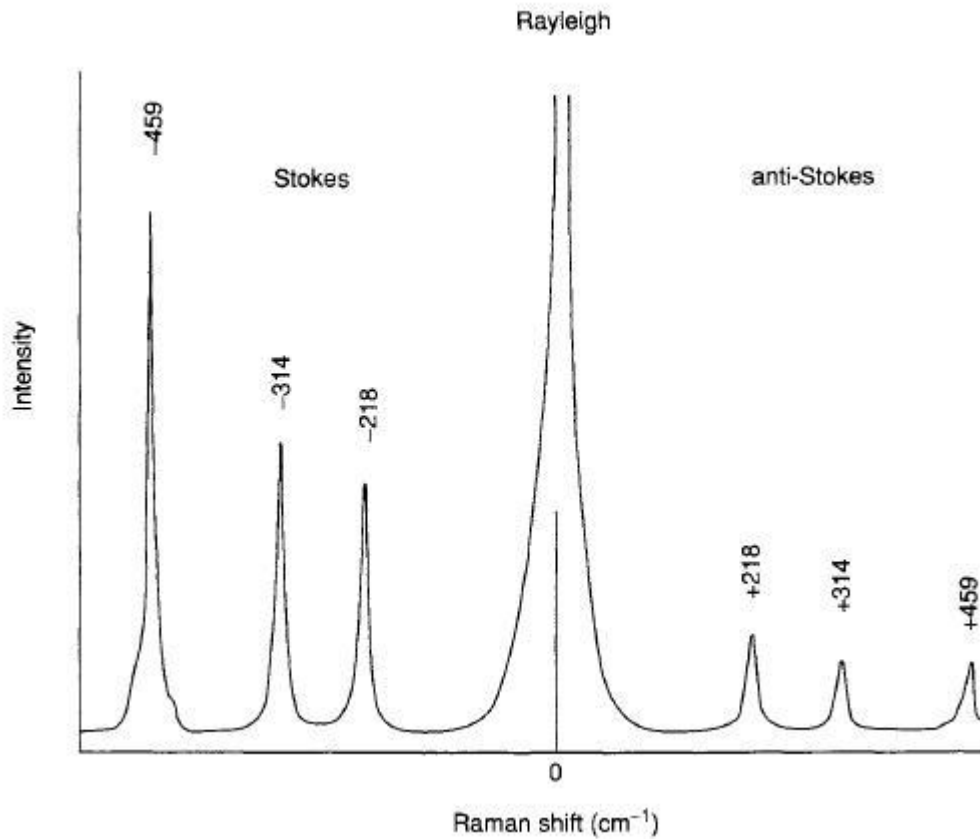


Figure 1-2: Raman Spectrum of CCl<sub>4</sub> (488.0 nm excitation)[9]

$$\frac{I_{anti-stokes}}{I_{Stokes}} = \frac{(\nu_0 + \nu_m)^4}{(\nu_0 - \nu_m)^4} \text{Exp}[-(h\nu_0/kT)] \quad (1.8)$$

This equation also indicates that the Stokes bands should exhibit a higher intensity than the anti-Stokes bands under normal Raman conditions.

Raman scattering is a very inefficient process that has limited the technique[11]. The efficiency of a Raman processes can be determined with the scattering cross section ( $\sigma_{sc}$ ):

$$P_{scatt} = \sigma_{sc} E_{inc} \quad (1.9)$$

where:

$P_{scatt}$  = the rate of scattering from a molecule.

$\sigma_{scatt}$  = scattering cross-section ( $m^2$ )

$E_{inc}$  = irradiance of the incidence photon ( $Wm^{-2}$ )

The cross-section is a property of individual molecules. A comparison with other spectroscopic techniques shows how the low efficiency of Raman leads to low analytical sensitivity and the interference by both Rayleigh scattering and fluorescence.

### 1.3.2 Raman Instrumentation

Three major components make up the commercially available Raman spectrometer. These consist of the following:

1. Excitation source, which is generally a continuous-wave (CW) laser
2. Wavelength selector
3. Detection and computer control/processing systems

A schematic of the typical arrangement of these components is shown in Fig. 1-3. At present, a wide variety of the systems with this general format has been marketed. The major categories for different instruments are defined by the wavelength region for the excitation sources, the type of wavelength selector, and the detection system. Most of the instrumentation will have similar sample illumination and collection systems.

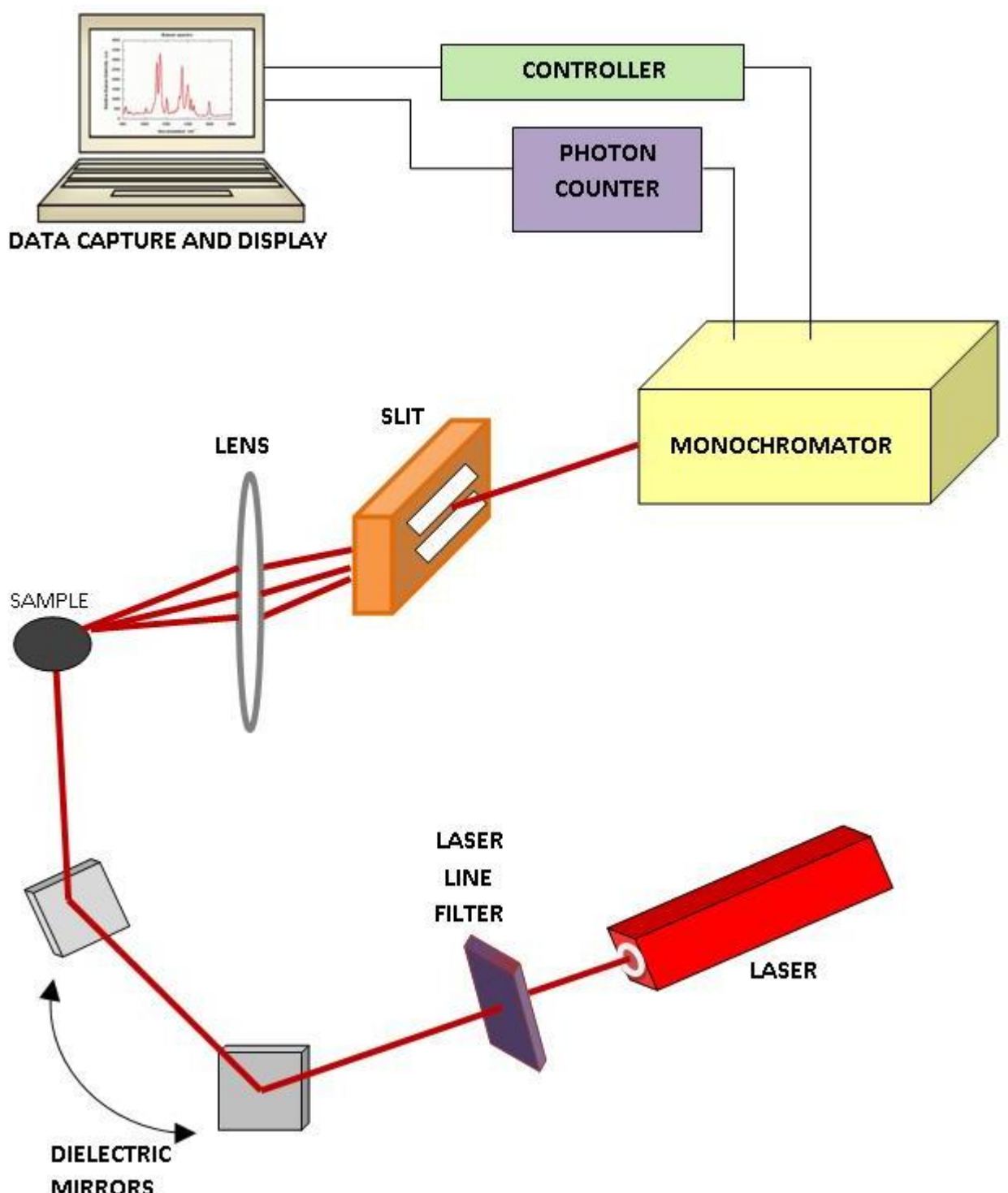


Figure 1-3: Schematic diagram of the major components in a Raman Spectrometer.

## Excitation Source

Elaborated systems have been developed to supply a single wavelength with enough power to produce Raman scattering. Laser sources have become the standard excitation system in Raman spectroscopy. Continuous-wave (CW) lasers, like ion (488.0-514.5 nm), Krypton ion (530.9, 647.0 nm), Helium/Neon (632.8nm), Diode lasers (782 and 830 nm), and Nd/Yag (1064 nm) are now commonly used for Raman spectroscopy. Taking into account the dependence of the intensity of the Raman signals on the fourth power of the laser frequency, lower wavelength sources such as the Argon or Krypton ion, exhibit better responses than their remaining counterparts. These sources can generate Raman signals that are up to three times more intense than those obtained with the corresponding Helium/Neon (He/Ne) source<sup>[12]</sup>. The main disadvantage of using these laser consists in the increased fluorescence emission of the analyte, which overlap and often swamp the Raman signals, thus compromising the sensitivity of the technique at lower wavelengths. The increased power density of these sources also promotes the fast thermal and photolytic decomposition of the analyte. As a result, most of the new Raman systems are shipped with a Helium/Neon source. The recent advances in technology also allowed the use of near infrared (NIR) lasers such as Nd/YAG and

diode lasers as sources for Raman applications. The major advantages of these lasers are the dramatic reduction of the fluorescence and photodecomposition of the analyte upon irradiation.

### **Wavelength Selector**

Advances in wavelength selectors or holographic filtering technology have considerably simplified rejection of the Rayleigh scattering of the incoming laser beam, thus reducing the costs and improving the performance characteristics of modern Raman instruments. The laser line passes through a narrow line band filter to remove all unwanted laser lines. These filters are present at both the absorption and interference stages: absorption filters (used since the early stages of Raman spectroscopy) absorb all unwanted laser lines and transmit specific laser lines of interest, while interference, or laser line filters, reject the unwanted laser lines/wavelengths and transmit the desired bands of wavelengths in the visible, NIR, and mid-IR regions. A pin-hole spatial filter is then used to improve the spatial properties of the laser beam. At last, the incident laser beam reaches a holographic notch filter. This type of filter is fabricated by recording the interference patterns from two mutually coherent laser beams onto the surface of a photoresist-type gelatin. The created pattern produces a sinusoidal profile in the refractive index of the photoresist that reflects over 99.5 % of the incoming radiation directly onto the sample. The

notch filter provides a sharp, narrow rejection of the laser line (less than  $150\text{ cm}^{-1}$  from the central wavelength), that allows the transmission of less than 0.5% of the laser backscatter, while it transmits over 90% of the remaining frequencies to the detector[9]. Holographic notch filters offers superior rejection of the laser line than most of the traditional dielectric filters or triple monochromators. This permits the fabrication of smaller, more economic and considerably more efficient Raman instruments.

### **Detector**

Charged coupled devices (CCD) are the most commonly used detectors in Raman spectroscopy. A CCD is a silicon-based semiconductor arranged as an array of photosensitive elements, each one of which generates photoelectrons and stores them as a small charge. Each element or pixel contains three electrodes sandwiched in a pn-silicon substrate. The Raman scatter is normally dispersed over the longest dimension of the array by a suitable spectrograph. The incident photons induce a charge build-up that at the surface of the irradiated pixels, which is stored in a capacitor (well) located below the electrodes. Once the analytical signals are being collected, a microprocessor within the CCD applies a series of voltages that promote the systematic displacement of the accumulated charges to a shift register located at the end of the array. The data is then digitized and

sent to a computer which converts it into the acquired spectrum. The major advantages of the CCD relative to other multichannel detectors are the low readout noise, which makes optical intensification unnecessary, and offers high quantum efficiency and sensitivity in a wide wavelength range (120-1,000 nm).

#### **1.4 The SERS Effect**

Surface-enhanced Raman spectroscopy was first observed by Fleischman et al. in 1974[13], and the unusual intensity of the Raman signals was attributed to the increased surface area of the rough substrate. In 1977 Jeanmarie and Van Duyne[14] pointed out that the intensification of the effective Raman cross section was due to the surface metal roughness properties. Since then, the observation of SERS by analyte molecules near metal surfaces has stimulated tremendous interest in the optical properties of rough metal surfaces and metal particles. The most popular metal used in these studies has been silver due to intense plasmon resonance excitation that nanometer-size silver particles exhibit at visible wavelengths. This leads to large enhancement factors in surface-enhanced Raman scattering studies on silver, and SERS is also detectable on gold and copper surfaces[15]. SERS is one of the few phenomena that can truly be described as nanoscience. This is because, for it to occur, the metal particles or metal features responsible for its operation must be small with respect

to the wavelength of the exciting light. This normally means that the SERS-active systems must ideally possess structure in the 5 nm to 100nm range.

#### **1.4.1 SERS Enhancement Mechanism**

The mechanisms leading to SERS still remain a matter of controversy , but two mechanisms are popularly mentioned in the literature. In the electromagnetic mechanism, the local electric fields around metal-particle surfaces are enhanced as a result of plasmon excitation leading to more intense electronic transitions in molecules adsorbed near the particle surfaces, and intense Raman scattering. This mechanism leads to the strong sensitivity of SERS intensities to particle size, shape, dielectric environment and arrangement . The second or chemical mechanism involves charge-transfer excitation between analyte molecules and the metal particles to give a resonance Raman enhancement process.

##### **Electromagnetic Enhancement**

Electromagnetic (EM) enhancement in SERS is caused by an amplification of the electric field as a response of the material surface to the incoming irradiation. The magnitude of the enhancement of the local field is dependent on the material and coupling between different surfaces. A small, isolated, illuminated metal sphere will sustain oscillating surface plasmon multipoles of various order induced by the

time-varying electric-field vector of the light[16]. The surface plasmons are collective oscillations of the conduction electrons against the background of ionic metal cores. For a particle much smaller than the wavelength of the exciting light, all but the dipolar plasmon can be ignored[4]. Systems with free or almost free electrons will sustain such excitations; and, the freer the electrons the sharper and the more intense the dipolar plasmon resonance will be. The EM enhancement factor in SERS can be expressed as (Stokes)[6]:

$$E^{EM} = [E_L(\nu_0) / E_I(\nu_0)]^2 \cdot [E_L(\nu_0 - \nu_m) / E_I(\nu_0 - \nu_m)]^2 \quad (1.10)$$

Where:

$E_I$  = Incident electric field

$E_L$  = total local electric field

$\nu_0$  = frequency of the incident light

$\nu_m$  = vibrational frequency

The first part of eq. 1-10 also referred to as the laser enhancement factor ( $A_L$ ), and the right side is referred as to the Raman enhancement factor ( $A_s$ ).

Assuming the shape of the metal nanoparticles being spherical and that its size is considerably smaller than the wavelength of the electromagnetic field (EMF), a molecule in the vicinity of the sphere

(distance  $d$ ) is exposed to a total EMF( $E_L$ ), which is the superposition of the incident field ( $E_I$ ) and the field induced in the metal sphere ( $E_S$ ). The field enhancement factor  $A$  at the position of the molecule can be expressed as[3]:

$$A = \frac{E_L}{E_I} \approx \frac{(\epsilon_M - \epsilon_i)}{(\epsilon_M + 2\epsilon_i)} \left( \frac{r}{r + d} \right)^3 \quad (1.11)$$

$\epsilon_M$  = dielectric function of the metal

$\epsilon_i$  = dielectric function of the media

$r$  = radii of the metal nanoparticles

$d$  = distance from the molecule to the surface of the metal particle

Taking into account enhancing effects for the laser and the Raman (Stokes) fields, the electromagnetic enhancement factor can be written as:

$$E^{EM} = \left[ \frac{(\epsilon_M - \epsilon_i)}{(\epsilon_M + 2\epsilon_i)} \right]^2 \left[ \frac{(\epsilon_M - \epsilon_i)}{(\epsilon_M + 2\epsilon_i)} \right]^2 \left[ \frac{r}{r + d} \right]^{12} \quad (1.12)$$

Provided that the imaginary part of the dielectric constant of the metal is negligible, the fields are at resonance when  $\epsilon_m = -2\epsilon_i$ . This model indicates that the electromagnetic enhancement scales to the fourth power of the effective electromagnetic field. The electromagnetic model also demonstrates that the strength of the induced EMF increases when the incident field is at resonance with the localized surface plasmons. The electromagnetic enhancement of the SERS signal does not require a direct contact between the molecules of the analyte

and the metal nanoparticles. However, the effective EMF experienced by the molecules of the analyte decays exponentially with increasing the distance from the metal surface. Therefore, the electromagnetic enhancement in the SERS signals is stronger when the molecules of the analyte are at close proximity to the metal particles. This model considered the situation for a single metal particle, however, almost all effective SERS-active systems, consist of assemblies of interacting particles. Examples are nanoparticle aggregates, rough metals surfaces and island films. More recently, the interest has been for closely spaced, well-engineered systems of interacting metal nanostructures that fulfill the double goals of providing high field enhancement and doing so with highly reproducible and controllable SERS platforms. The interparticle effect can be understood if we suppose a molecule located in the interstice between two metal nanospheres and is surrounded by two sets of time-varying conjugate charges arising from the polarization of the individual nanoparticles as shown in figure 1-4[17]. As the nanoparticles are brought closer together, the proximity of these charges to the molecule can be made arbitrarily close and hence the field sensed by the molecule larger. The mutual interaction of the two nanospheres also leads to an increase in the magnitude of the dipole induced in each component of the nanosystem. The dipole

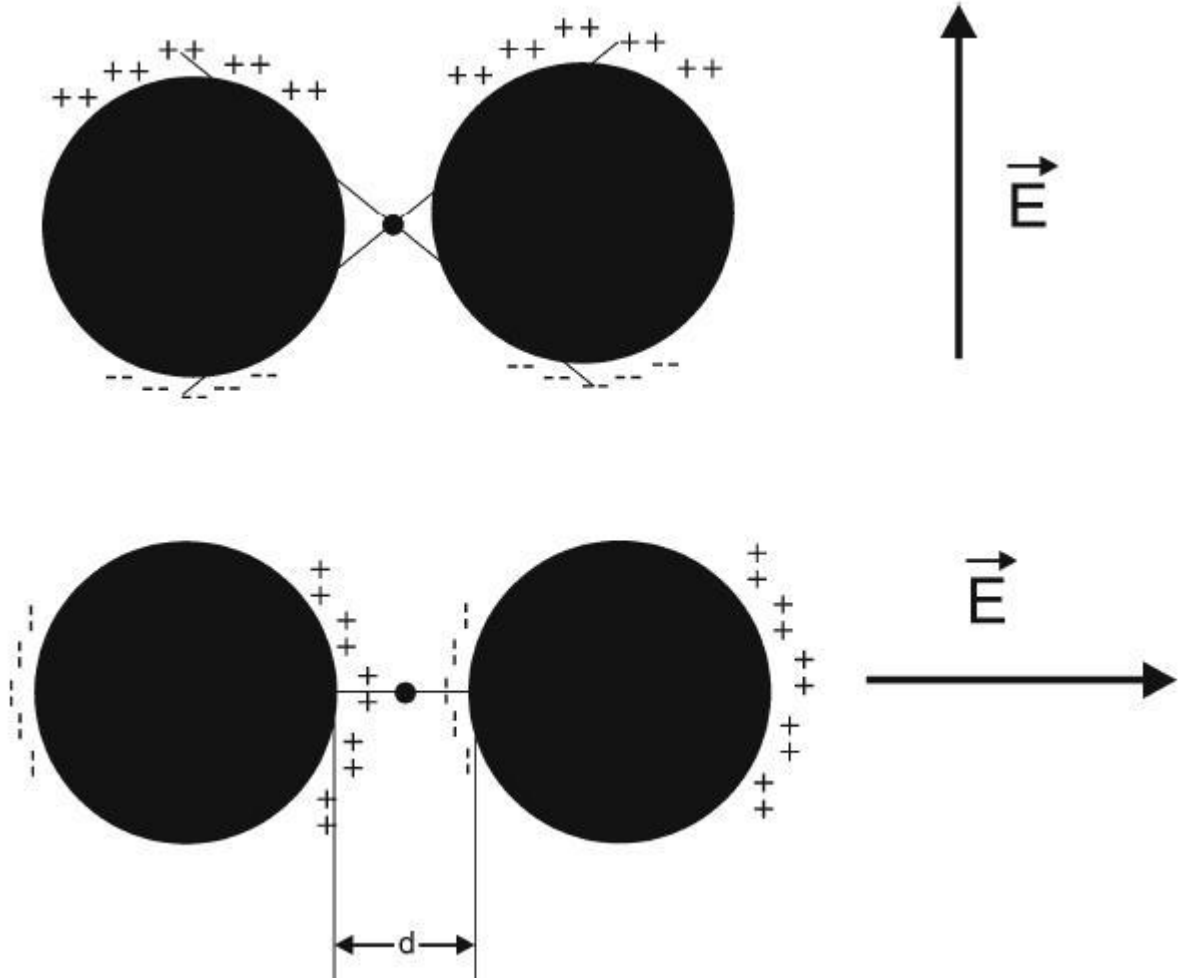


**Figure 1-4: Top:light polarized perpendicular to the interparticle axis. Bottom:light polarized parallel to the interparticle axis[15]**

induced in each nano-object arises from the combined field of the incident light and the intense field of its partner, which, in this configuration, leads to an amplification of the polarization. It is demonstrated that for light polarized along the interparticle axis, the enhancement increases approximately as  $d^{-8}$  where  $d$  is the gap size between the two nanospheres[? ]. On the other hand, when the light is polarized in the other direction, illustrated in Fig. 1-4 (top), that is, normal to the axis

joining the centers of the two nanospheres, a molecule in the interstitial region will not benefit from proximity to the induced charges, even if the particles are brought closely together. Additional studies have been accomplished to determine the EMF in situations where substantial morphological changes in the shape of the single particle exist[4]. It was found that the presence of protrusion increases the enhancement factor dramatically. The discrete dipole approximation (DDA)[2] was used by Hao and Schatz[18] to investigate the electromagnetic fields induced by optical excitation of localized surface plasmon resonances (LSPR) of silver nanoparticles, including monomers and dimers. In their calculations, they chose spheres with radius of 36nm, and triangle calculations all refer to triangles that are 60nm in edge length. another shapes studied are oblate spheroids, with aspect ratio of 3.4:1, and a cylindrical rod with an aspect ratio of 2.8:1. Figure 1-5 the EM fields for nonspherical particles. The contours show that the maximum enhancement occurs at the particle tips. The largest fields ( $|E|^2$ ) are 3500 (times the incident field) for the triangular prism, 4500 for the rod, and 4700 for the spheroid at the resonance wavelength of 700nm.

Figure 1-6 presents the results obtained from calculations performed with dimmers of particles. The top of this figure shows contours of the EMF ( $|E|^2$ ) around a pair of Ag spheres for 430 and 520nm. It can be seen that the maximum enhancement occurs at

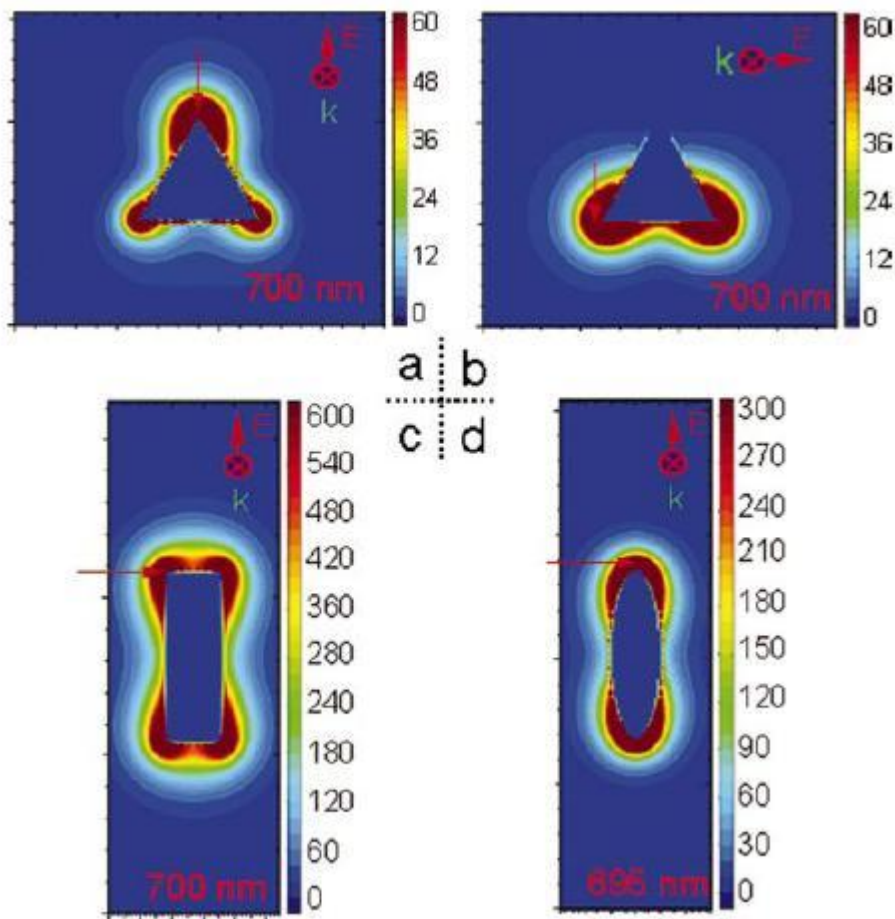


**Figure 1-5:** E-field enhancement contours external to monomers with different shapes. a) and b) are the E-field enhancement contours external to a triangular prism polarized along the two different primary axes, c) and d) are the E-fields enhancement contours for a rod and spheroid polarized along their long axes. The arrows show where is the maximum E-field[16].

the midpoint between the two spheres. The largest fields are 3500 times the applied field at 420nm and 11000 times the applied field at 520nm, respectively. These enhancement are much larger than those found for isolates Ag spherical nanoparticles. The middle and bottom of the figure 1-6 show the contours of different arrangements of triangular prisms. For the head to head configuration (fig 1-6 middle) the largest fields are 53000 and 57000 times the applied field, for 932 and 550nm respectively. For the head to tail configuration (figure 1-6

bottom) the largest fields at 852 and 650nm are 57000 and 3700 times the applied field, respectively.

The results obtained by Hao and Schatz are in accordance with those presented by Xu[4], in the sense that the maximum fields enhancement are found in the sharp edges of the nanoparticles.

## 1.5 Review of SERS Substrates

An optimum SERS substrate should be capable of maximizing the Raman intensity, relatively inexpensive, simple to prepare, highly homogeneous, stable, robust, and reproducible. The most commonly used substrates for SERS applications are noble metal particles, such as copper, silver and gold. Silver and gold nanoparticles exhibit maximum SERS activity when the dimensions of the particles are within the 10-100 nm range. These particle aggregates (clusters), typically exhibit fractal-like properties, which result in an inhomogeneous distribution of the induced electromagnetic fields over the substrate surface. As a result, the maximum enhancement of the SERS signal often occurs in highly localized areas (hot-spots), which are randomly distributed through the entire surface. A considerable amount of research has been devoted to increasing the homogeneity of these surfaces, as well as, to maximize the strength of the induced electromagnetic field.

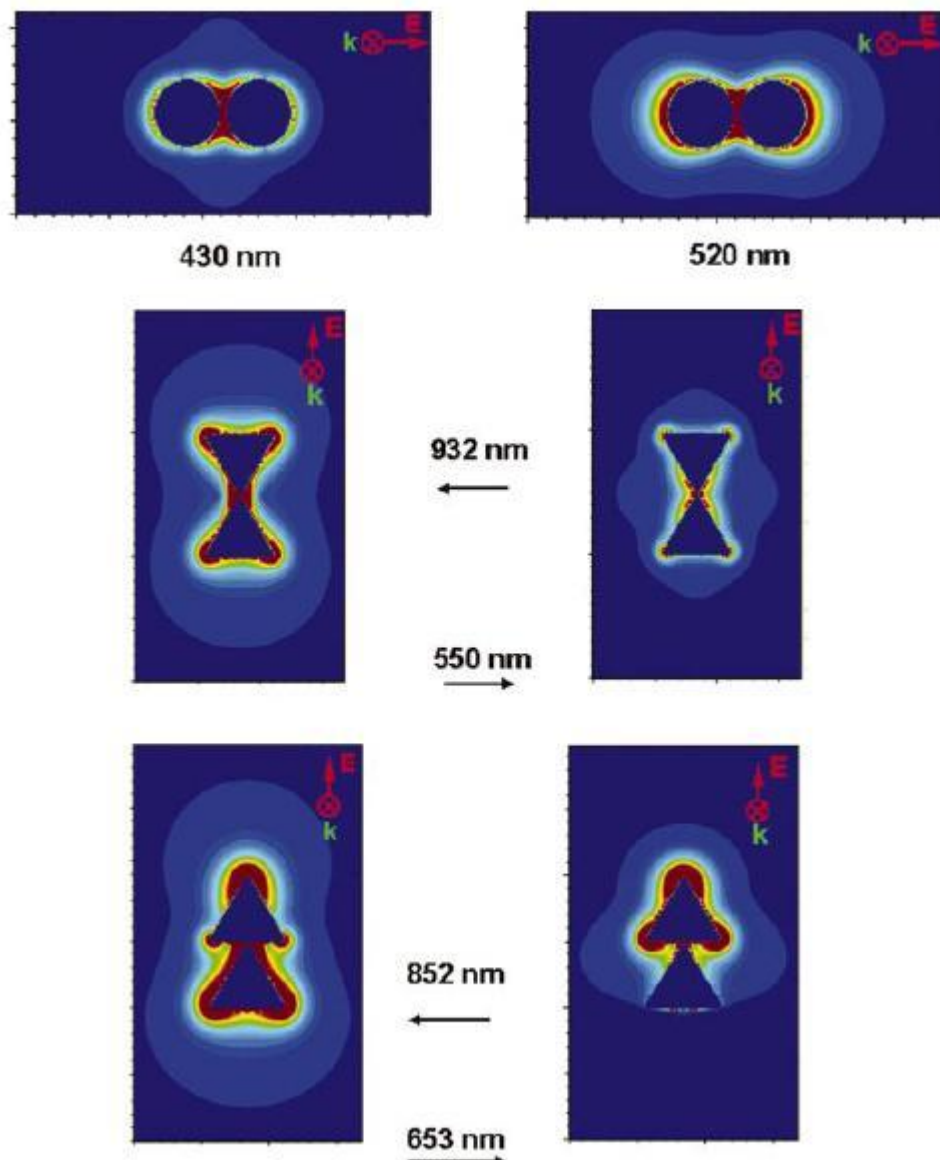


**Figure 1-6:** E-field enhancement contours external dimer of Spheres(top), head to head triangles configuration(middle) and head to tail triangles configuration(bottom)[16].

In the 1970s several observations reported dramatic enhancements in the Raman scattering signal of molecules absorbed on roughened

silver electrodes[13]; therefore, these surfaces were the first to be utilized for SERS. These types of substrates are prepared by the initial oxidation of the electrode surface, followed by the etching (roughening) of the surface with a series of oxidation-reduction cycles[19]. This process results in the formation of a series of protrusions in the range from 25-500 nm[20]. The spatial orientation of the electrode is adjusted so it facilitates the focusing of the laser beam onto the surface of the metal. Silver electrodes were exploited in the initial SERS studies[21, 22]. Other types of electrodes such as gold, copper and platinum have also been used. Since that first observations a lot of effort have been focused on developing techniques to create more effective SERS substrate, providing stable and optimized enhancement factors, and permit SERS studies in diverse environments. Besides roughened electrodes, there are variety of SERS substrates available today, with the most common SERS substrates being those with the desired optical properties. Some of those substrates include, metal island films, colloidal nanoparticles, and surface confined nanostructures. One of the most common SERS active substrates are colloidal nanoparticles. The solutions are prepared by mixing an aqueous solution of the metal (e.g. 1% silver nitrate), with a good reducing agent such as sodium citrate or sodium borohydride[23, 24]. The aggregated particles are typically 10-100nm in diameter, and can be used either

as an aqueous suspension or as a dried solid[3]. Some of the disadvantages of colloidal nanoparticles include their tendency to coagulate, low stability, inhomogeneous size distribution, light sensitivity, and low reproducibility.

Physical vapor deposition (PVD) of thin-metal films onto solid surfaces such as glass, and silica[25, 26] is used to create SERS active substrates. The PVD process involves the electro-thermal evaporation of a metal under high vacuum conditions. The evaporated particles travel through the interior of the evaporation chamber reaching the surface of the solid support. Under these conditions, the adsorbed particles aggregate at the surface of the solid support forming isolated clusters, also known as island films[27, 28]. SERS substrates consisting of closed packaged nanostructures can be produced by several fabrication methods, including nanosphere lithography[29, 30], and electron beam lithography[31–33]. Nanosphere lithography begins with the self-assembly of size monodisperse nanospheres of a certain size to form a two-dimensional colloidal crystal deposition mask. A metal is then deposited at specific rate and thickness and the nanosphere mask is removed, leaving behind surface confined triangles nanoparticles.

Producing surface confined nanostructures using Electron Beam Lithography (EBL) involves the exposure of a thin layer of a photoresist to high energy electrons, followed by the development of this resist

and the deposition of noble metals. EBL provides control over inter-particles spacing and can fabricate arbitrary shapes. Previous work performed by De Jesus et. al. [34] showed strong SERS signal using substrates with densely packed polymeric arrays that were metalized via physical vapor deposition to create isolated metal nanoparticles.

## **1.6 Structure of Thesis**

Chapter 2 exposes the theoretical basis involving Electron Beam Lithography (EBL), which is the nanofabrication method used to create the SERS active surface. Chapter 3 is focused on the material and methods utilized to create the proposed nanofabricated SERS substrates. In Chapter 4 the materials and methods used to test the final SERS performance and results are presented. The conclusions and future work are provided in Chapter 5.

## CHAPTER 2

# ELECTRON BEAM LITHOGRAPHY BASICS

### 2.1 Lithography

The word *Lithography* comes from the greek words lithos (stone) and gráphein (to write), and refers to the proces developed in 1796 by Aloys Senefelder[35]. Senefelder found that stone, when properly inked and treated with chemicals could transfer carved image onto a paper. He found that the image (non-image) area became oil receptive after the chemical treatment, and the nonimage (image) area turnes oil repelent. Today, lithography is referred to the proces of transferring patterns, mostly with micro and nano scale sizes, from one medium to another, and is increasingly finding relevant importance in many areas, from sensors and actuators to biomedical devices, in addition to its use in microelectronics device manufacturing. Modern lithographic patterns are produced when a radiation sensitive material is exposed to a source, that can be UV, X-ray radiation or an electron beam.

## 2.2 Types of Lithography

### 2.2.1 Optical Lithography

Optical lithography is the most commonly used form of lithography. This technique uses a mask to repeatedly generate a desired pattern on resist coated wafers. The mask, which consists of a nearly optically flat glass (transparent to near ultraviolet [UV]) or quartz plate (transparent to deep UV) with an absorber pattern metal, is placed in direct contact with the photoresist coated surface, and the wafer is exposed to UV radiation. The absorber pattern on the photomask is opaque to UV light, whereas glass and quartz are transparent. Depending on the photoresist tone (positive or negative), the exposed or nonexposed areas of the photoresist are dissolved after immersed in a developer solution, and the mask image is transferred to the wafer. Photolithography process steps are summarized in figure 2-1.

A thin negative photoresist layer (B) is coated onto a bare silicon wafer (A). After exposure (C), the wafer is immersed or rinsed with a developer solution, which removes the unexposed areas of photoresist and leaves a pattern of bare silicon and photoresist on the wafer surface (D). The minimum feature size achievable by photolithography is proportional to the wavelength of the source. For this reason and other defects, optical techniques perform satisfactorily for feature sizes in the order of  $1\mu\text{m}$  and larger, which is becoming increasingly

unsatisfactory for a lot of miniaturization applications, where critical dimensions rely on the nanometric scale.

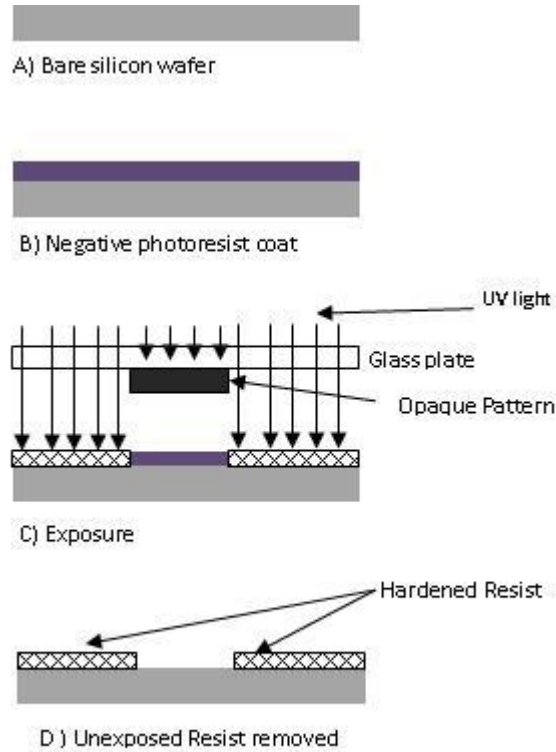


**Figure 2–1:** Basic photolithography steps.

### 2.2.2 X-ray Lithography

X rays were discovered by W. H. Roentgen, while experimenting on the nature of cathodic rays[36]. Since then, X-rays have encountered applications in medicine and industrial inspection. In lithography, this radiation has the advantage of defining high resolution images( $\sim 0.1\mu\text{ m}$ ) in thick materials. The resolution comes from the extremely short wavelength, which is in the order of 1nm. X-ray lithography is superior to optical lithography because of the use of shorter wavelength and the flexibility of the exposure time and development conditions.

Reproducibility is high, as results are independent of substrate type, surface reflections, and wafer topography. The three main classes of sources for x-ray lithography are electron impact tubes, laser-based plasmas, and synchrotrons.

### **2.3 Introduction to Electron Beam Lithography**

Electron beam lithography (EBL) is a specialized technique for creating the nanometric scale patterns required by the modern applications. EBL is almost capable of resolutions to the atomic level, and is a flexible technique that can work with a variety of materials and an almost infinite number of patterns [37]. The technique consists of scanning a beam of electrons across a surface covered with a resist film sensitive to those electrons, thus depositing energy in the desired pattern in the resist film. For positive resists, the development eliminates the exposed area, whereas for negative resists, the exposed areas remain in the substrate. This lithographic technique comprises three steps: sensitive material coating, exposure of the resist and development of the resist. It is important to point out that the final resolution is conditioned for the cumulative effect of each individual step of the process. As a consequence, the shape, energy and intensity of the electron beam, the molecular structure and thickness of the resist, the electron-solid interactions, the developing conditions and the irradiation process, affect the results, in terms of dimensions, resist

profile and feature definition.

EBL patterning, based on the scanning electron microscopes (SEM), were developed in the late 1960s. In these systems the electron beam is focused to smallest size possible for a given set of electron optics and operating conditions, and exposes individual pattern pixels. The current distribution within the beam is nearly Gaussian and spots are overlapped to provide the smoothest features[38]. The main disadvantage of this technique is the low writing speed (throughput), being one or more orders of magnitude slower than optical lithography. Figure 2-2 shows a block diagram of a typical EBL configuration. Forming and controlling the electron beam is accomplished by the column of the SEM.

Underneath the column is a chamber containing a stage for moving the sample around, and facilities for loading and unloading it. Associated with the chamber is a vacuum system needed to maintain an appropriate vacuum level throughout the column and also during the load and unload cycles. A set of control electronics supplies power and signals to the various parts of the machine. Finally, the system is controlled by a computer, which handles such diverse functions as setting up an exposure job, loading and unloading the sample, aligning and focusing the electron beam, and sending pattern data to the pattern

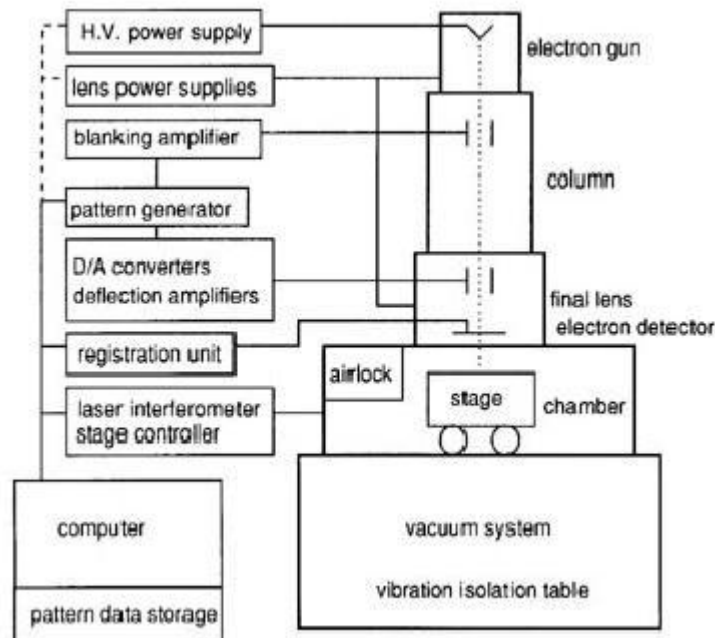


**Figure 2–2:** Block diagram showing the major components of a typical EBL system[36] generator. The part of the computer and electronics used to handle pattern data is sometimes referred to as the datapath.

### 2.3.1 Electron Optics

As previously mentioned, the electron optical column is used to form and direct a focused beam of electrons onto the surface, which is mounted in a holder and clamped to the stage. Figure 2-3 shows a typical EBL column configuration[39]. The electrons are produced in the uppermost section, which is called the electron source or gun. The beam of electron passes through several additional stages in the electron optical column, which perform specific processes to produce a beam having the required current and spot size and correctly focused onto the substrate. Other column components include two or more

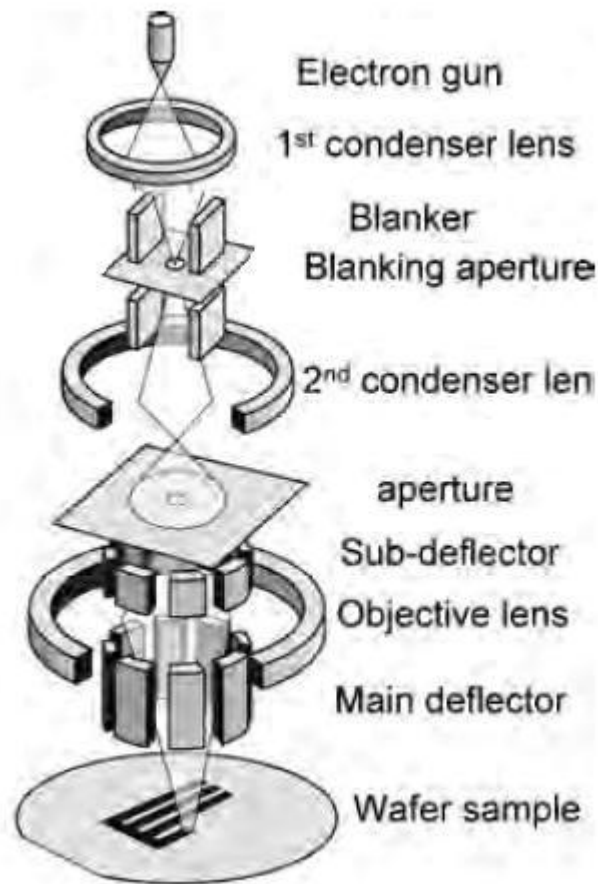


**Figure 2–3:** Components of a typical SEM column[37]

lenses, a mechanism for deflecting the beam, a blarker for turning the beam on and off, a stigmator for correcting any astigmatism in the beam, apertures for helping to define the beam, alignment systems for centering the beam in the column, and finally, an electron detector for assisting with focusing and locating marks on the sample. The optical axis ( $Z$ ) is parallel to the electron beam, while  $X$  and  $Y$  are parallel to the plane of the sample. Beam current and current density are critical parameters in the optimization of pattern writing time.

The electron optical system is limited by the brightness of its electron gun, the imaging limitations of its lenses, and beam interactions along the beam path. The relative importance of these limitations depends upon the writing strategy used.

### **Electron Source**

Electrons may be emitted from a conducting material either by heating it to the point where the electrons have sufficient energy to overcome the work function barrier of the conductor (thermionic sources) or by applying an electric field sufficiently strong such that they tunnel through the barrier (field emission sources). Three key parameters of the source are the virtual source size, its brightness (expressed in amperes per square centimeter per steradian), and the energy spread of the emitted electrons (measured in electron volts)[37]. The size of the source is related to the demagnification that must be provided by the column to get a small spot at the substrate. Table 2-1 shows the characteristics of different types of electron sources. One common electron source is a tungsten wire heated by passing a current through it. The disadvantage of this source is its relative low brightness and large energy spread caused by the high operating temperature. Recently, lanthanum hexaboride ( $\text{LaB}_6$ ) has become a very used cathode; due to a very low work function, and the high brightness that is obtained at an operating temperature of around 1800 K. The

beam current delivered by thermionic sources depends on the temperature of the cathode. Higher temperatures can deliver greater beam current, but also generate an exponentially decreasing lifetime due to thermal evaporation of the cathode material. The thermal field emitter provides the highest brightness and smallest source size. It combines the sharp tungsten needle of the field emission source and the heating of the thermal source. Because the tip operates at a temperature of about 1800 K, it is less sensitive to gases in the environment and can achieve stable operation for months at a time. The tungsten is usually coated with a layer of zirconium oxide to reduce the work function barrier.

### **Electron Lenses**

Once the beam is formed, the electron optics is responsible for focusing and deflecting the beam. Electrons can be focused using either an electric or a magnetic field. Electrostatic lenses usually produce higher aberrations; therefore, magnetic lenses are preferred to focus the beam. Magnetic lenses are fabricated by wrapping a circularly symmetric iron core with turns of copper wire. Passing a current through the wire produces a magnetic field. The flux path is rotationally symmetric except for an air gap in the center of the lens. In this air gap the flux leaks out to form a flux gradient, which acts as a lens for the electron beam. Electrostatic lens are most often found in the

**Table 2–1:** Properties of the electron sources commonly used in electron beam lithography[35].

source type	brightness ( $A/cm^2/sr$ )	source size	energy spread (eV)	vacuum requirements (Torr)
tungsten thermionic	$\sim 10^5$	$\sim 25\mu m$	2-3	$10^{-6}$
LaB <sub>6</sub>	$\sim 10^6$	$\sim 10\mu m$	2-3	$10^{-8}$
thermal FE	$\sim 10^8$	$\sim 20nm$	0.9	$10^{-9}$
W & cold FE	$\sim 10^9$	5nm	0.22	$10^{-10}$

gun region as a condenser lens since they can be combined with the extractor or anode used to pull electrons out of the cathode, and they are easily made for ultrahigh vacuum use and are bakeout compatible. Also, aberrations in the condenser lens tend to be less important. System performance is usually dominated by the aberrations of the final lens. Figure 2-4 shows a typical configuration of an electrostatic lens and a magnetic lens.

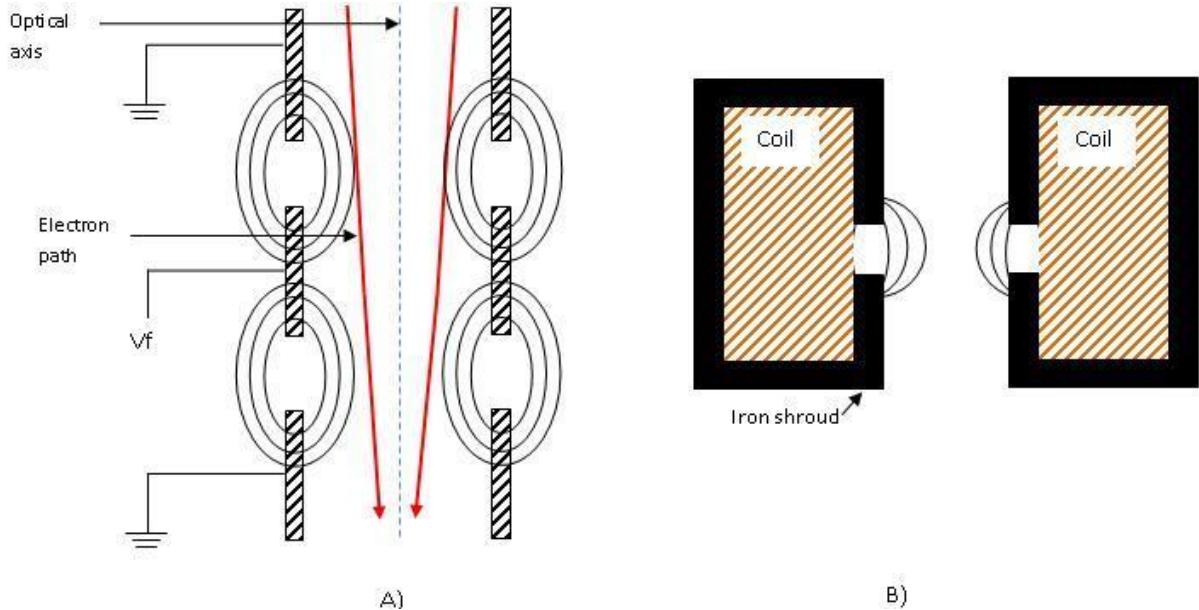


**Figure 2-4:** A) Electrostatic lens configuration. B) Magnetic lens configuration.

### Electron Beam Deflection

The electron beam deflection is used to scan the beam across the surface of the sample. In the same way of the focusing lenses, deflection can be accomplished either electrostatically or magnetically. It is implemented with coils and plates that can create fields perpendicular to the optical axis. The magnetic deflection again introduces less distortions, but with electrostatic deflection can achieve faster response. Since deflection systems are frequently placed inside the final lens, care must be taken to prevent the fields from interacting with conducting metal parts. Usually the final lens will be shielded with ferrite to minimize eddy currents. Some tools use multiple deflection systems, where high speed, short range deflection is done electrostatically while long range deflection is magnetic.

## Other Column Components

Other optical elements include apertures, alignment coils, blanking plates, and stigmators.

Apertures are small holes through which the beam passes on its way down the column. There are several types of apertures. A blanking aperture is used to turn the beam on and off by deflecting the beam away from the aperture hole. The aperture intercepts the beam when not writing. A beam limiting aperture has two effects: (1) it sets the beam convergence angle  $[\alpha]$  (measured as the half-angle of the beam at the target) through which electrons can pass through the system, (2) controls the effect of lens aberrations and thus resolution, and also sets the beam current. A beam limiting aperture is normally set in an X-Y stage to allow it to be centered, or aligned, with respect to the optical axis. It is best to have a beam limiting aperture as close to the gun as possible to limit the effects of space charge caused by electron - electron repulsion. The beam blanker turns the beam on and off, and usually consists of a pair of plates set up as a simple electrostatic deflector. One or both of the plates are connected to a blanking amplifier with a fast response time. A voltage is applied across the plates which sweeps the beam off axis until it is intercepted by a downstream aperture. The stigmators are in charge of correcting

beam shape to be circular. It consists of four or eight poles that surround the optical axis.

### **2.3.2 Electron-Solid Interaction: Proximity Effect**

Electron beam lithography systems can create extremely fine patterns, but its resolution limits are determined in part by the events that take place when the electrons hit the workpiece. As the electrons penetrate the resist, they experience many small angle scattering events (forward scattering) which tend to broaden the initial beam diameter. As the electrons penetrate through the resist into the substrate, they occasionally undergo large angle scattering events (backscattering). The backscattered electrons cause the proximity effect, where the dose that a pattern feature receives is affected by electrons scattering from other features nearby. The range of the electrons (defined here as the distance a typical electron travels in the bulk material before losing all its energy) depends on both the energy of the primary electrons and the type of substrate. During this process the electrons are continuously slowing down, producing a cascade of low voltage electrons called secondary electrons. The fraction of electrons ( $e$ ) that are backscattered, is roughly independent of beam energy, although it does depend on the substrate material, with low atomic number materials giving less backscatter. Typical values of  $e$  range from 0.17 for silicon to 0.50 for tungsten and gold. Figure 2-5 shows

a Monte Carlo simulation of electron scattering in a silicon substrate for two different beam energies. If a pattern has fairly uniform den-

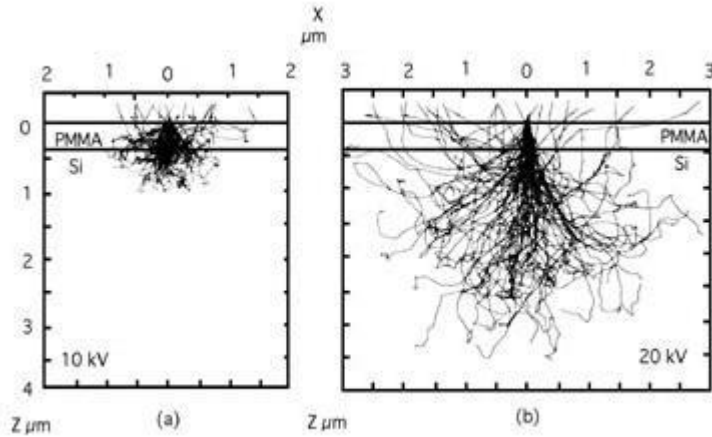


**Figure 2–5:** Monte Carlo simulation of electron scattering in resist on a silicon substrate at a) 10 kV and b) 20 kV[36].

sity and linewidth, the best way to minimize the proximity effect is to adjust the overall dose until the patterns come out in the proper size. Higher contrast resists can also help minimize the linewidth variations.

### 2.3.3 Proximity effect correction

#### Dose Modulation

The most widely used technique for correcting for proximity effect exposure is dose modulation. In this method, each individual shape in the pattern is assigned a dose calculated in a way that the shape prints at its correct size. The technique implies costly and time consuming computation required to evaluate the dose correction that must be applied.

## **Shape Modification**

A similar computational magnitude to that associated with dosed modulation is required to apply this method. In this approach, the extra dose that dense patterns receive is compensated for by slightly reducing their size. This technique has the advantage that it can be implemented on EBL systems that are not capable of dose modulation.

## **Multilayer Resists**

A multilayer resists configuration can be used to reduce the proximity effect by applying a thick resist as the bottom layer. This layer must be thick enough, to absorb almost completely the backscattered electrons from the substrate. The extra complexity introduced by the bilayer resists increases the processing cost considerably.

## **GHOST**

To correct the proximity effect with this method, the reversed field of the pattern is written by a correction exposure after the pattern exposure has been completed. The beam conditions for the corrected energy deposition are adjusted to mimic the backscattered electron energy distributions produced by the pattern exposure (figure 2-6). After this has been done, each pattern has received the same energy distribution, and the proximity effect has been corrected.[40]

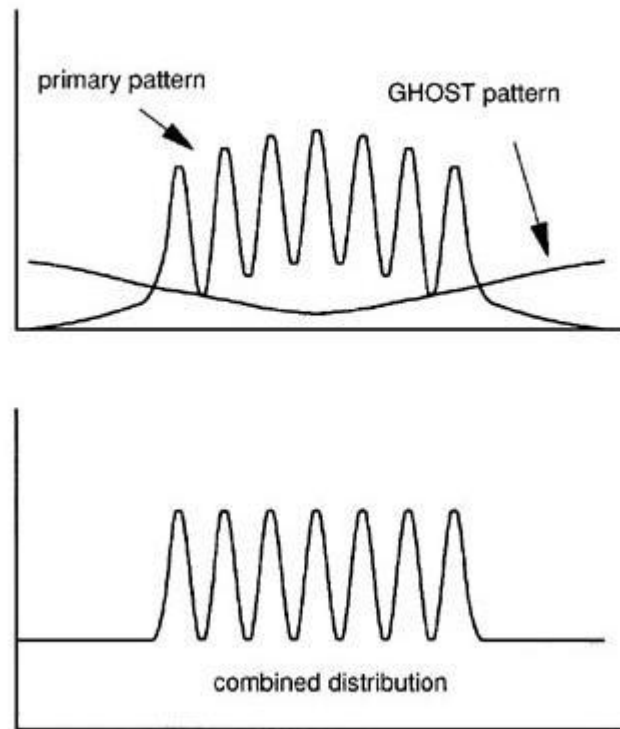


**Figure 2-6:** Schematic showing how the GHOST technique can be used to correct for the proximity effect. The top curves show the energy distribution in the resist for a group of seven lines from the primary exposure and from the GHOST exposure. The bottom curve is the resulting final energy distribution, showing the dose equalization for all the lines.[36]

### 2.3.4 Writing Strategies

In Raster Scan mode, the beam is swept across the entire field, pixel element by pixel element, and the beam is turned off and on (blanked and unblanked) as needed to expose the desired pattern. This strategy is based on a relatively simple architecture that is easy to calibrate. The disadvantage is that sparse patterns take just as long to write as dense patterns. An additional drawback is that dose adjustment within the pattern, for purposes of correcting for proximity effect, is inherently difficult. Vector Scan mode makes the beam

jump from one pattern to the next, skipping over all non-patterned areas. This method of not visiting every point in the makes the vector scan approach faster than raster scan for sparse patterns. Figure 2-7 illustrates the raster and vector scan writing modes.

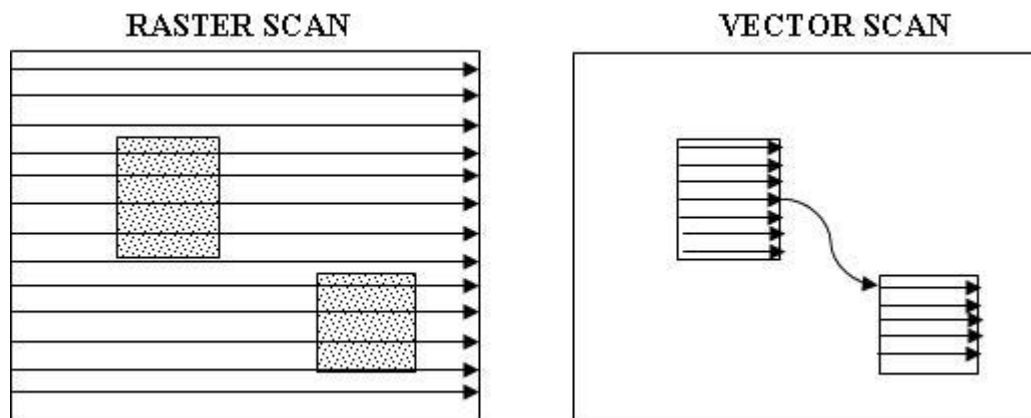


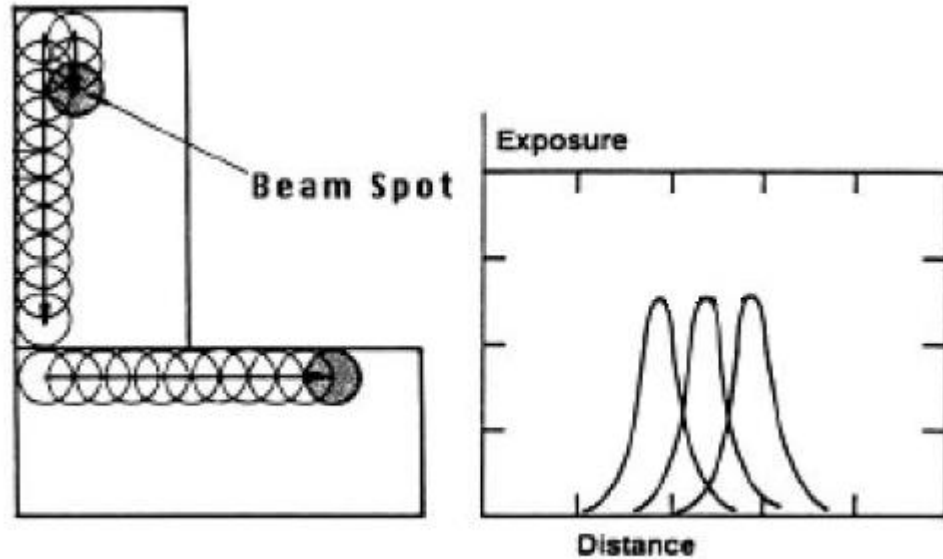
**Figure 2-7:** Typical electron beam writing strategies

### 2.3.5 Exposure Parameters

In the direct writing EBL, the desired pattern in the resist is exposed point by point in a straight manner, by an overlapping rounded beam (figure 2-8). Several exposure conditions and operational parameters used in EBL determine the final process performance and pattern definition. The influence and determination of the conditions and the different parameters involved in the irradiation and operation are presented next.

#### Dose

The dose is the energy that the resist receives from the incoming electrons to fully develop the resist thickness, whatever its shape, area or lines. Its definition varies according to the type of filling method

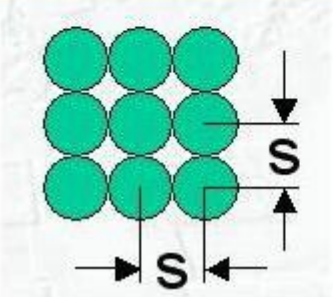
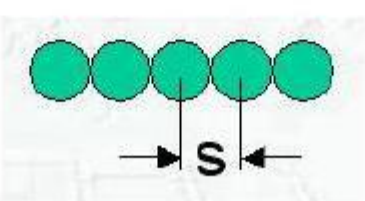
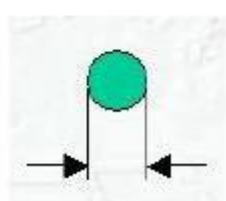


**Figure 2–8:** Exposure condition for EBL direct writing[39].

used to create the pattern. The dose can be chosen as area, line or dot dose (Fig-2-9). The dwelltime ( $T_{dwell}$ ) is the time the beam remains in each pixel to deliver the correct dose. The proper dose is determined during the exposure process, and depends on many interrelated parameters: resist, developer conditions, beam energy [38].

### Working Distance

The working distance influences the susceptibility to external interference, and on some microscopes, the optimal magnification setting that should be used. A shorter working distance will improve the resolution of the microscope and will reduce the susceptibility of the beam to external interference. In cases where the microscope environment has magnetic fields, using a shorter working distance may have a dramatic effect on the writing quality. For most microscopes, a working

Area dose (AD)	SPL dose (LD)	Dot dose (DD)
$AD = I_{\text{beam}} \cdot T_{\text{dwell}} / s^2$ ( $\mu\text{As}/\text{cm}^2$ )	$LD = I_{\text{beam}} \cdot T_{\text{dwell}} / s$ ( $\text{pAs}/\text{cm}$ )	$DD = I_{\text{beam}} \cdot T_{\text{dwell}}$ ( $\text{pAs}$ )
		

**Figure 2–9:** Definition of dose for area, line and dot exposure.[39]

distance between 5 and 10 mm is appropriate for writing fine features. The working distance can also affect the optimal magnification settings. When the scan control electronics change from one subrange to another, it will generally produce a small temporary image distortion and/or an audible click from a mechanical relay. The best signal-to-noise within the scan control electronics will be found at the higher magnification value after a transition[41].

### Accelerating Voltage

Increasing the accelerating voltage will produce a greater electron penetration depth, thus lowering the number of scattered electrons in the resist (see fig. 2–5), which will result in finer linewidths. The

accelerating voltage can also affect the magnification settings in conjunction with the working distance previously mentioned. Most SEMs will have a maximum accelerating voltage of 30 kV, which will be the voltage used for most fine writing.

### **Beam Current**

A lower beam current will produce a smaller spot size on the sample than a larger beam current. The smallest spot size can be achieved by using the highest available accelerating voltage and a reasonably low beam current. The typical range of beam current used for fine lithography is 5 to 50 pA, where the optimal value will vary depending on the model of SEM as well as the filament type. Some of the common ranges are: 5–10 pA for a W filament, 10–20 pA for a  $\text{LaB}_6K$  filament, and 20–50 pA for a FE microscope. In general, the goal is to use a beam current that is small enough to produce the desired feature sizes, but is also large enough to make the microscope reasonably easy to optimize.

#### **2.3.6 Nanometer Pattern Generation System**

Nanometer Pattern Generation System (NPGS) is a SEM conversion kit sold by J.C. Nability Lithography Systems, which is built around a Windows-based PC-compatible with an ISA bus. A 16 bit multifunction board from Data Translation is used to generate the X and Y beam deflections and to program a second board which provides

the signals for blanking control. The beam is deflected from shape to shape in a writing field (vector scan mode), with the unique feature that the raster for filling arbitrary polygons can be defined by the user. The user can specify the raster to be parallel to any side of the polygon and has control over the exposure spot spacing in X and Y. Angled lines, polygons, and arbitrarily shaped features are all supported, and data can be imported in common e-beam formats: GDSII (Stream), CIF, and a subset of DXF (AutoCAD.)

## **2.4 Resists**

Resists are the sensitive material to electrons and are able to be developed by certain developers after exposure. The resists may produce either a positive or negative image compared to the exposed areas. Similar to photoresist, electron beam resists play two primary roles in lithography: (a) precise pattern transfer and (b) formation and protection of the covered substrate from etching or ion implantation. The resists will normally be removed with the completion of these functions. However, in some cases the resists are also employed as a part of device and structure. Important properties of electron beam resists include resolution, sensitivity, contrast and etch resistance. Exposing a positive resist to a range of doses and then developing the pattern, the average film thickness versus dose, gives a graph as shown in Fig. 2-10(a) is obtained. The sensitivity of the resist is defined as

the point at which all of the film is removed. Ideally, the film thickness would drop abruptly to zero at the critical dose. In practice, the thickness line drops with a finite slope. If  $D_1$  is the largest dose at which no film is lost and if  $D_2$  is the dose at which all of the film is lost, then we define the contrast of the resist by [37]

$$\gamma = |\log_{10} (D_2/D_1)|^{-1} \quad (2.1)$$

For a negative resists, the same expression defines the contrast (see figure 2–10(b))

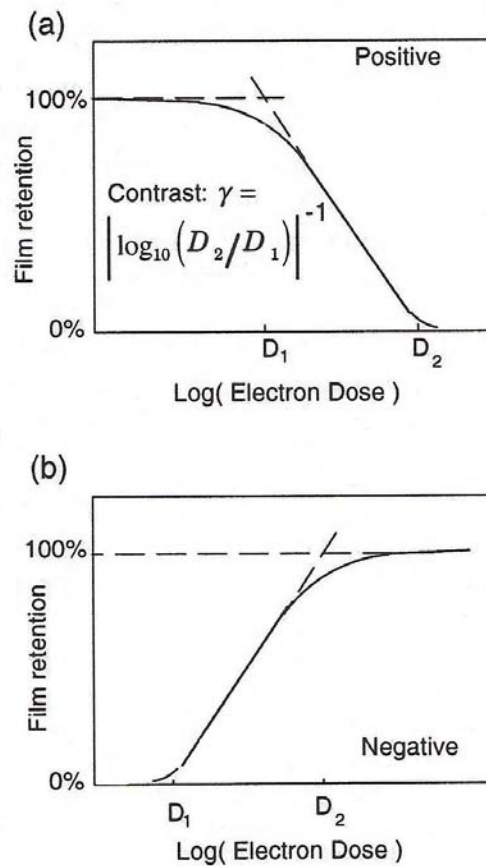


**Figure 2–10:** Film thickness versus exposure dose for (a) positive and (b) negative resist. Contrast is defined as the slope of the linear portion of the falling (or rising) section of the curve [37].

### 2.4.1 Positive Resists

For positive electron beam resists, the pattern exposed by the electron beam will be removed during development. These resists are usually high molecular-weight polymers in a liquid solvent and electron irradiation breaks polymer backbone bonds, leaving fragments of lower molecular weight. As a result, patterns of the positive resist exposed become more soluble in the developer solution.

#### PMMA

Although Polymethyl methacrylate (PMMA) was one of the first resists developed for electron beam lithography, it is still the most commonly used low-cost positive electron beam resist[42]. PMMA is usually found in two high molecular weight forms (495 K or 950 K) in a casting solvent such as chlorobenzene or anisole. PMMA is spun onto the substrate and baked at 170°C. Electron beam exposure breaks the polymer into fragments that are dissolved preferentially by a developer such as Methyl Isobutyl Ketone (MIBK). MIBK alone is too strong a developer and removes some of the unexposed resist. Therefore, the developer is usually diluted by mixing in a weaker developer such as Isopropil alcohol (IPA). A mixture of 1 part MIBK to 3 parts IPA produces very high contrast but low sensitivity. By making the developer stronger, say, 1:1 MIBK:IPA, the sensitivity is improved significantly

with only a small loss of contrast. The exposure dose for a typical electron acceleration voltage of 30 kV is in the range of 50-500  $\mu\text{C}/\text{cm}^2$  depending on the radiation source/equipment, developer, developing time, and pattern density. When exposed to more than 10 times the optimal positive dose, PMMA will crosslink, forming a negative resist. It is simple to see this effect after having exposed one spot for an extended time (for instance, when focusing on a mark). The center of the spot will be crosslinked, leaving resist on the substrate, while the surrounding area is exposed positively and is washed away. In its positive mode, PMMA has an intrinsic resolution of less than 10 nm. In negative mode, the resolution is at least 50 nm.

### **PBS**

Poly(butene-1-sulfone) is a common high-speed positive resist used widely for mask plate patterning. For high-volume mask plate production, the sensitivity of 1 to 2  $\mu\text{C}/\text{cm}^2$  is a significant advantage over other positive resists. However, the processing of PBS is difficult and the only advantage is the speed of exposure.

## ZEP

ZEP is a new chain-scission positive resist developed on poly (methyl-achloroacrylate-co-a-methylstyrene) by Nippon Zeon Co. ZEP provides a high resolution and contrast comparable to PMMA but relatively low dose ( $8 \mu\text{C}/\text{cm}^2$ ) at 10 kV). ZEP also has better etch resistance than PMMA.

### 2.4.2 Negative Resists

Electron irradiation cause negative resists chains cross-linking, making them less soluble in the developer. COP is an epoxy copolymer of glycidyl methacrylate and ethyl acrylate, P(GMA-co-EA), commonly used for negative exposure of mask plates. This is a very high speed resist,  $0.3 \text{ C}/\text{cm}^2$  at 10 kV, with relatively poor resolution (1  $\mu\text{m}$ ). COP also has relatively poor plasma etch resistance and requires spray development to avoid swelling. Because cross-linking occurs by cationic initiation and chain reaction, the cross-linking continues after exposure. Therefore, the size of features depends on the time between exposure and development. Unless speed is very critical, COP is probably not a good choice for a negative resist. NEB-31 is a relatively new resist for electron beam lithography from Sumitomo Chemical, Inc. NEB-31 exhibits high resolution, 28 nm structures, high contrast, good thermal stability, good dry etch resistance, and long shelf-life. SU-8 is a chemically amplified epoxy-based negative resist. Due to its

good chemical and mechanical properties, SU-8 is normally employed to fabricate high aspect ratio 3D structures and serve as a permanent part of the device with the LIGA (a German acronym that stands for deep-etch x-ray lithography, electroplating, and molding) technique. As an electron beam resist, SU-8 is able to generate sub 50 nm structures with 0.03 nC/cm electron dose.

## **2.5 Pattern Processing**

After the patterned resist is exposed, the common procedure for the next step to follow will be transferring the pattern either to the substrate or to a layer added after the lithography. The processing that is used depends on the material system and the final structure that is desired. Sometimes the polymer remains as a part of the device.

### **2.5.1 Coating and Lift Off**

Sputtering and evaporation are the most common used coating methods. A significant difference between sputtering and evaporation is the control over the direction of the deposition material. In a typical sputtering system, the deposition is homogeneous over the substrate surface, with the metal particles arriving on it with a wide range of incident angles, while evaporation is usually nearly directional. Liftoff is the process of removing the resist and the material that has been coated on top of the resist. The material that has adhered to the substrate will then be left, thus producing the desired pattern. The

success of liftoff depends primarily on the adhesion of the coating to the substrate, and whether or not the coating covers the sidewalls of the resist. Generally, an evaporated beam will be collimated enough to leave the sidewalls uncoated, while sputtering is much more likely to coat the sidewalls and make the liftoff step more difficult. For liftoff, it is important to know the thickness of the resist and to keep the coating thickness less than approximately two thirds of the resist thickness.

### **2.5.2 Sputtering**

In sputtering system, ions from a plasma impact a metallic material (target), whose atoms are ejected at all angles. The sputtered material coats the specimen which is placed below the target. The wide range of trajectories of the sputtered material is desirable for coating SEM specimens, since the metal will cover most surfaces and prevent charging during imaging. However, for lithography, it is generally undesirable to coat the sides of the resist walls that define the pattern, because this can cause ragged edges after liftoff or sections of the pattern may not lift off at all if the edges are coated with too thick of a layer. Figure 2–11 shows a schematic representation of sputtering process and a cross section view of a pattern after sputtering has been performed [41].

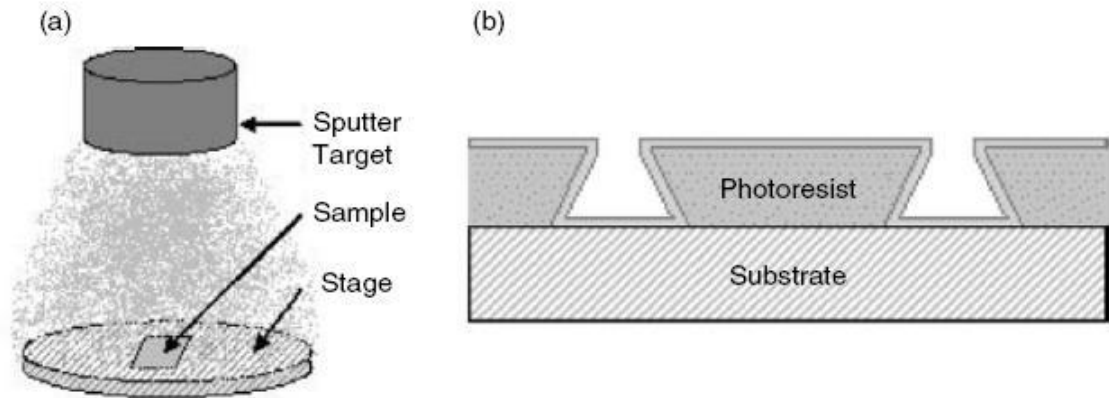


**Figure 2–11:** (a) Is a schematic representation of the sputtering process and (b) shows a cross section view of a pattern after sputtering coating[41].

### 2.5.3 Evaporation

During thermal evaporation, the source material is placed in a boat or a filament coil, which is heated using an electrical current as shown in Fig. 2–12. Electron beam sputtering systems can also be used, which heat a localized spot in the source material using an electron beam. The sample can be placed either above or below the source material depending on the equipment being used. The evaporated material will be nearly collimated, so it is less likely to coat the sides of the pattern as compared to sputtering. This yields cleaner edges after removal of the resist, which is critical in high-resolution patterning. However, even with a collimated deposition, care must be taken to ensure that the deposited material hits at near normal incidence, otherwise the deposited material may coat some of the sidewalls and/or

may not reach the bottom of narrow features that have a high aspect ratio between the resist thickness and the feature size.

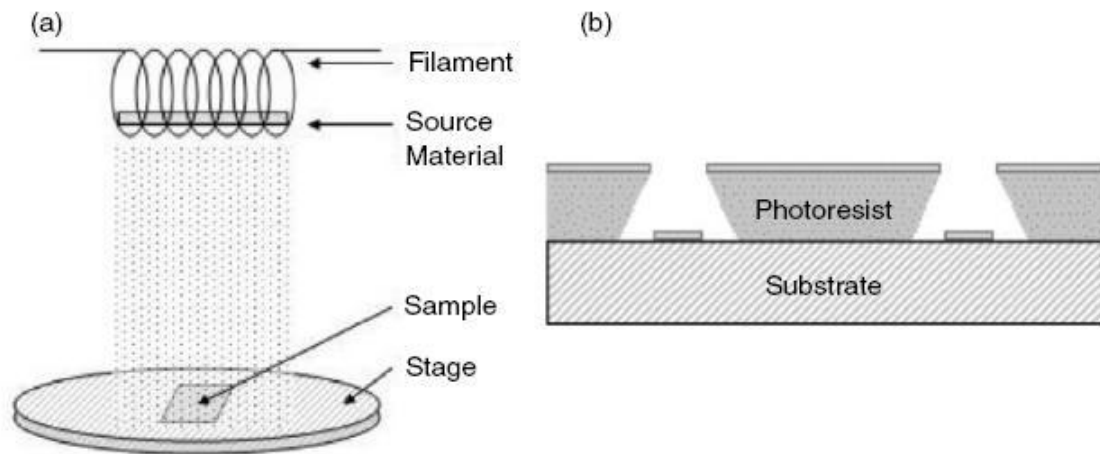


**Figure 2-12:** (a) Shows a schematic of a filament-style evaporation process; a boat is similar except that the sample is above the source material; and (b) shows a cross section view of the pattern after it has been coated using evaporation[41].

# **CHAPTER 3**

## **EBL NANOFABRICATION OF PROPOSED METAL/POLYMER SUBSTRATES FOR SERS**

### **3.1 Materials**

Single crystal silicon was used as the substrate for EBL. PMMA and MIBK:IPA 1:3 from Micro-Chem. were used as e-beam resist and developer, respectively. The EBL tool is a JEOL 6390 SEM, which has a thermionic electron source (tungsten filament), and the highest acceleration voltage that can be achieved is 30kV. The patterns are designed in DesignCAD Express V16, and then transferred to NPGS software converter.

### **3.2 Experimental procedure**

#### **3.2.1 PMMA Spin Coating**

15x15mm chips are obtained after cutting a whole single crystal wafer using a diamond tip pencil. To clean the chips, a solution of 20ml of distilled water with 1ml contrad is prepared in a beaker. The chips are immersed in the solution and sonicated for 5min. The same procedure is repeated with distilled water only, acetone, and Isopropyl Alcohol (IPA). The chips are blown with Nitrogen and then baked at

180°C to evaporate any residual moisture. The chip is then placed in the spin coater, and 2–3ml of PMMA is dispensed manually (with a dropper). The chip is spun at 1800rpm at high acceleration rate, according to the resist manufacturer. Figure 3–1 shows the relationship between spin speed and thickness for 950 and 495 PMMA. The curves corresponding to C2 belong to the polymers used in the process.

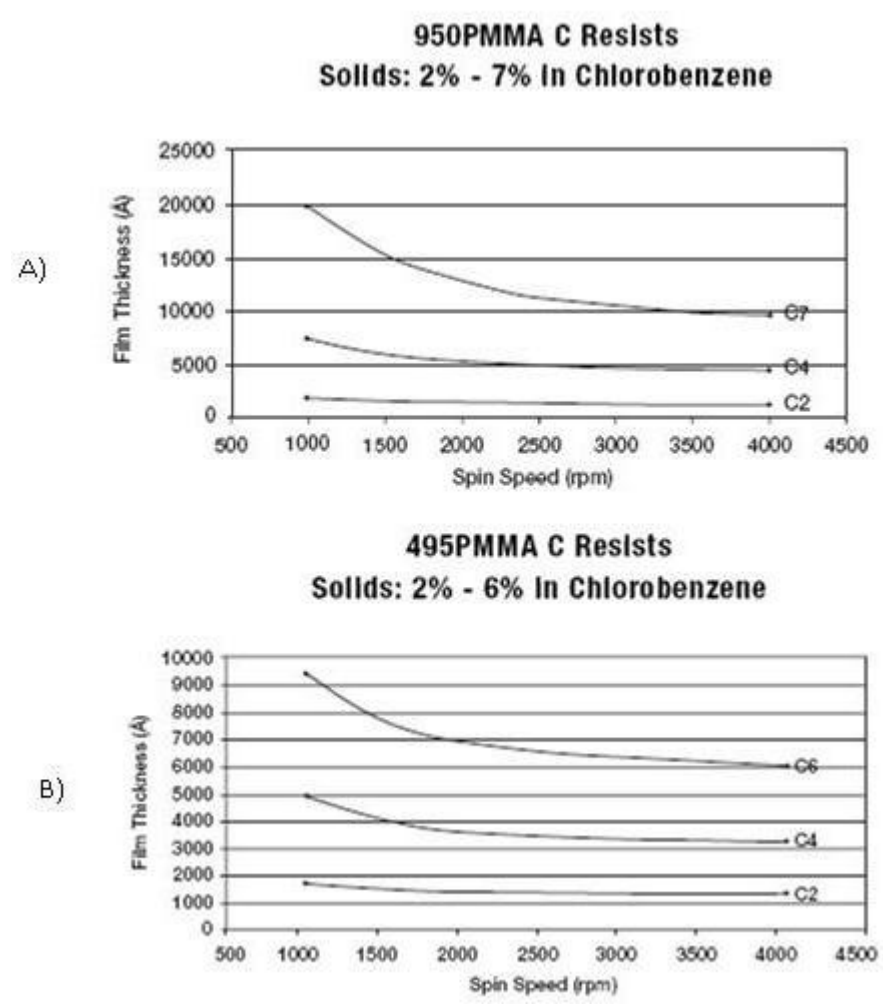


**Figure 3–1:** 950K (A) and 495K (B) PMMA thickness vs rpm curve.

A single layer of 950K PMMA and a bilayer system with a 950K PMMA on top of a 495K PMMA layer were used to observe the lithography performance. Both, the single and bilayer system configuration were exposed to the same EBL conditions, that will be presented in a subsequent section. After the polymer is spin coated, the substrate is soft baked to evaporate any residual solvent. Two different baking times were used, 90 and 180 seconds. After all this process has been completed, the polymer can be exposed to the e-beam.

### **3.2.2 Patterns Design and Processing**

Patterns design were obtained using DesignCad Express V16. A series of Hexagonal, Elliptical, triangular, and square patterns have been designed. Each shape has variations in gap, configuration and/or aspect ratio. To get 50nm in interparticle spacing, the contour of the figure is exposed, and then developed to leave the desired shape. The resulting e-beam distribution diameter (including additional PMMA exposure due to backscattered electrons arriving at the polymer surface after returning from the substrate) exposing the PMMA gives the desired dimension. The gap is also affected by the dose applied to the pattern, resulting in larger gaps at higher doses. The drawing has been designed in a way that the beam passes only once in each line. The line has no width, but the beam does, therefore each pattern has been oversized by 50nm to get the final desired dimensions. Figure 3-2(A)

shows the UPRM seal made with Design CAD V16. Figure 3–2(B) shows the lithography result. The design used for the honey combs is

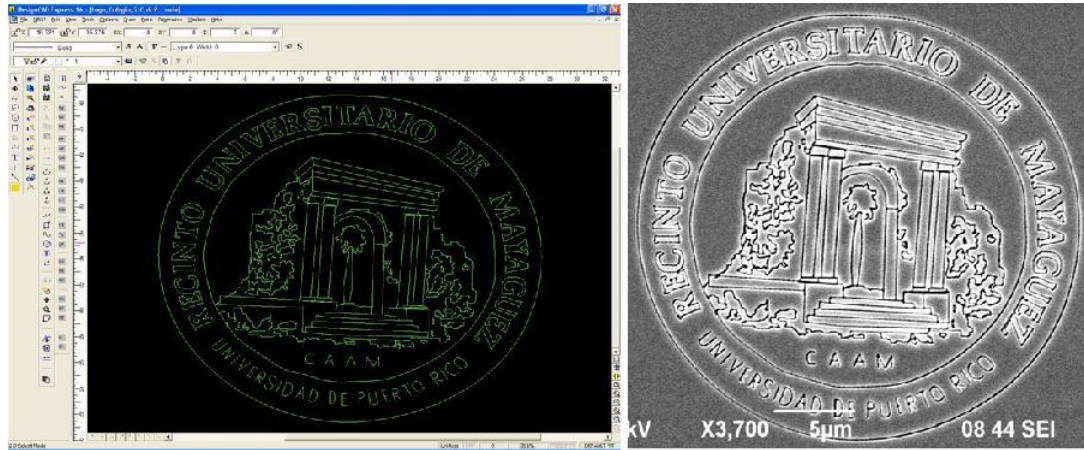


**Figure 3–2:** Design CAD drawing of University of Puerto Rico at Mayaguez seal (left) and a SEM image of the lithographically defined pattern on PMMA (right).

presented in figure 3–3. The dashed lines represent the e-beam beam path, while the gray areas represent the real size shape in the polymer after exposure due to the effective beam diameter ( $\sim 50\text{nm}$ ). The orange areas are those developed away after exposure. The rest of the shapes were designed in the same way, except for the ellipses. For the ellipses there was a shape modification in the design. The shape modification method to correct proximity effect in EBL was presented in chapter 2. For the ellipses, the concept of this method was applied. The sequence of the design for this pattern is exposed in figure 3–4. The design begins by drawing an ellipse with the desired final shape and size. It is desired to obtain an aspect ratio of 3:1 in the ellipse, with a major axis of 170nm. After the ellipse is drawn, a rectangle

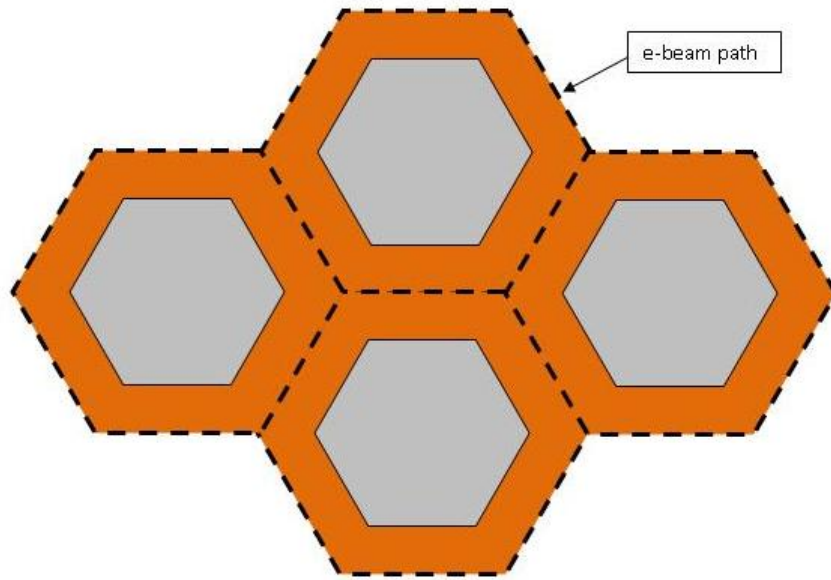


**Figure 3–3:** Hexagons design for EBL writing.

is written outside the ellipse, tangent to the top and the side curves. Then the tips of the ellipses are modified as shown in the figure 3–4, obtaining the final design for the pattern. This pattern is oversized by 50nm with a  $\Delta a$  and  $\Delta b$  of 25nm, to compensate for proximity effect, which as mentioned before, gives a final exposure diameter of approximately 50nm in the PMMA. In the same way as in figure 3–3, the dashed lines represent the beam path. The critical areas at the corners receive additional dose, which will become rounded when developed. Finally the shape that will be produced is elliptical as is shown later in the lithography results. The resulting pattern is elliptical as will be shown in the lithography results section.

To obtain gap variation in the patterns, different designs were created. To obtain features with 100nm in spacing, the patterns are

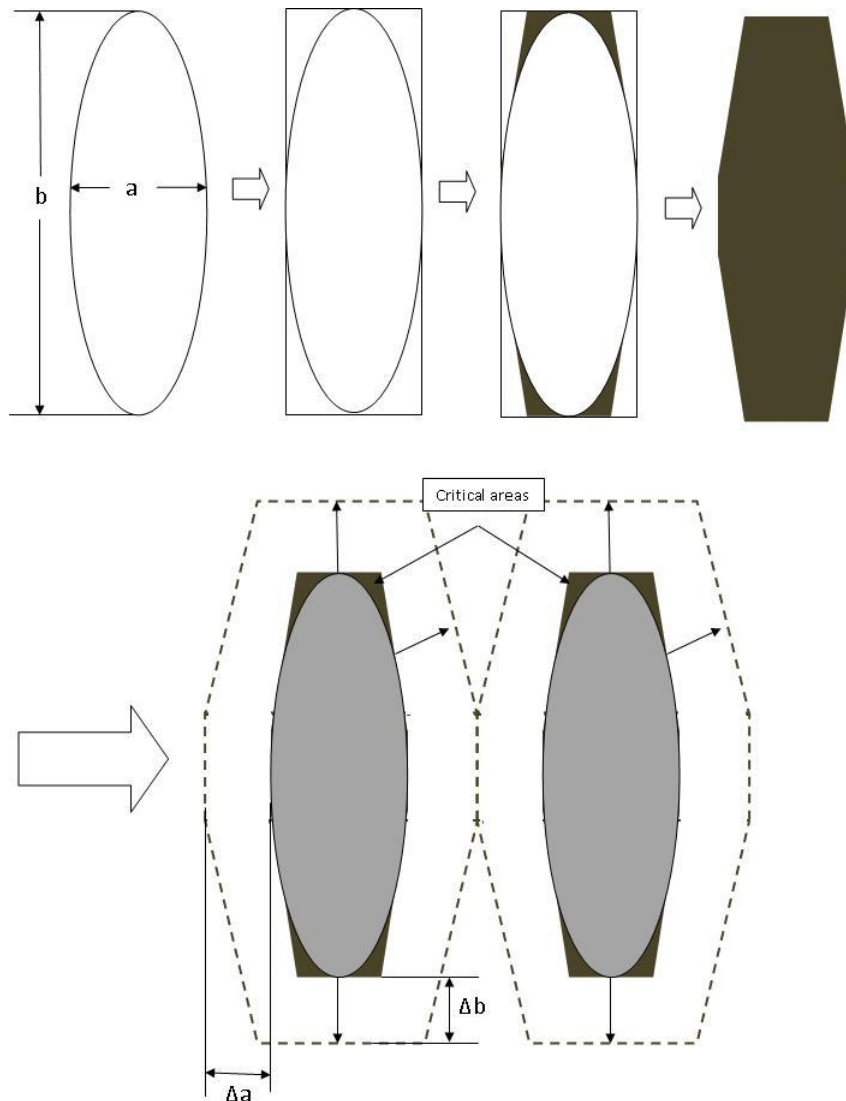


**Figure 3-4:** Sequence of the ellipses design for EBL writing. A shape modification was utilized to make the patterns.

spaced 50nm in the drawing, and with the beam diameter, the final spacing will be 100nm. To obtain 150nm gap between features, the patterns are spaced 100nm, and between pattern a line is introduced to complete the exposure in the desired spacing area (see figure 3-9). This line is set to a different color to allow dose variation between pattern lines and spacing lines. After the pattern has been drawn, it is

then converted to a NPGS run file, where all the exposure parameters are introduced in order to produce the EBL patterning. Figure 3–5 shows a typical run file configuration.

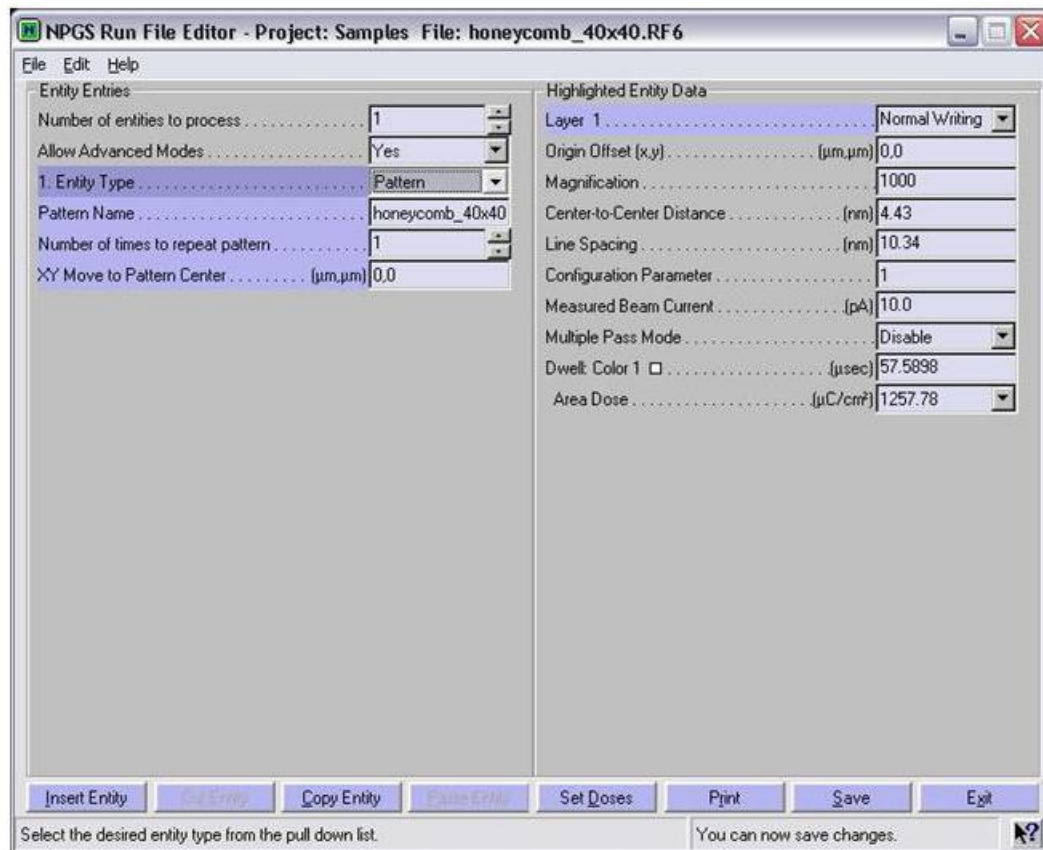


**Figure 3–5:** Run file configuration. All parameters are introduced here to make the EBL writing.

### 3.2.3 Microscope optimization

Once the run file is ready, a microscope optimization step is needed in order to write the pattern correctly. To achieve this, a  $\sim 1$ –2mm long scratch is made on the top of the chip in the center part as shown in figure 3–6. This gives a spot to focus the beam, correct the astigmatism, and locate the patterns when observing. This scratch is

taken as the reference point, because of the fact that the patterns will be written 1mm below this point.

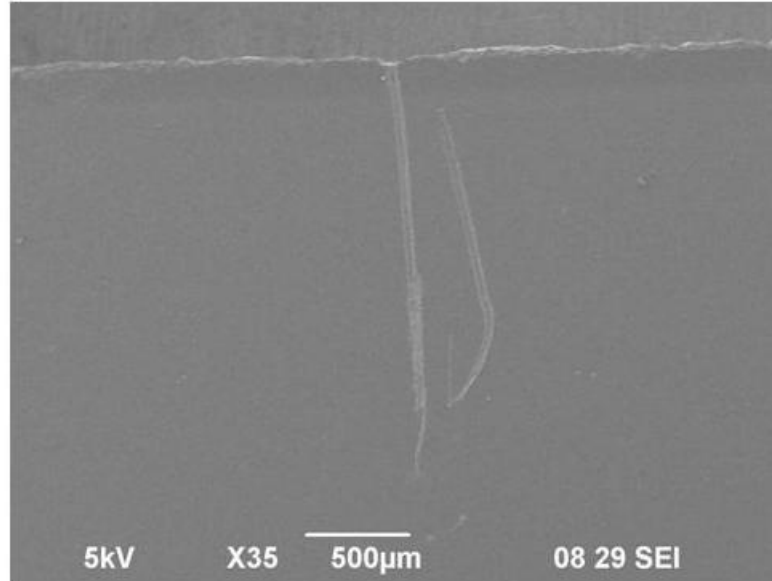


**Figure 3–6:** Scratch made on the polymer substrate to take as reference point.

Two additional scratches are made at both sides of the chip to focus on. This will give NPGS the focus values at different places. NPGS uses these values to create a matrix to calculate the focus variation with location, adjusting the correct value for each location when writing. The reference point and the additional scratches coordinates are manually taken, at low kV. Then the microscope is taken to 30kV to correct the focus and astigmatism in any dust present on the chip near the reference point. Before writing a pattern, it is necessary to check the beam optimization. This can be done by taking an image of a spot contamination made by the beam over the polymer surface. If we obtain an image of a rounded, small spot, we can be sure that

the beam is properly optimized. If we get a large or noncircular spot, we must optimize the microscope until we get the circular, small spot image over the resist. The left side of Figure 3-7 shows a beam without astigmatism correction and out of focus. The right side of Figure 3-7 shows the image of a spot contamination produced by an optimized electron beam (well-focused and stigmatized). If the astigmatism

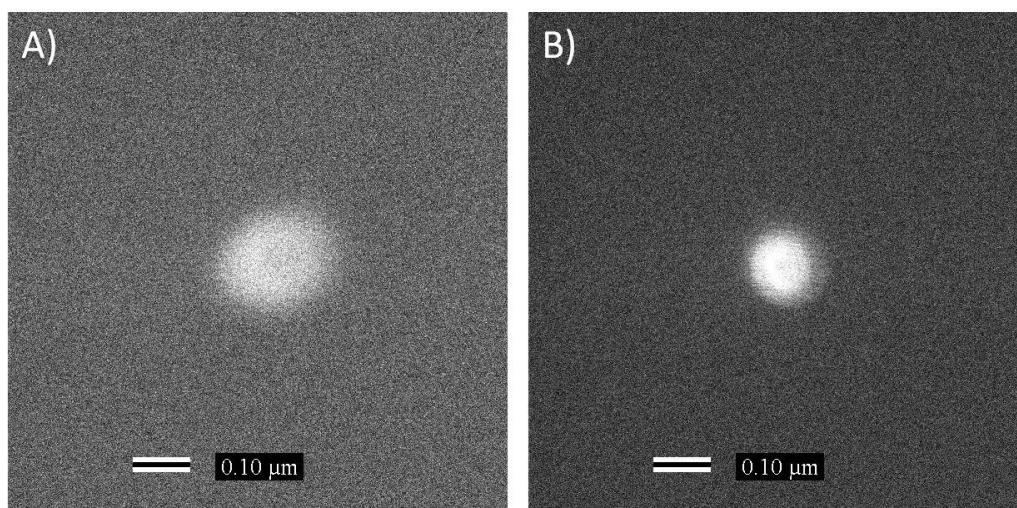


**Figure 3-7:** Example of a spot contamination for a non optimized beam (A) and a focused beam with astigmatism correction (B).

is not properly corrected before doing lithography, a wheel pattern provided by NPGS will appear like in figure 3-8 (A). In this figure some lines appear underexposed in one direction and other lines appear well exposed in other direction. In figure 3-8 (B) the lines have the same dose in all directions due to the fact that the astigmatism was properly corrected.

The wheel is a good pattern to write when doing lithography for the first time, to get the ability of optimizing the e-beam correctly.

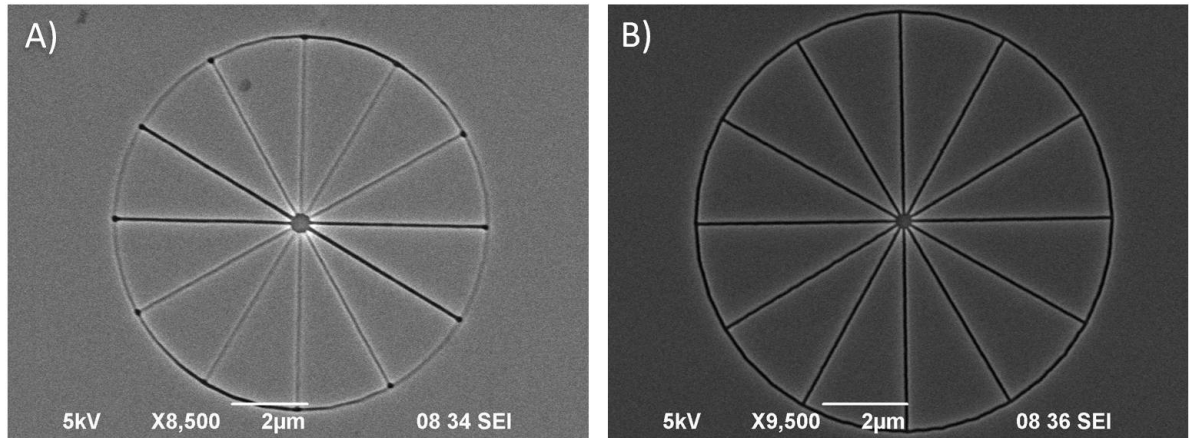


**Figure 3–8:** A) Pattern that shows the effect of astigmatism. B) Pattern performed by a well optimized beam.

### 3.2.4 Exposure Details

All patterns were exposed at a magnification ranging from 1000 to 1700X. The working distance and accelerating voltage were held constant at 8mm and 30kV respectively. For the 50nm interparticle spacing, the proximity correction was done by exposing the desired feature over a range of doses, until the patterns came to a proper size. The dose were varied between 0.2–1nC/cm. For patterns where the desired gap was larger than 50nm, a line between patterns was introduced with a different color, to allow dose variation. For this configuration, the dose were varied in a combined manner between the pattern and the filling line. The beam current for EBL was varied between 5 and 30pA, in order to get the optimum beam diameter, and to get the final features dimensions. Figure 3–9 is an example of square patterns that were designed to obtain a 150nm spacing between

features. The main squares are in yellow and are assigned a dose, and

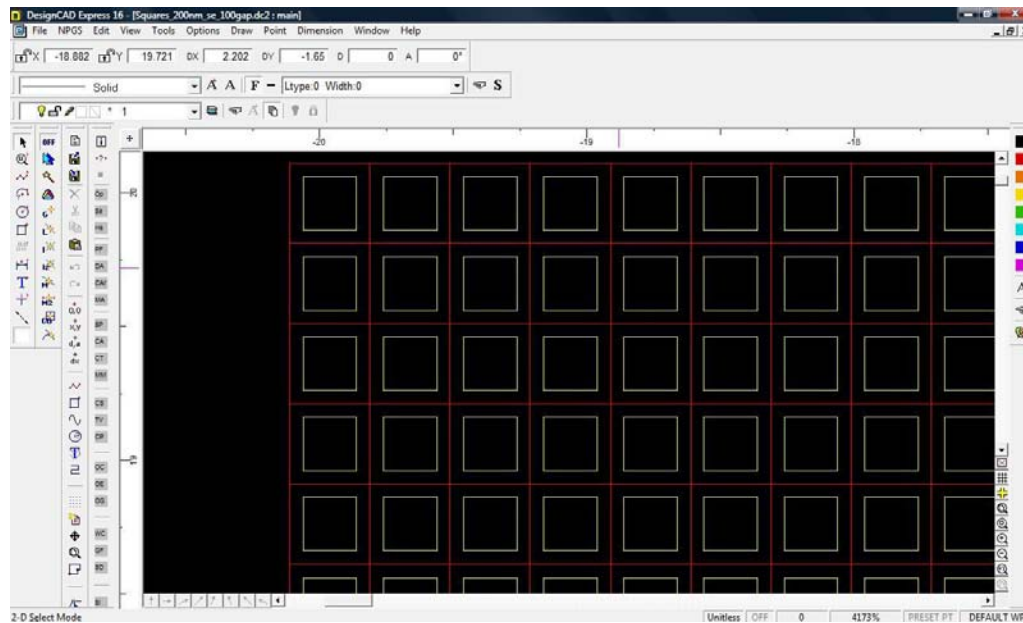


**Figure 3–9:** Square patterns design for 150nm in features gap. The yellow lines are assigned a dose, and the red ones are assigned a different dose to develop away the gap between the squares.

the outer squares in red and are assigned a different dose. The goal is to leave the squares in yellow and remove the gap between them by adjusting the dose of the red lines. So a combination of doses is applied between yellow and red lines. The same procedure for varying gap of other patterns is applied, especially for hexagons and ellipses. When the run file for these patterns has been created, the dose for each color is asked. For the case of rectangles, the line at top is set to a red color to adjust the dose at this side of the pattern (see Figure 3–10). The reason for that color change was, that the lithographic observation showed that the top line was overexposed due to proximity effect; hence the dose at this line was reduced.

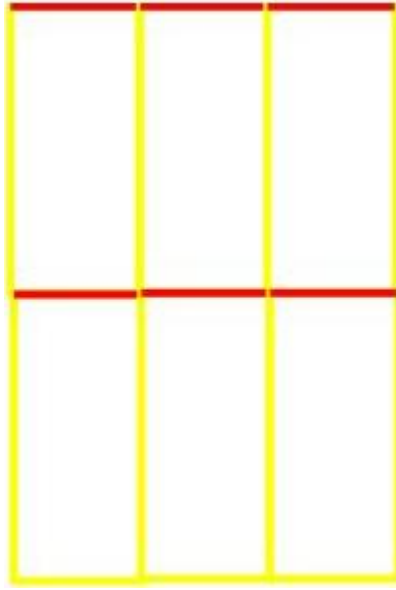


**Figure 3–10:** Rectangles design. The top line is set to a different color to change the dose.

### 3.2.5 PMMA Developing

After beam exposure, the chip is submerged in the developer which in this case is MIBK:IPA 1:3. Two different developing times were used: 90 and 120sec. After developing, the chip was submerged for 60sec in IPA and finally for 30sec in distilled water. After this process, the chip was post-baked for 30sec to eliminate remaining developer or moisture.

## 3.3 EBL patterns results

### Beam Current

The beam current, as mentioned previously, is related to the diameter of the beam exposing the polymer. After doing e-beam lithography with a range of beam current between 5 and 30pA, it was observed that a range of 7–10pA was the most favorable to obtain the

finest linewidths. The effect of a high beam current on the final particles spacing can be seen in Figure 3–11. For this honey comb pattern, the original drawing was 250nm in side, and as can be seen, the final side dimension is 100nm, but with a gap of near 200nm. This is consistent with the fact that increasing the spot size the beam diameter increases, therefore linewidth will increase.

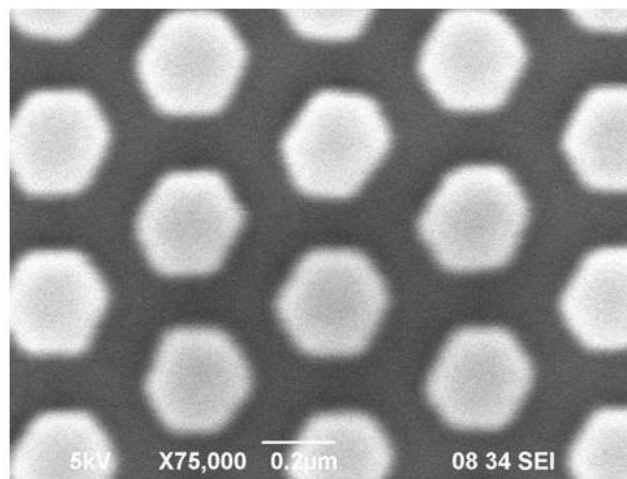


**Figure 3–11:** Honey Comb patten written with a beam current of 25pA

It was observed that for beam currents above approximately 15pA, the effect became more marked with increasing beam current. It implies that above this current, a slight increase in beam current, represented a big increase in beam diameter.

### **Dose**

It was previously mentioned that due to the high symmetry and uniform density of most patterns, the correct dose for them was determined experimentally by applying a series of doses, from lower values

to higher values, until the pattern was developed with the proper size and shape. The sequence of a hexagonal pattern optimization is presented in Figure 3–12.

It is observed in the figure that a low dose, results in underexposed lines between hexagons, where the polymer does not develop its complete thickness. Gradually increasing the dose value, the polymer thickness was reduced, until all lines were well defined. For the particular case of the hexagonal pattern, the optimum dose was found to be 0.45nC/cm. The same procedure was applied to the rest of the

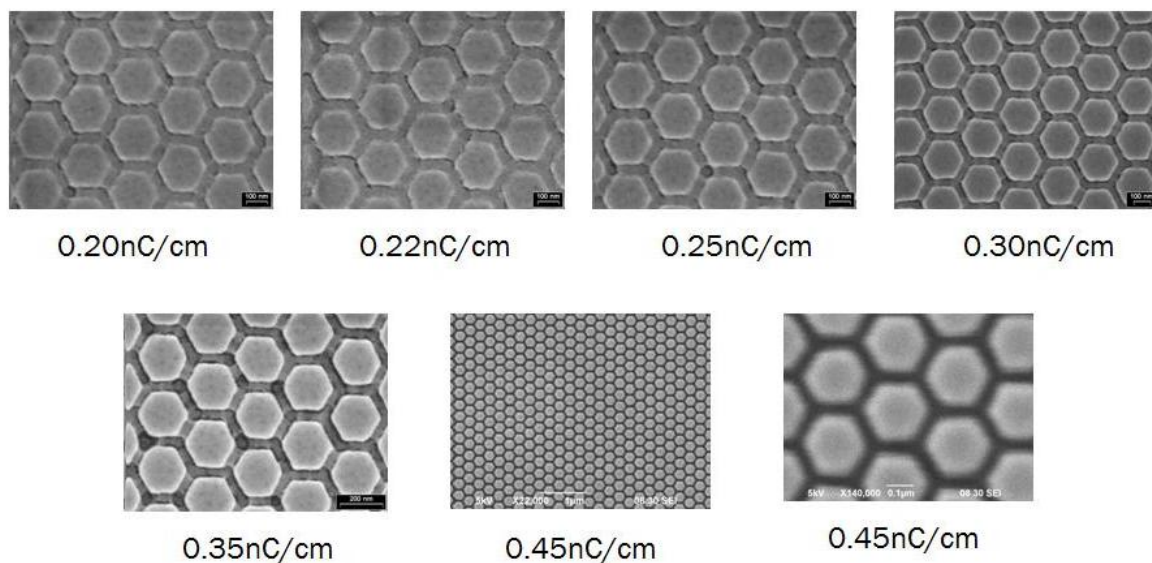


**Figure 3–12:** Sequence of the hexagonal pattern optimization.

shapes.

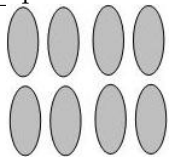
Tables 3–1 to 3–5 present the final dose that must be applied to each pattern to achieve the required shape and size. The figure in each table represents the final shape of the patterns after exposure. Unless

other dimensions are specified, the side dimension of each pattern is 100nm. In case of the ellipses, the minor axis dimension is 60nm and for the rectangles is 100nm.

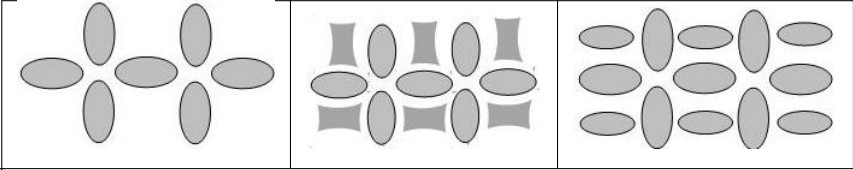
**Table 3–1:** Final dose requirements for hexagons and squares.

Gap (nm)	dose (nC/cm)			
	yellow	red	yellow	red
50	0.4–0.45	–	0.5–0.55	–
100	0.4	–	0.4–0.45	–
150	0.33	0.28	0.45	0.25
200	0.35	0.25	0.45	0.35

**Table 3–2:** Final dose requirements for ellipses.

						
<b>Gap (nm)</b>	<b>dose (nC/cm)</b>					
	Aspect ratio		Aspect ratio		Aspect ratio	
	3:1		4:1		5:1	
	yellow	red	yellow	red	yellow	red
50	0.3–0.35	–	0.35	–	0.38	0.35
100	–	–	0.38–0.4	–	0.4	–
150	–	–	0.38	0.35	0.38	0.35
200	–	–	0.38	0.35	0.38	0.35

**Table 3–3:** Final dose requirements for different elliptical configurations.

			
gap	<b>dose (nC/cm)</b>		
50 (nm)	0.3–0.33	0.35	0.25

**Table 3–4:** Final dose requirements for stars and triangles.

Gap (nm)	dose (nC/cm)	
	130nm side length	
	130nm side length	130nm side length
50	0.25–0.38	0.3–0.35

**Table 3–5:** Final dose requirements for rectangles.

Gap (nm)	dose (nC/cm)					
	3:1		4:1		5:1	
	yellow	red	yellow	red	yellow	red
50	0.53	0.45	0.5	0.45	0.53	0.45

### Single Layer and Bilayer System

After writing the patterns with a single layer of 950K PMMA and with a bilayer coating with 450K PMMA as the bottom layer, it was observed that the single layer configuration was the best option. The bilayer system was used as a method for proximity correction method, but the thickness of the bottom layer coating was not enough to absorb the backscattered electrons, thus the total thickness of the resist was unfavorable for EBL. Figure 3–13 shows a 40x40 $\mu\text{m}$  field of hexagons

written with the bilayer coating. As can be seen in the figure, some polymer areas appear dislodged from the substrate.

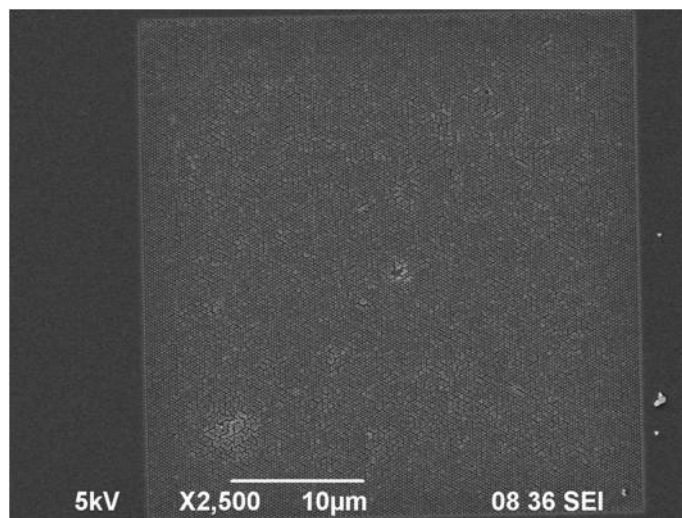


**Figure 3–13:** Field of hexagons written with a bilayer system.

### Soft Baking Time

A better adhesion was observed at a baking time of 180s than at 90s. Figure 3–14 shows the difference in the patterns adhesion between 90s (A) and 180s (B) of baking time.

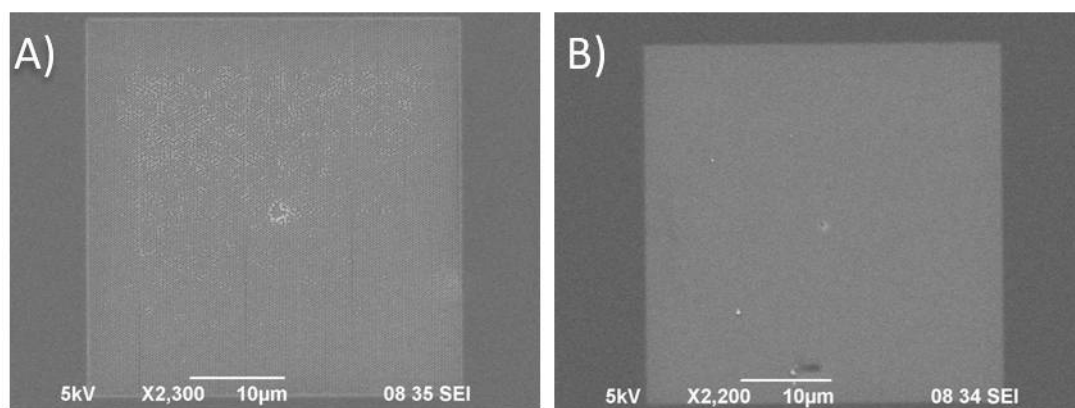


**Figure 3–14:** Difference in patterns adhesion at a baking time of 90s (A) and 180s (B).

### 3.3.1 Patterns Observation

After the development, the patterns are observed in the JEOL 6390 SEM at low kV. A thin layer of gold is sputtered on the substrate to allow observation. Most of the images are taken at low kV to avoid damage in the patterns. The patterns that are observed are not used as SERS substrates. For SERS substrates the deposition method and the metal used are evaporation and silver respectively. The following figures show the final patterns with the experimentally determined dose needed to achieve the required features.

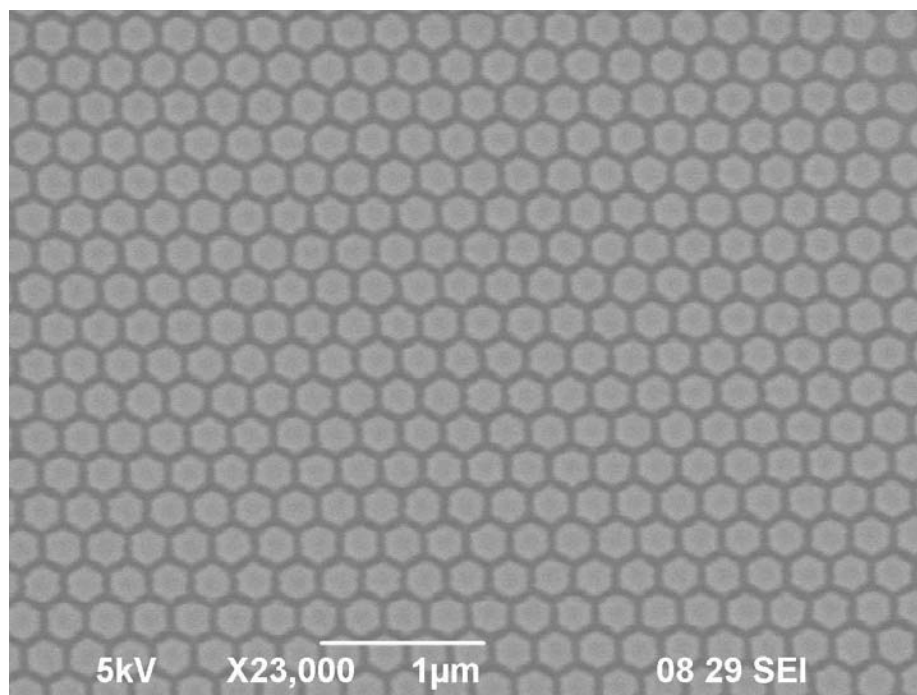


**Figure 3–15:** Hexagons with 50nm in spacing

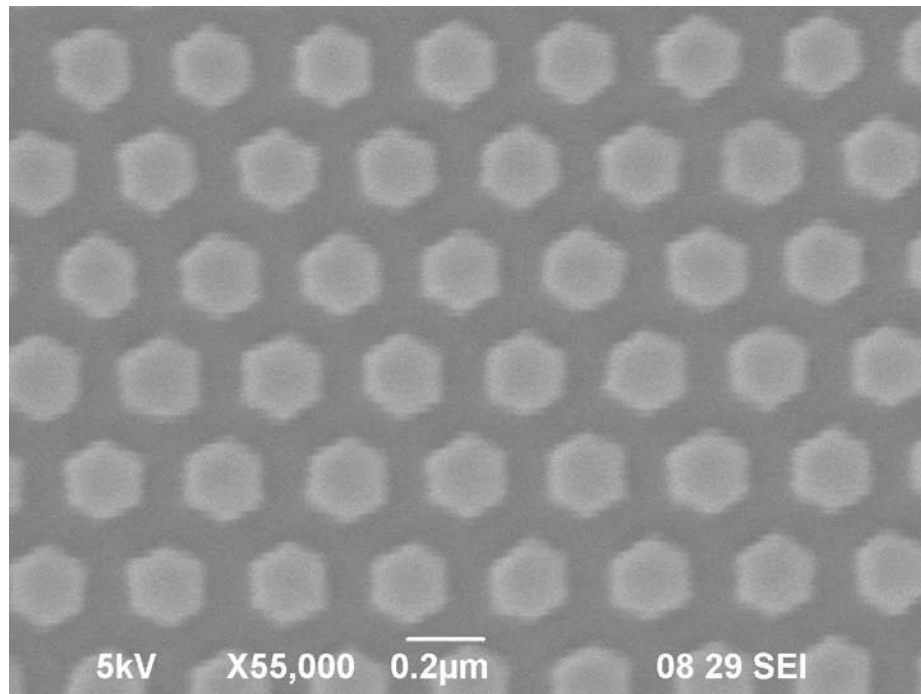


**Figure 3-16:** Hexagons with 100nm in spacing

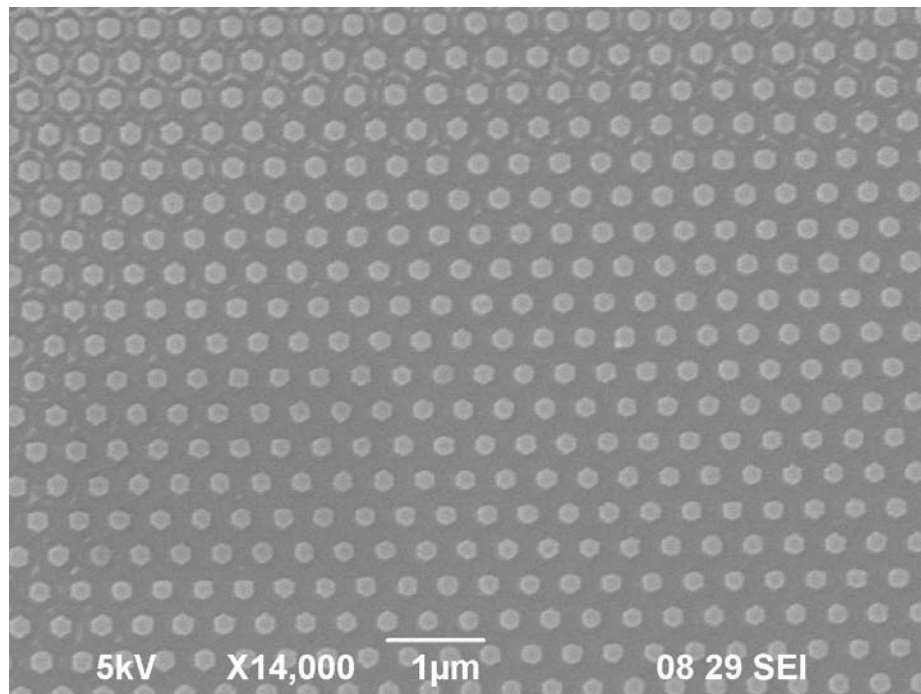


**Figure 3-17:** Hexagons with 150nm in spacing

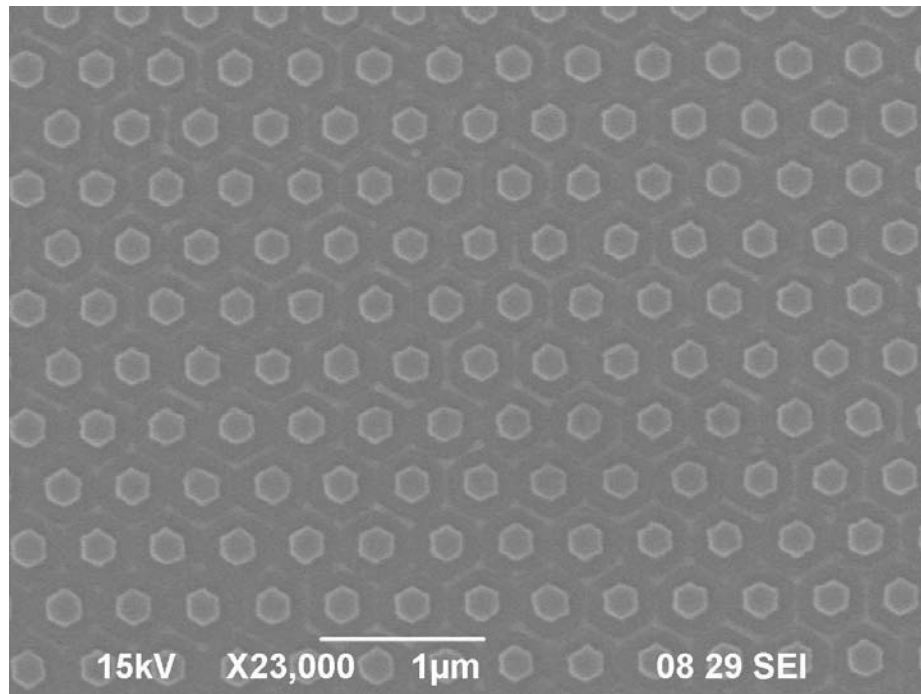


**Figure 3–18:** Hexagons with 200nm in spacing

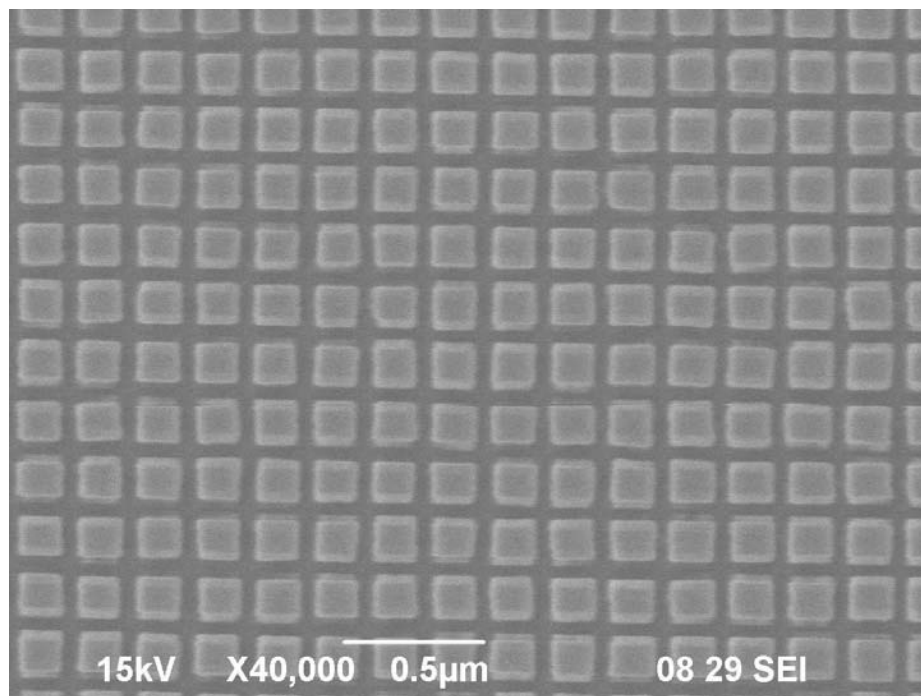


**Figure 3–19:** Squares with 50nm in spacing

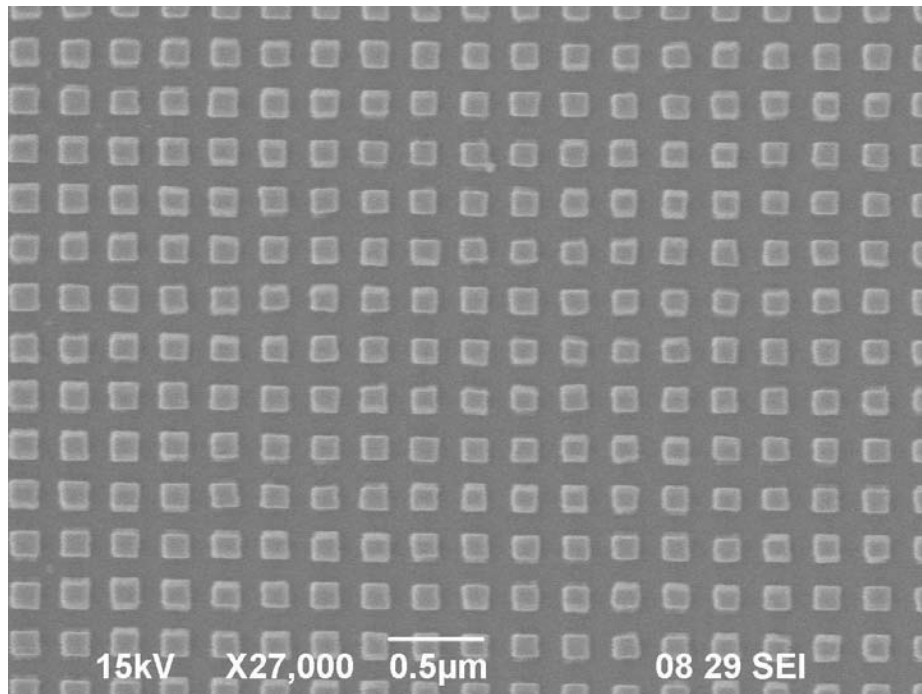


**Figure 3–20:** Squares with 100nm in spacing

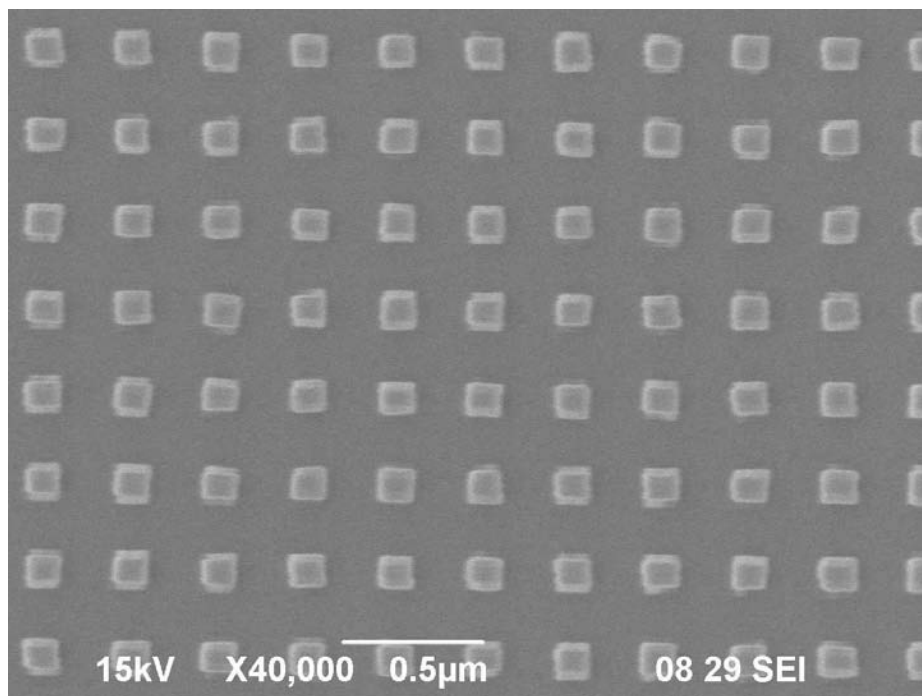


**Figure 3–21:** Squares with 150nm in spacing

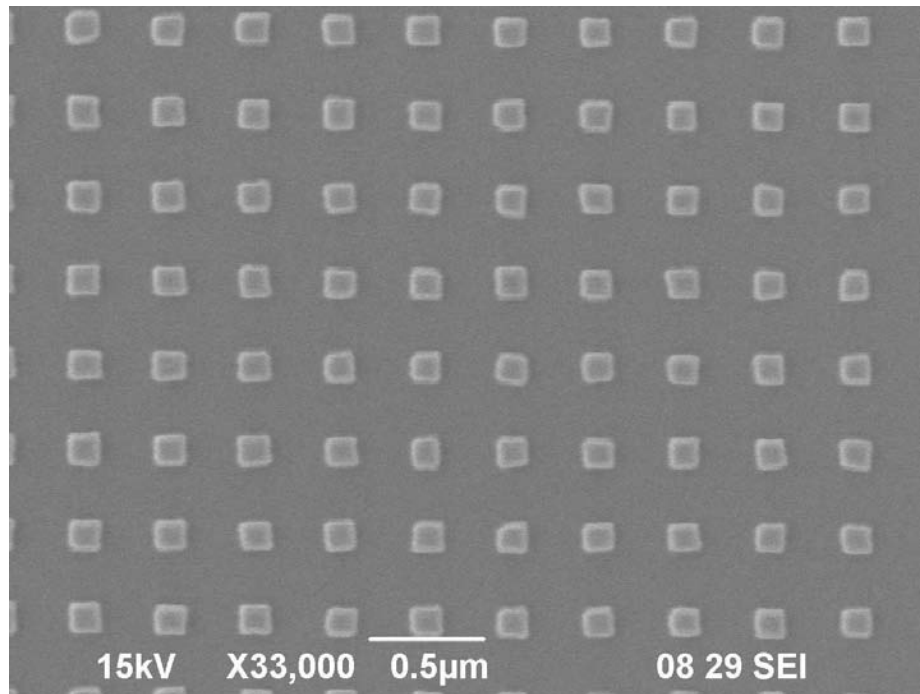


**Figure 3-22:** Squares with 200nm in spacing

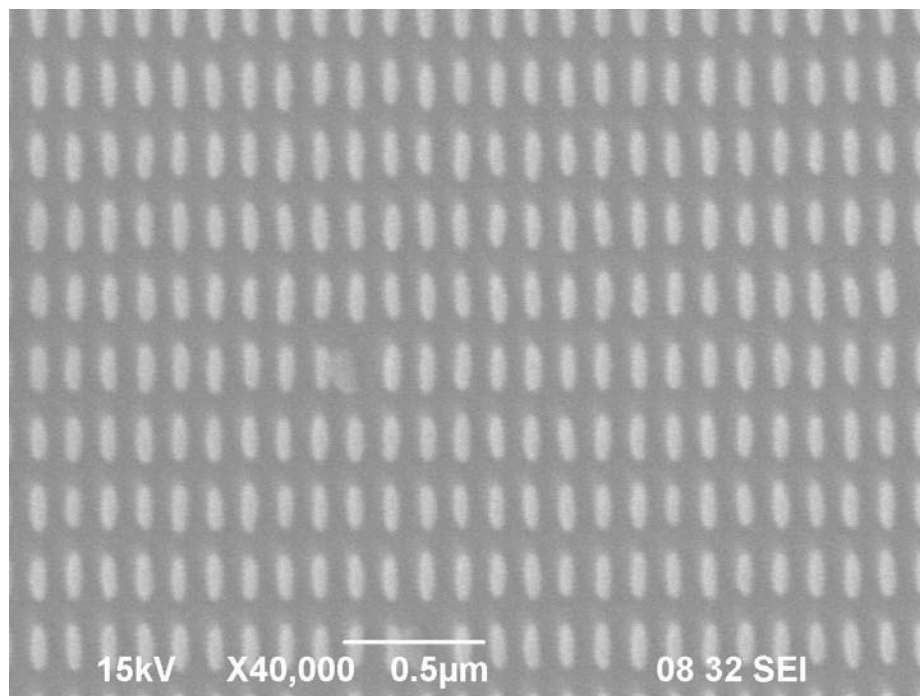


**Figure 3-23:** Ellipses 3:1 with 50nm in spacing

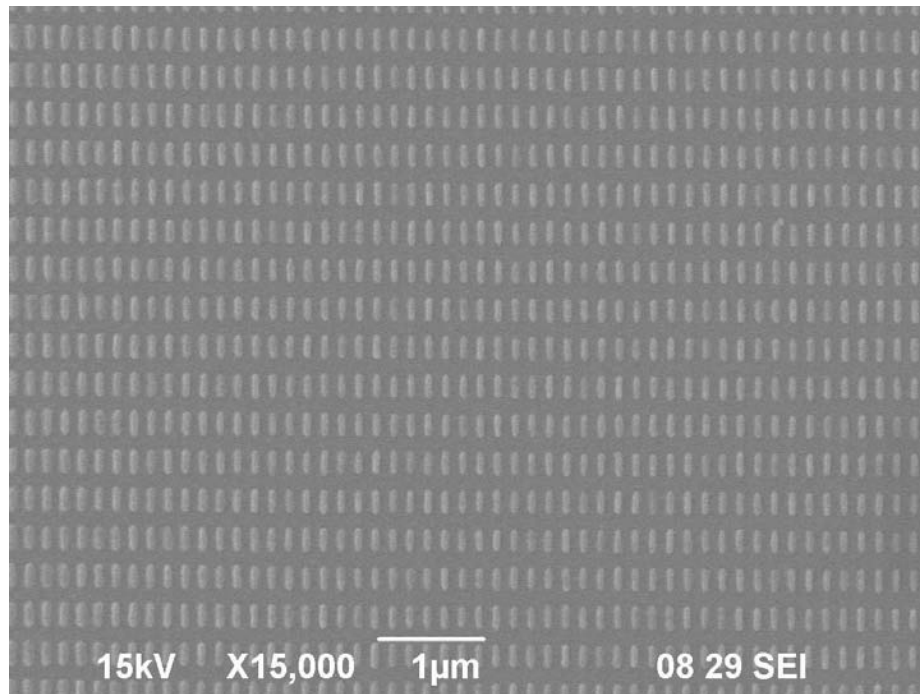


**Figure 3–24:** Ellipses 4:1 with 100nm in spacing

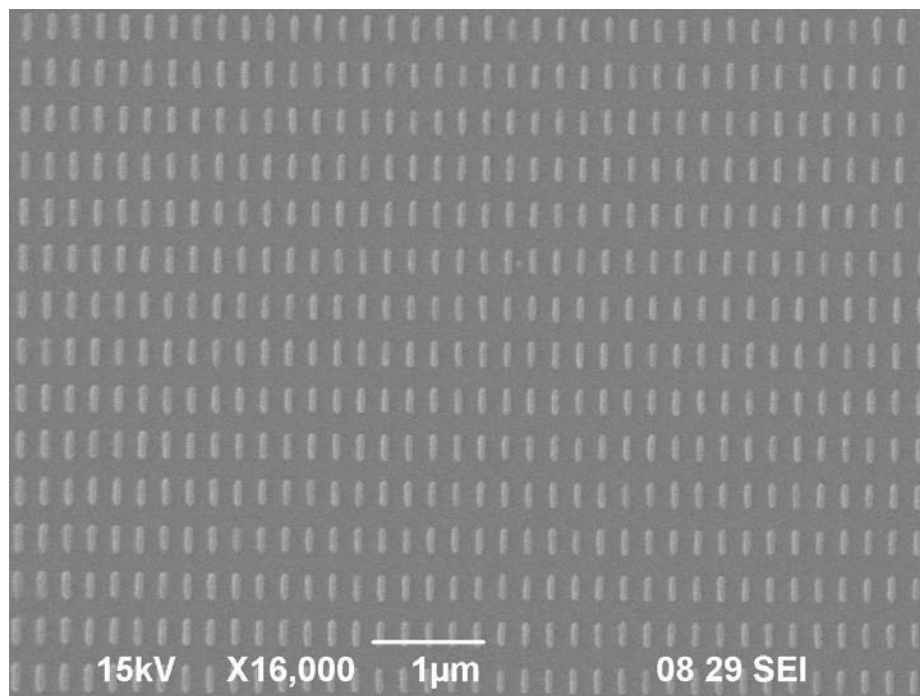


**Figure 3–25:** Ellipses 4:1 with 150nm in spacing

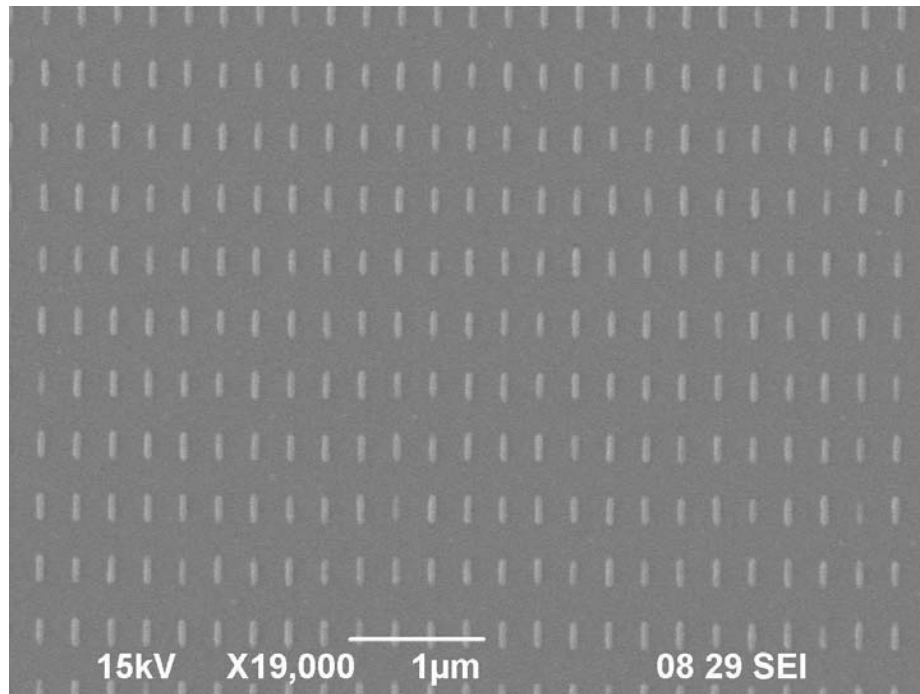


**Figure 3–26:** Ellipses 4:1 with 200nm in spacing

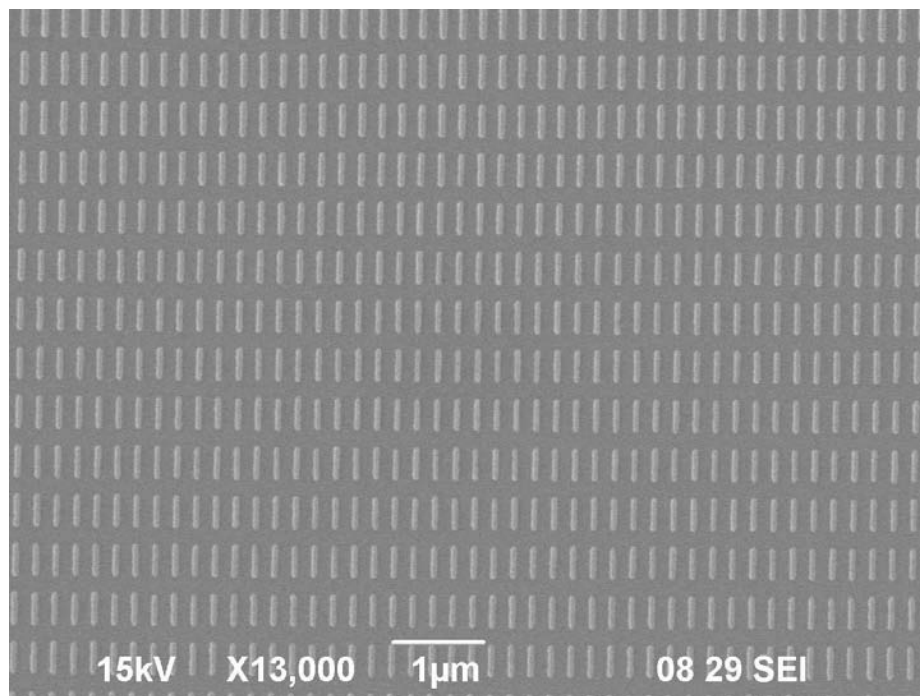


**Figure 3–27:** Ellipses 5:1 with 150nm in spacing

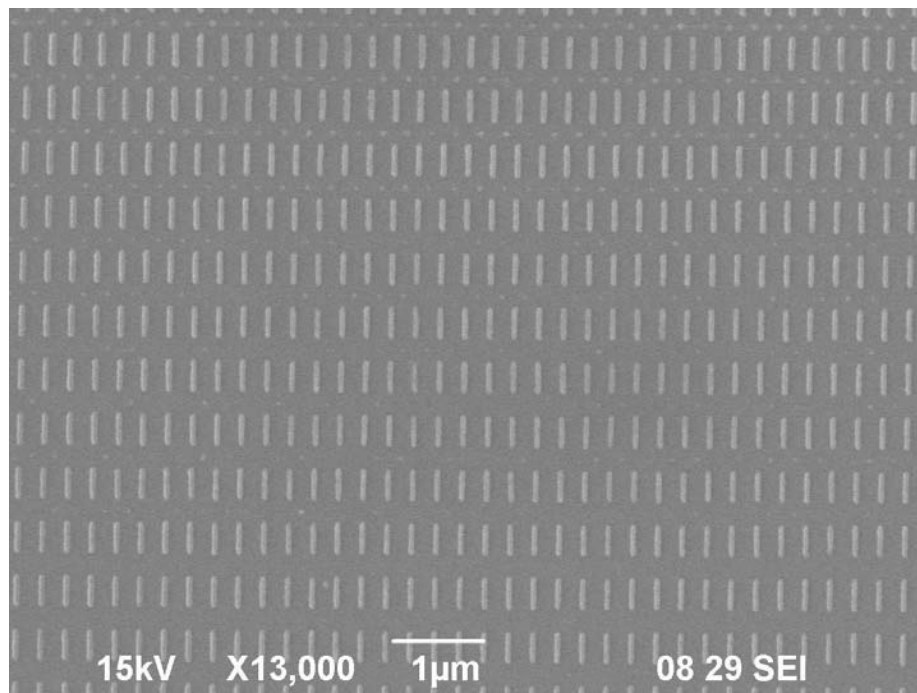


**Figure 3–28:** Ellipses 5:1 with 200nm in spacing

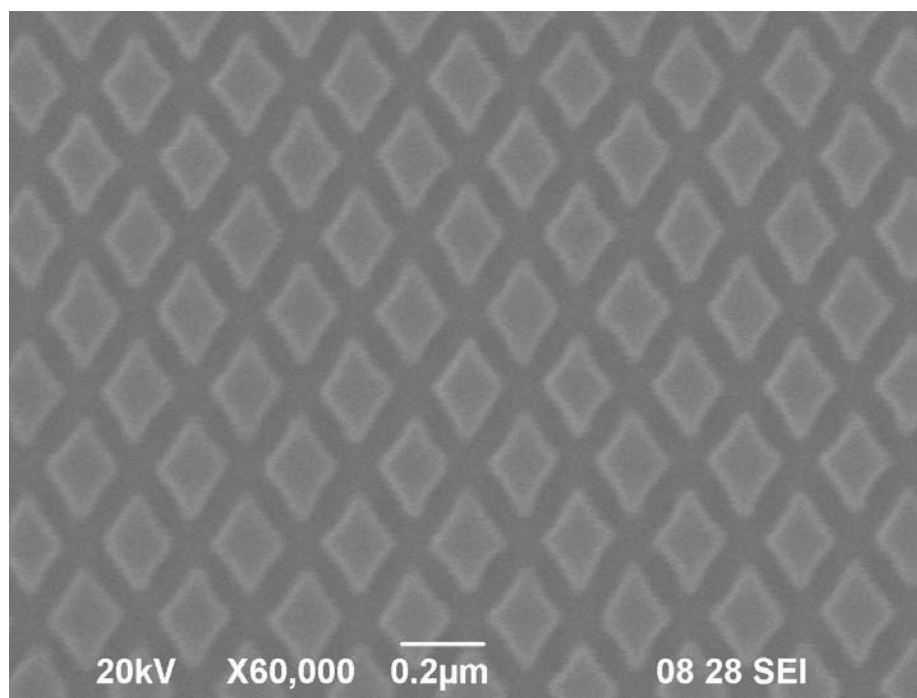


**Figure 3–29:** Stars with 50nm in spacing

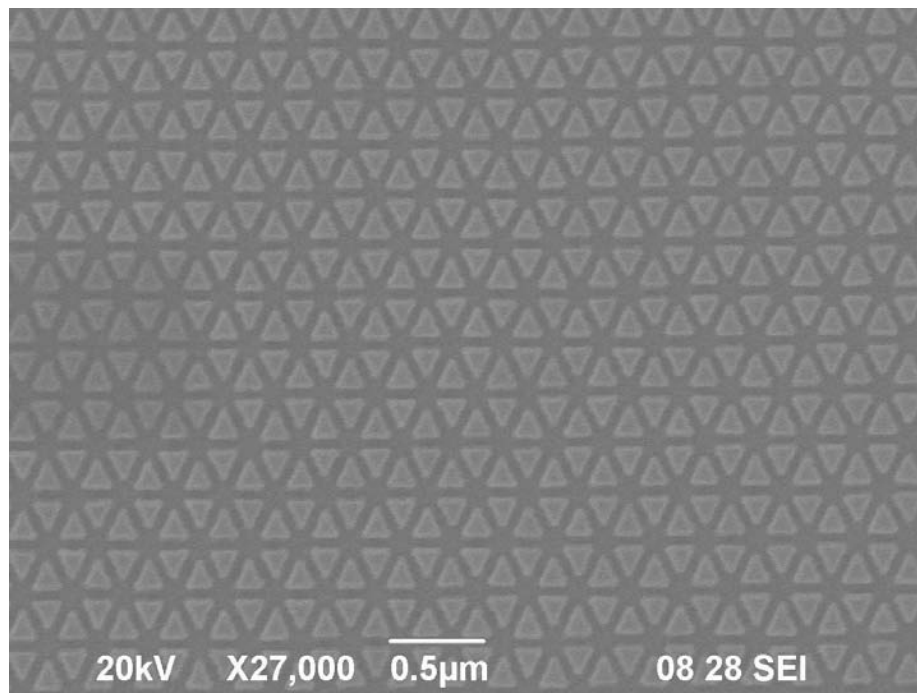


**Figure 3-30:** Triangles with 50nm in spacing

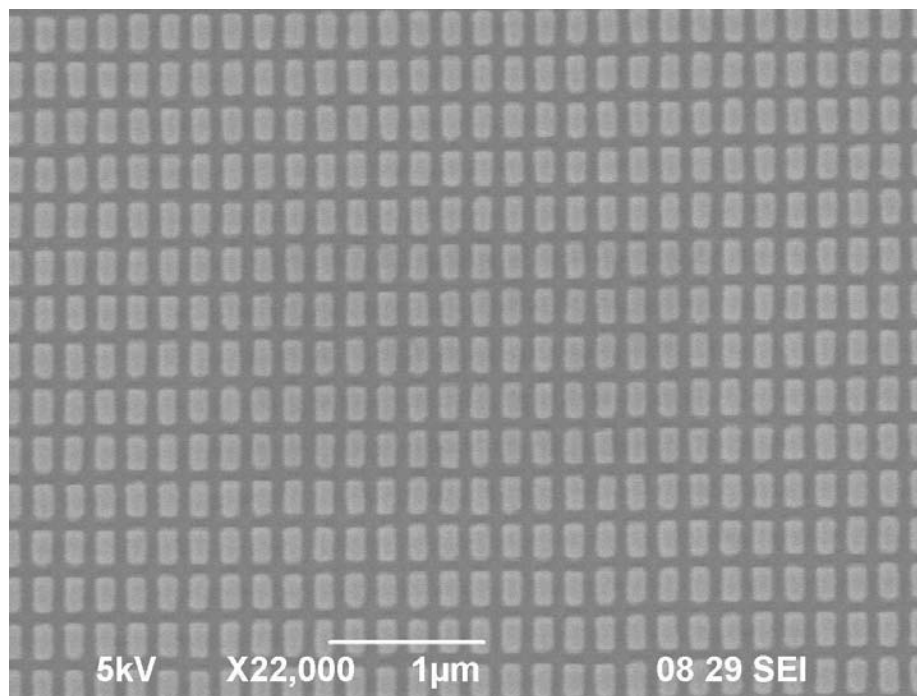


**Figure 3-31:** rectangles 2:1 with 50nm in spacing

## CHAPTER 4

# RAMAN SPECTRA ACQUISITION USING PROPOSED SERS SUBSTRATES

In this chapter, the final SERS substrates performance is presented. An example of a typical Raman Spectra was presented in chapter 1. As a review, it consists of the vibrational frequencies of the molecules comprising a substance, as a shift from the excitation frequency. Figure 4–1 is an example of the Raman spectra of naphthalene. In the figure, the Rayleigh band corresponds to the frequency of the irradiation source, which acts as background in the signal and is filtered. The Stokes and anti-Stokes bands are also shown. Due to the higher signal intensity of the Stokes band, it is commonly used in the Raman Spectra. In the horizontal axis, the wavenumber (inverse of the wavelength) of the inelastically scattered light is presented, and is proportional to the difference in vibrational energy levels in a molecule. Figure 4–2 presents a Raman spectrum of 4-aminobenzoic acid (PABA) in solid state. Generally, a solid Raman spectrum of a

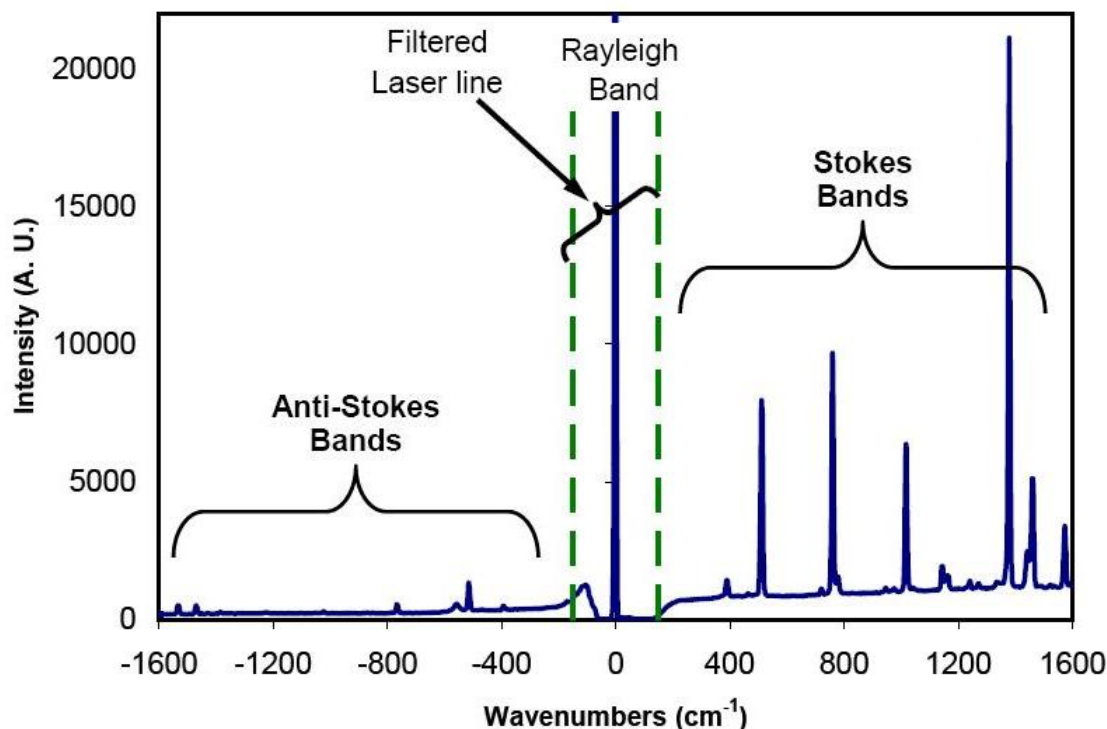


**Figure 4-1:** Rayleigh and Raman bands of solid naphthalene excited with a 632.8nm line [9].

substance will differ slightly from a SERS spectrum, with some vibrational modes appearing in one spectrum and not in the other, depending on the orientation of the molecule with respect to the SERS surface. Particularly for PABA, the  $980\text{cm}^{-1}$  band appearing in the SERS spectrum, does not appear in the solid Raman spectra. This band appears in the SERS spectrum due to an interaction between the PABA molecule and the silver deposited on the nanostructured SERS surface[43]. At the right side of figure 4-2 is shown a figure of the molecular structure of PABA. Also, since the molecule is not diluted in its solid state, the Raman signal is strong enough for detection and does not need enhancement. However, when the analyte is diluted in

an aqueous media, the normal Raman signal is very weak, and hence SERS becomes a strong tool for detection. This is why PABA as solid state was used as a reference point.

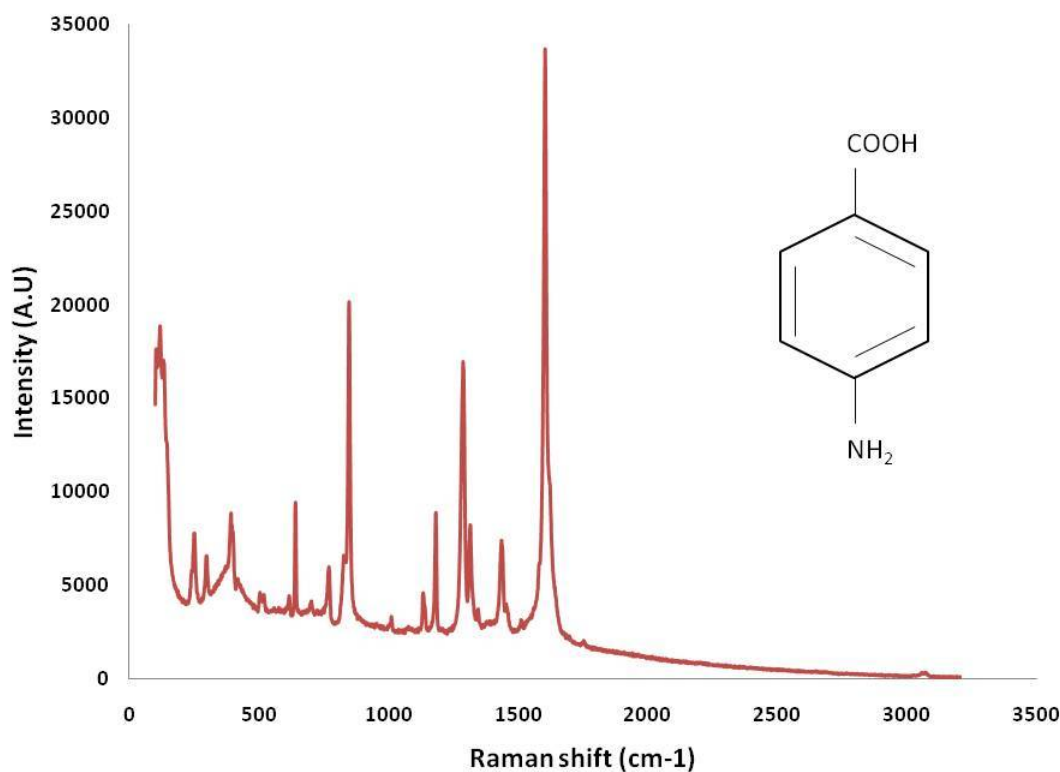


**Figure 4–2:** Raman spectrum of PABA in solid state. The inset shows the molecular structure of the substance.

#### 4.1 Materials and Methods

After the nanofabrication step, the polymer nanostructures were metalized by depositing a thin silver layer over the surface. An EDWARDS FL 400/AUTO 306 Physical Vapor Deposition (PVD) system was used to evaporate silver over the polymer composite to get the final SERS substrate. A  $1 \times 10^{-4}$ M solution of PABA prepared in deionized water was employed as the test analyte for the optimization

studies. The Raman spectra were obtained using a 2000 Renishaw Raman Microspectrometer equipped with a Leica microscope. The objective employed was a 10X lens, which allowed an incident power of 3.5 mW for the 785nm and 513nm excitation lines used. One acquisition of 10 seconds was collected by the charged coupled device detector. The spectral window ranged from 100–3200  $\text{cm}^{-1}$ .

The chip containing the nanofabricated arrays were carefully placed in the bottom of a small plastic dish where 3ml of PABA was added. Each nanoarray was then focused with the objective and centered to the incident laser beam. This was followed by the spectra collection.

#### **4.1.1 Thin Film Silver Evaporation**

In this step, the chips containing the polymer nanostructures were placed at the top of the deposition chamber and the target material (silver) was deposited over the chip surface. The deposition was achieved by heating the silver until its evaporation temperature at the chamber pressure was reached ( $1 \times 10^{-6}$  Torr). The instrument used to make the silver evaporation is shown in figure 4–3.



**Figure 4-3:** Picture of the EDWARDS FL 400/AUTO 306 Physical Vapor Deposition (PVD) system used to evaporate silver over the nanostructured polymer.

The deposition rate was  $5\text{\AA}/\text{s}$ . The Ag layer thickness deposited at the chips surface was varied from 15 to 45nm in 10nm interval. The Raman spectra were acquired with the different thickness, in order to determine the highest SERS intensity.

## 4.2 SERS Results

For the Raman spectra acquisition, arrays of hexagonal, square and elliptical nanopillars were used to test the nanostructured surface performance as SERS substrates. For each shape, the spectrum was acquired for the EBL dose that produced the patterns with the best geometrical definition, and minimum overexposed and underexposed areas (refer to Chapter 3 section 3.3), given by SEM inspection. For comparison purposes, the SERS spectrum was also acquired for patterns manufactured with lower EBL doses, which produce underexposed areas yielding ill-defined patterns. The spectrum was also

obtained with the different silver layer thickness. Only the 785nm excitation line gave SERS signal, indicating that the plasmon resonances of the composite metal/polymer nanopillars were near this wavelength value. To make the parametric study of the effect of shape and fabrication dose for the nanostructures and the influence of the different deposited silver layer thickness, the magnitude of the  $411\text{cm}^{-1}$  band present in the PABA spectrum was chosen. The reason this band was chosen is due to the high chemical stability that this band represents, not being exposed to photolytic changes induced by the LASER irradiation[44]. The following sections explain the results obtained for each individual nanopillar shape. The effect of different dose is presented at each deposited silver layer thickness for the different nanopillars geometry.

#### 4.2.1 Study with Hexagonal Patterns

Figure 4–4 presents a comparison of the Raman spectra intensity of PABA using the hexagons array, fabricated with an EBL dose of 0.45, 0.35, and 0.3 nC/cm and with a silver layer thickness of 15nm. Silver layers thickness greater than 15nm did not give SERS signal for the hexagons. It is assumed that above 15nm the silver coating thickness begins to cover the gap between the patterns, giving a semi-continuous film that reduces the SERS signal intensity. From the observation of figure 4–4, it is clear that the signal intensity is higher at a dose of

0.45 nC/cm (best well-defined pattern) and is reduced when the dose is lower than 0.45nC/cm. The signal intensity at a dose of 0.35 and 0.3 nC/cm is reduced by 16% and 80% respectively, with respect to the one obtained at 0.45 nC/cm. Figure 4–5 and 4–6 show the Raman

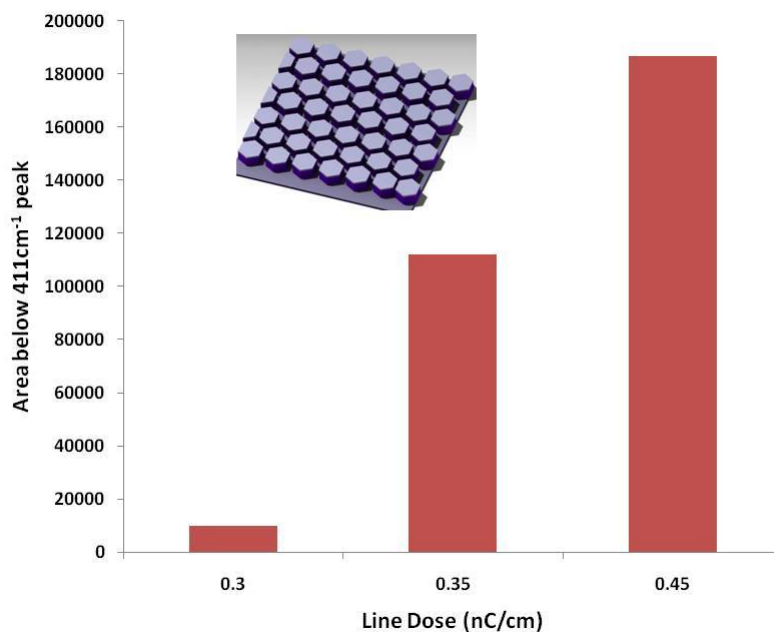


**Figure 4–4:** Effect of the dose used for the hexagonal pattern fabrication on the 411cm<sup>-1</sup> band signal of PABA (1X10<sup>-4</sup>M). The silver layer thickness corresponding to these intensities is 15nm.

spectra of PABA, with a dose of 0.45 and 0.35nC/cm respectively, both with a silver layer thickness of 15nm. The signal obtained with the fabricated nanostructures at the dose of 0.45nC/cm is clearly stronger than the one obtained with the lower fabrication dose.

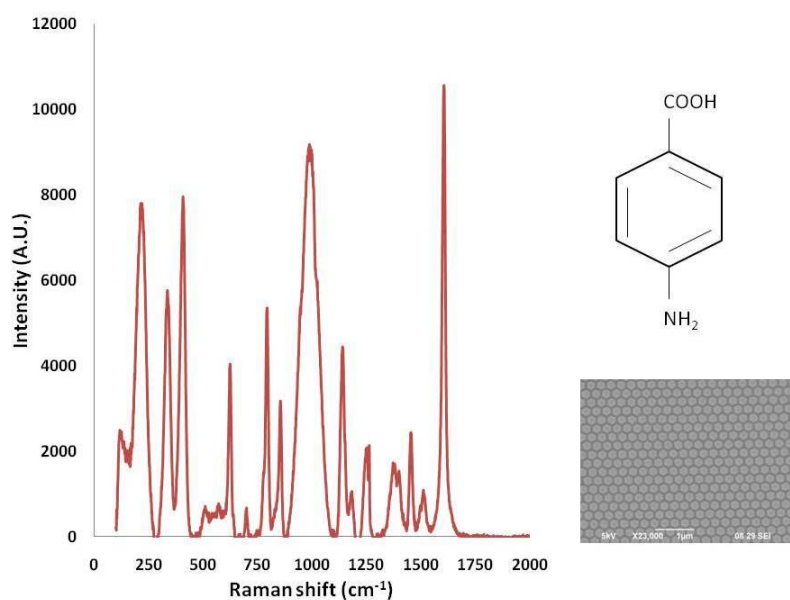


**Figure 4-5:** Raman spectra of PABA acquired using the Hexagons array fabricated with a dose of 0.45nC/cm. The excitation line used was 785nm with a silver layer thickness of 15nm.

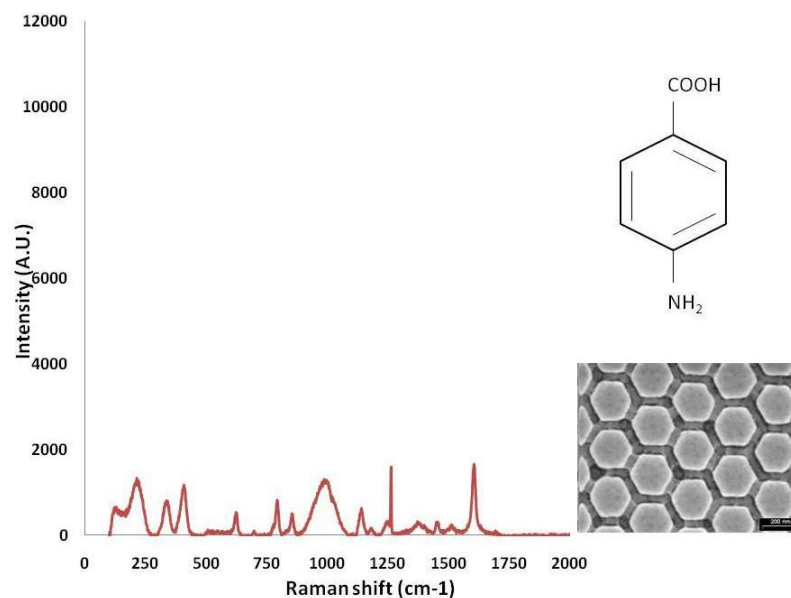


**Figure 4-6:** Raman spectra of PABA acquired using the Hexagons array fabricated with a dose of 0.35nC/cm . The excitation line used was 785nm with a silver layer thickness of 15nm.

### 4.2.2 Study with Square Patterns

Figure 4–7 shows the comparison of the Raman spectra intensity of PABA using the square patterns, fabricated with a dose of 0.5, 0.45, and 0.4nC/cm, with a silver layer thickness of 15nm. This figure shows that the maximum intensity occurs with the squares fabricated with the dose of 0.5nC/cm, at which the squares had the best definition. At the fabrication dose of 0.45nC/cm, the SERS intensity decayed by 46%, while for a dose of 0.4nC/cm there was no SERS signal. Figure 4–8 shows the SERS intensities of the patterns with a silver layer thickness of 25nm. In this case, the only pattern that gave SERS signal was the one fabricated with a dose of 0.5nC/cm. The other two doses for pattern fabrication did not show a SERS response at 25nm of thickness.

From figures 4–7 and 4–8 it can be observed that at an EBL dose of 0.5 nC/cm the SERS signal intensity with a deposited silver layer of 25nm is reduced by a 94% with respect to the one obtained with a silver layer thickness of 15nm. For silver layer thickness of 35 and 45nm no SERS signal was obtained. Although there was SERS signal for squares at a silver layer thickness of 25nm, this was severely reduced compared with the one obtained at a silver layer thickness of 25nm. The same situation assumed for the hexagons, for which there was not SERS signal with silver layer thickness above 15nm is expected

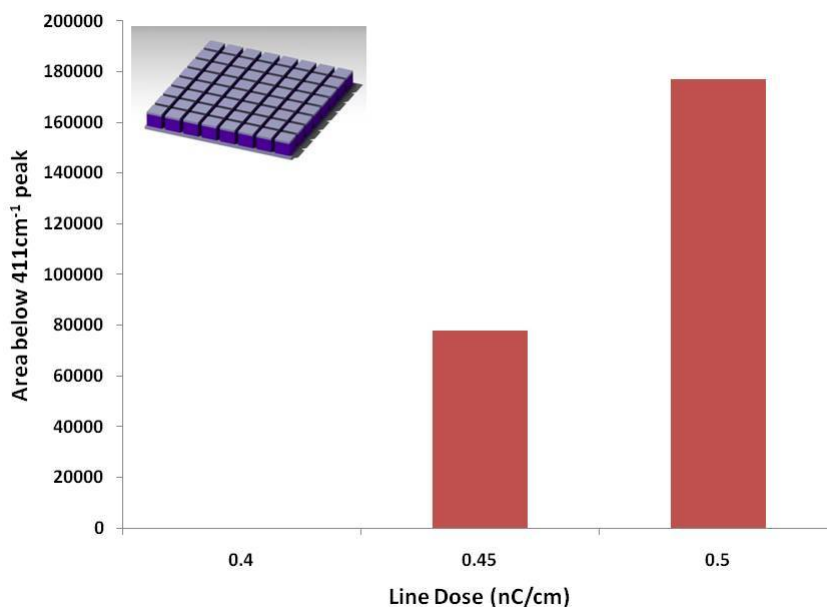


**Figure 4-7:** Effect of the dose used for the square pattern fabrication on the  $411\text{cm}^{-1}$  band signal of PABA ( $1 \times 10^{-4}\text{M}$ ). The silver layer thickness corresponding to these intensities is 15nm.

to be occurring with the squares. Hence the increase in silver layer thickness above 15nm may be creating a semi-continuous film that is screwing up the nanopillars discontinuities (gap between features), decreasing the SERS enhancement mechanism. The SERS spectra of PABA using squares nanostructures as the active surface are shown in figures 4-9 and 4-10. The squares nanostructures in figures 4-9 are fabricated with a dose of  $0.5\text{nC/cm}$ , while a dose of  $0.45\text{nC/cm}$  was used for the structures of figure 4-10. Figure 4-11 presents the Raman spectrum using the squares nanostructures with a deposited silver layer thickness of 25nm. As can be seen, the signal intensity is considerably reduced with respect to the nanostructures with a 15nm of silver layer.

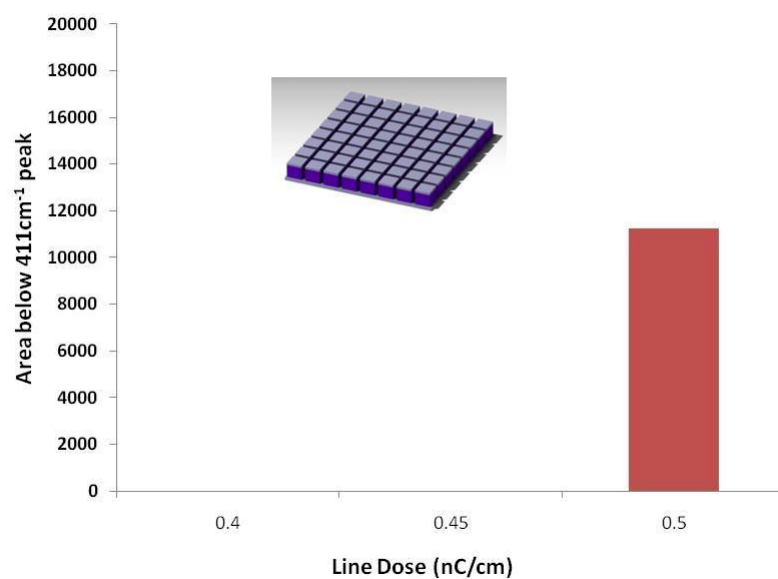


**Figure 4–8:** Effect of the dose used for the square pattern fabrication on the 411cm<sup>-1</sup> band signal of PABA (1X10<sup>-4</sup>M). The silver layer thickness corresponding to these intensities is 25nm.

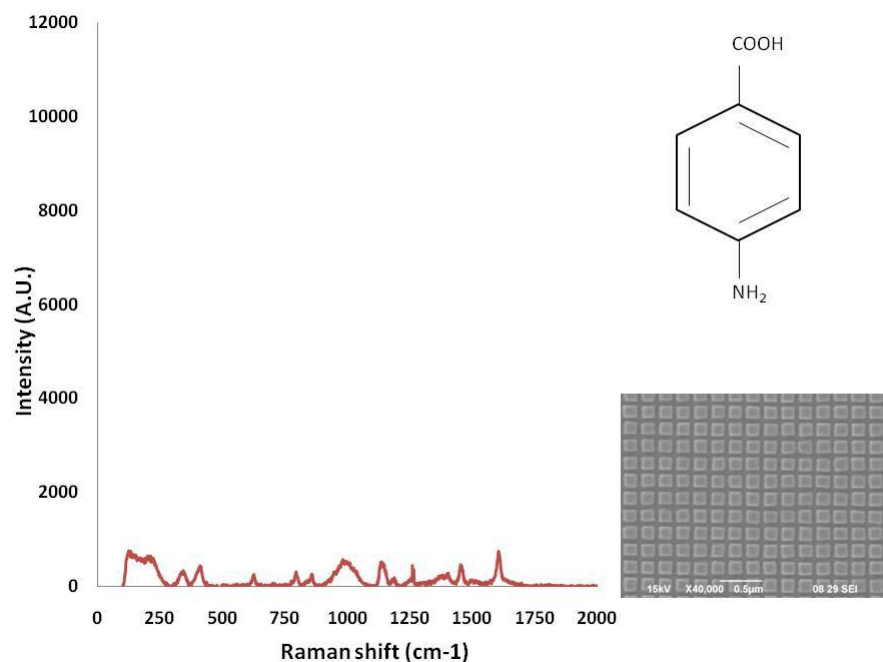


**Figure 4–11:** Raman spectra of PABA acquired using the Squares array fabricated with a dose of 0.5nC/cm . The excitation line used was 785nm with a silver layer thickness of 25nm.

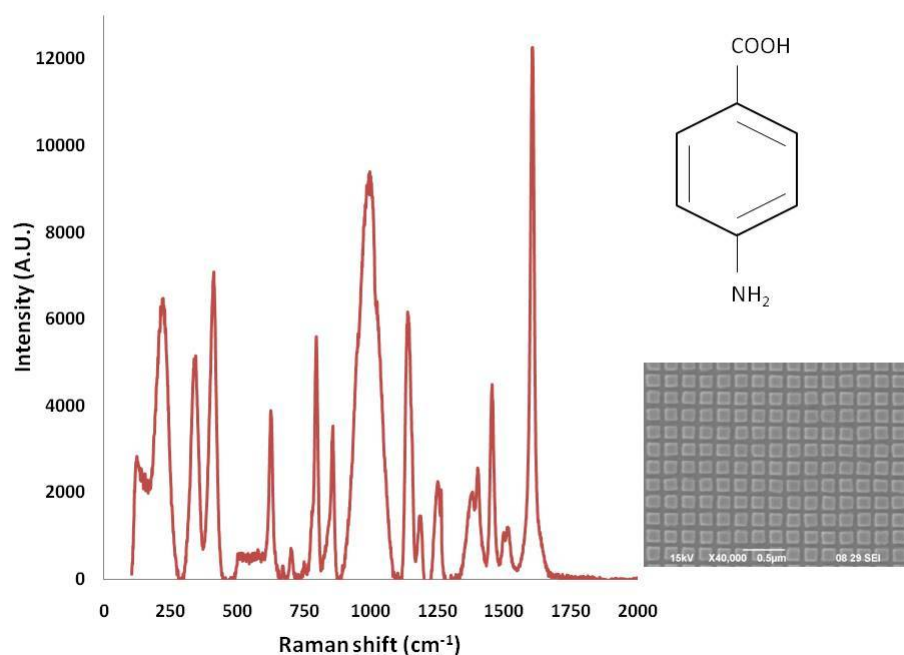


**Figure 4–9:** Raman spectra of PABA acquired using the Squares array fabricated with a dose of 0.5nC/cm . The excitation line used was 785nm with a silver layer thickness of 15nm.

### 4.2.3 Study with Elliptical Patterns

Figures 4–12 to 4–14 illustrate the effect of dose and deposited layer thickness on the elliptical nanostructures. The fabrication dose for the elliptical pattern that gave the highest SERS signal was the dose that produced the nanostructures with the best geometrical definition. This result is consistent with those that were previously obtained for the hexagonal and square patterns.

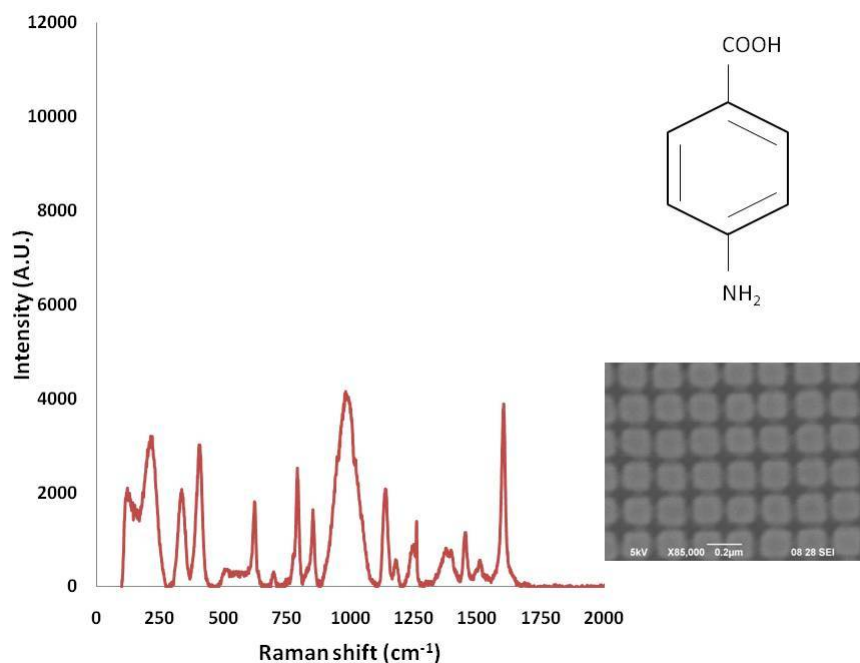


**Figure 4–10:** Raman spectra of PABA acquired using the Squares array fabricated with a dose of  $0.45\text{nC}/\text{cm}$ . The excitation line used was  $785\text{nm}$  with a silver layer thickness of  $15\text{nm}$ .

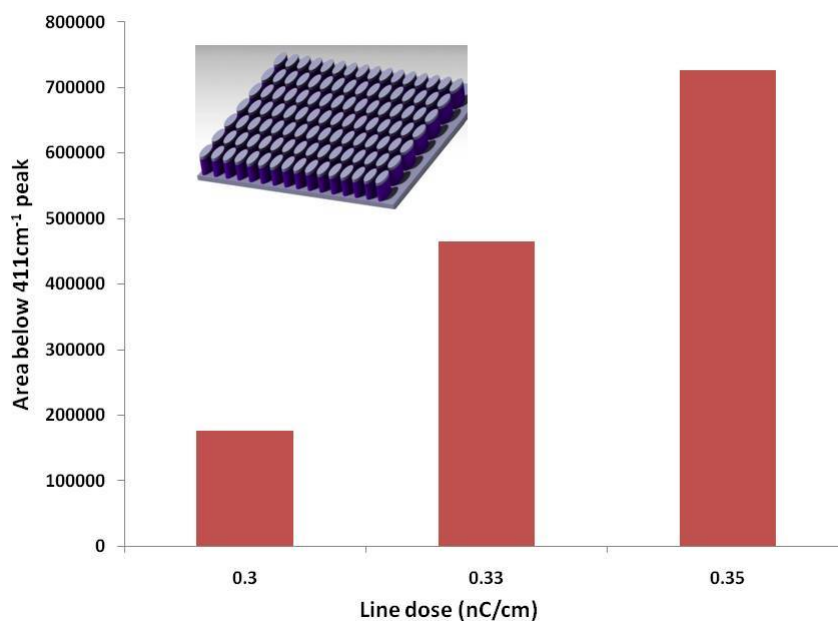


**Figure 4–12:** Effect of the dose used for the elliptical pattern fabrication on the  $411\text{cm}^{-1}$  band signal of PABA ( $1 \times 10^{-4}\text{M}$ ). The silver layer thickness corresponding to these intensities is  $15\text{nm}$ .

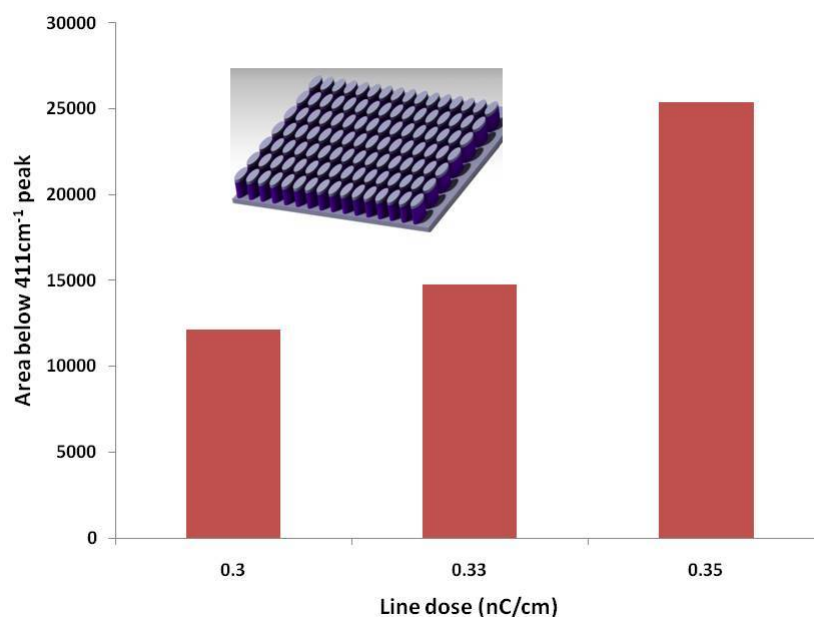


**Figure 4–13:** Effect of the dose used for the elliptical pattern fabrication on the  $411\text{cm}^{-1}$  band signal of PABA ( $1 \times 10^{-4}\text{M}$ ). The silver layer thickness corresponding to these intensities is 25nm.

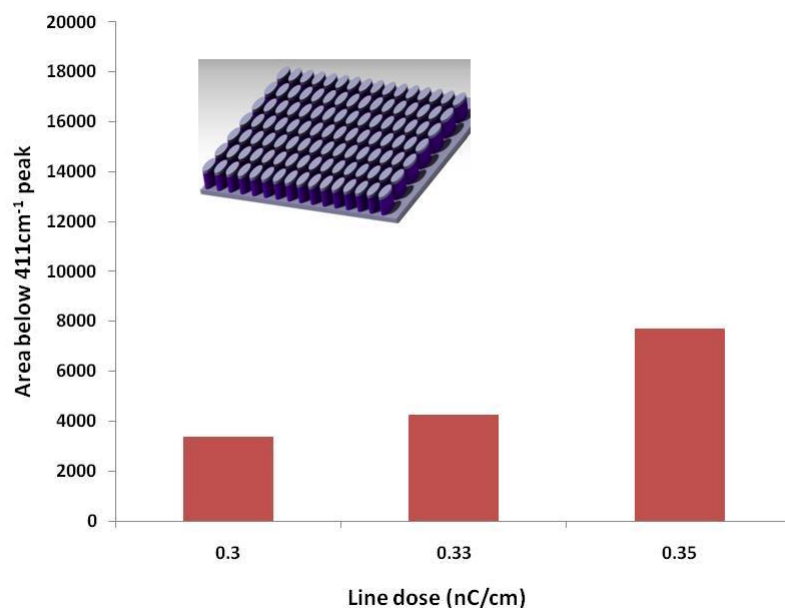


**Figure 4–14:** Effect of the dose used for the elliptical pattern fabrication on the  $411\text{cm}^{-1}$  band signal of PABA ( $1 \times 10^{-4}\text{M}$ ). The silver layer thickness corresponding to these intensities is 35nm.

The signal corresponding to a silver layer thickness of 15nm was the highest in the interval. Figure 4–15 shows the trend of the SERS

signal intensity with the ellipses fabricated at a dose of  $0.35\text{nC/cm}$ , varying the silver layer thickness. The vertical axis represents the percentage of the maximum intensity of the  $411\text{cm}^{-1}$  band present in PABA with respect to the silver layer thickness. The figure indicates that the maximum enhancement of the signal is obtained when the thickness is  $15\text{nm}$ , and drops sharply with a  $25\text{nm}$  of silver coating. Then, when going from  $25$ ,  $35$  and  $45\text{nm}$  of silver coating, the SERS signal decayed gradually. Figures 4–16 and 4–17 show the acquired PABA SERS spectra with a silver deposited layer thickness of  $15$  and  $25\text{nm}$  respectively.

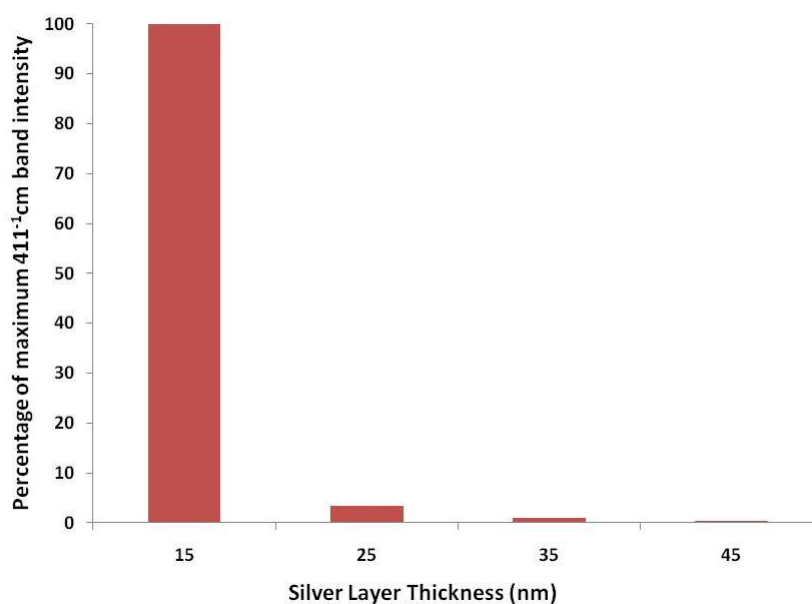


**Figure 4–15:** Influence of the deposited layer thickness over the elliptical nanostructures on the SERS intensity of the  $411\text{cm}^{-1}$  present in PABA.

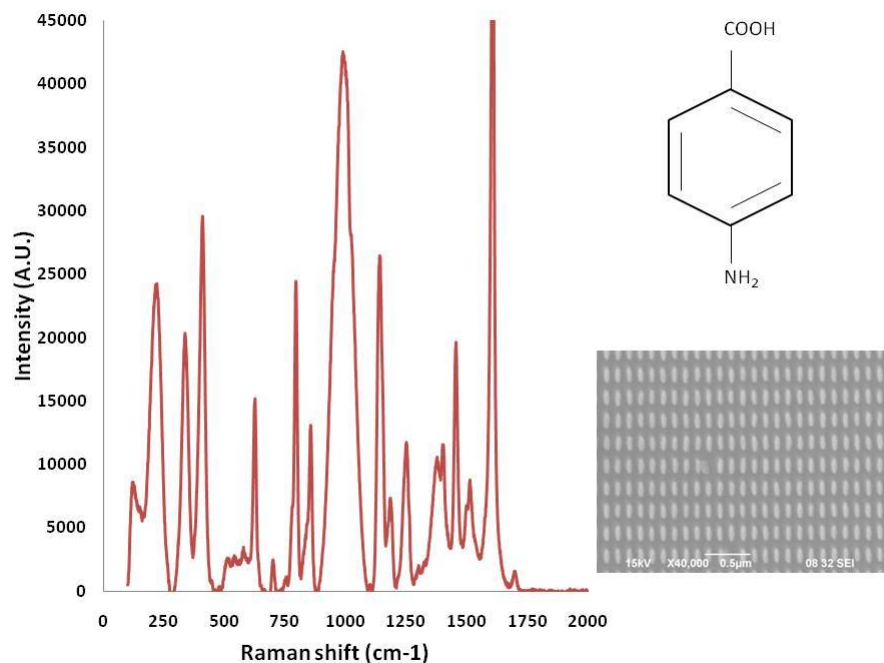


**Figure 4–16:** Raman spectra of PABA acquired using the elliptical array fabricated with a dose of 0.35nC/cm . The excitation line used was 785nm with a silver layer thickness of 15nm.

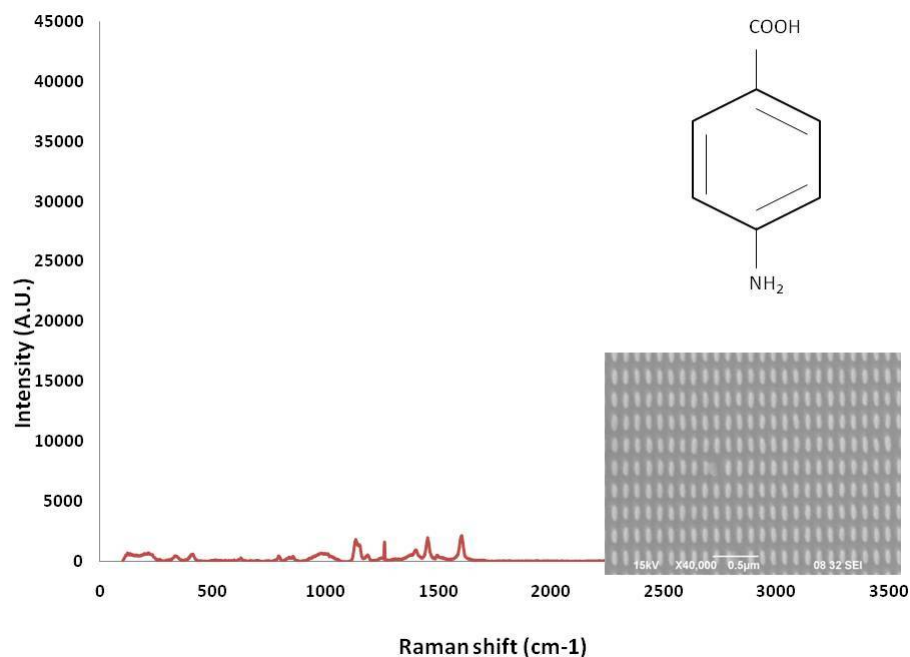


**Figure 4–17:** Raman spectra of PABA acquired using the elliptical array fabricated with a dose of 0.35nC/cm . The excitation line used was 785nm with a silver layer thickness of 25nm.

#### 4.2.4 Nanostructures Shape Comparison

The evaluation of the influence of the nanoparticle shape parameter in the strength of the generated SERS signal is shown in figure 4-18. This figure compares the percentage of maximum SERS spectrum intensity obtained for PABA  $1 \times 10^{-4} \text{M}$  with a deposited layer thickness of 15nm over surfaces versus the shape of the nanostructures. The percentage is taken with respect to the highest signal obtained, which was given by the elliptical nanostructures at 15nm. The values of the signal of squares and hexagons were extracted from sections 4.2.1 and 4.2.2, using the most intense signal obtained with a silver thickness of 15nm. The figure indicates that the maximum signal strength is obtained with the elliptical nanostructures for the excitation line of 785nm.

### 4.3 Discussion

The evaluation of the influence of the EBL fabrication dose on the SERS signal intensity for each nanostructure shape at different silver coating thickness shows that an effective nanofabrication procedure is crucial to achieve the maximum SERS intensity. The effect of the silver deposition over the incompletely developed PMMA (facilitating the creation of a continuous conductive film) combined with the lack of shape definition of the patterns (which attenuates the effect of localized surface Plasmon resonances) is the most probable reason of

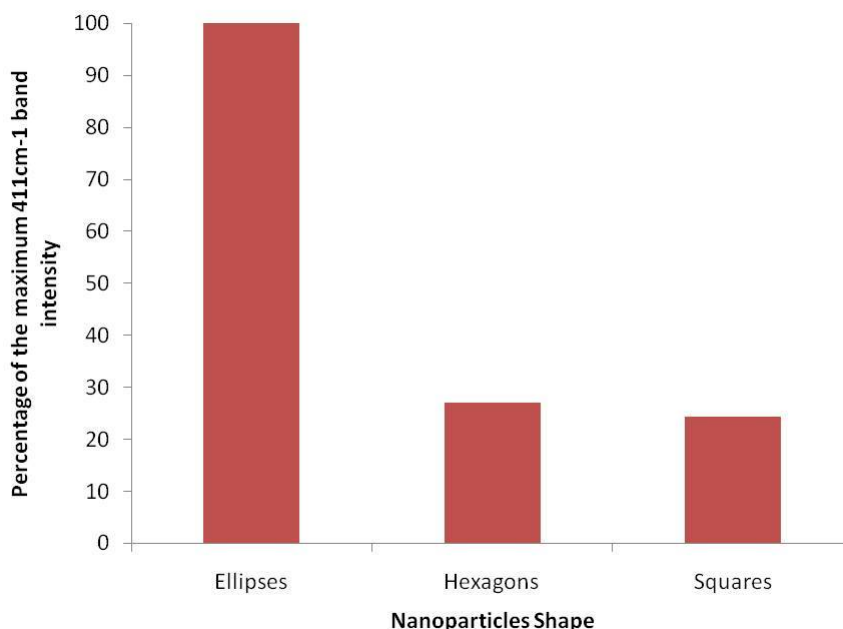


**Figure 4–18:** Influence of the nanostructures shape on the SERS intensity of the  $411\text{cm}^{-1}$  present in PABA. The silver layer thickness is 15nm.

the drastically reduced SERS signal obtained by the nanopillars fabricated with doses below the threshold required to achieve well-defined patterns.

On the other hand, if the deposition of silver was completely directional, even with a silver layer thickness of 45nm (maximum deposited thicknesses in the range), a strong SERS signal should be obtained. The reason for this to occur is because the height of the nanopillars (fabricated with the correct dose) is about 200nm, which should prevent the creation of a continuous metallic layer. However, although the silver deposition is directional for the most part, some shadow effect occurs, which tends to reduce the gap between the patterns.

This situation is beneficial to some extent, because it increases the active plasmonic surface area and it might induce interpillar coupling effect, thus enhancing the effective plasmon resonance. However, further increase in the thickness of the silver coating eventually causes the pillars to touch each other, creating a semi-continuous layer that attenuates the SERS effect. This would explain the abrupt decrease of SERS signal obtained for square and elliptical nanopillars, when changing from a silver coating thickness of 15nm to 25nm. The signal decreases even further with increasing coating thickness. This effect might have caused the lack of SERS signal for hexagonal nanopillars with silver layer coatings greater than 15nm.

Finally, graph 4-18 clearly indicates that the geometry plays an important role in the mechanism of SERS. From the figure, it is deduced that changing the nanostructures shape from square and hexagonal to elliptical, the SERS signal increased by 410 and 370% respectively, using a 785nm excitation line. Obviously, being SERS a mechanism dependent on the excitation line wavelength, we may obtain a higher signal for other geometries at a different excitation line frequency.

## CHAPTER 5

# CONCLUSIONS AND FUTURE WORKS

### 5.1 Conclusions

From the study elaborated in the previous chapter the following conclusions can be drawn:

- The nanofabrication process using EBL to produce the SERS substrates proved to be effective, allowing control over the desired shape, size, and interparticle spacing. The nanofabrication parameters were obtained, varying baking and developing time, base dose, and number of resist layers.
- The nanofabricated substrates gave intense Raman signal, which demonstrates the importance of nanofabrication processes to produce highly reproducible and effective nanostructures for SERS. EBL in particular promises to continue being an effective way to produce surfaces with unique properties, which represents superior response for SERS.
- The thickness of the deposited silver layer played a relevant role in the final SERS substrate performance. For thickness larger than 15nm, the signal began to flag considerably.

- The 785nm wavelength radiation source showed to be near the resonance of the surface plasmons of the nanostructures. This result was in accordance with the fact that at increasing the nanoparticles size, the wavelength of the source that effectively excites the surface Plasmon is red shifted.
- From the tested nanostructures, the ellipses gave the most intense signal, indicating that they were better for the 785nm excitation line.

## 5.2 Future Work

For future work, the performance of different produce shapes will be tested as SERS substrates. Some of them are showed in figures 5-1 to 5-3 . Figures 5-2 and 5-3 illustrate nanostructures that will encounter relevant importance in system were the sample is allowed to rotate. This would give a strong SERS signal, taking into account that in certain moment all the particles major symmetry axis will be parallel to the electric field component of the exciting light, which is known to be the configuration most favorable for a more intense Raman signal.

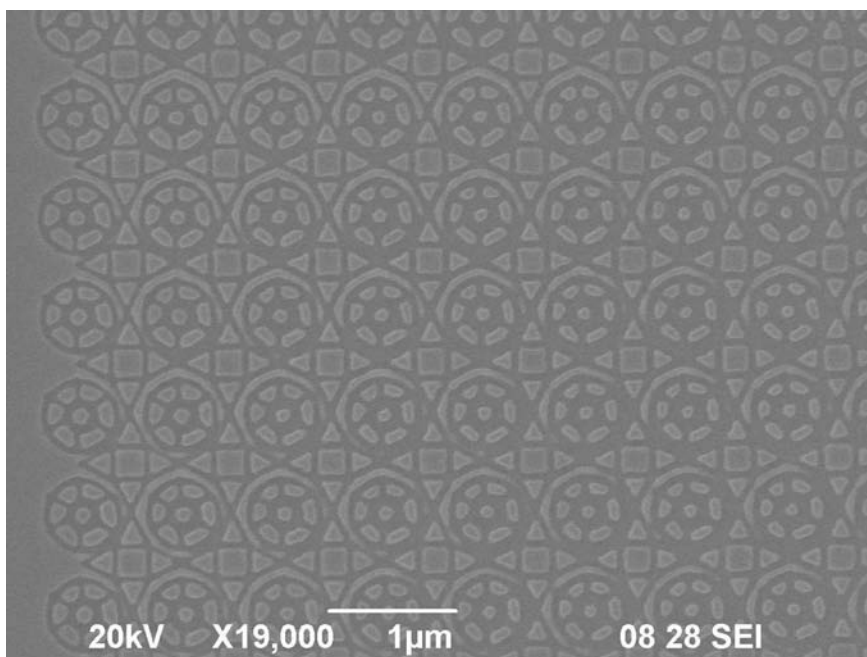


**Figure 5–1:** Nanostructures with triangles and cluster like particles configuration

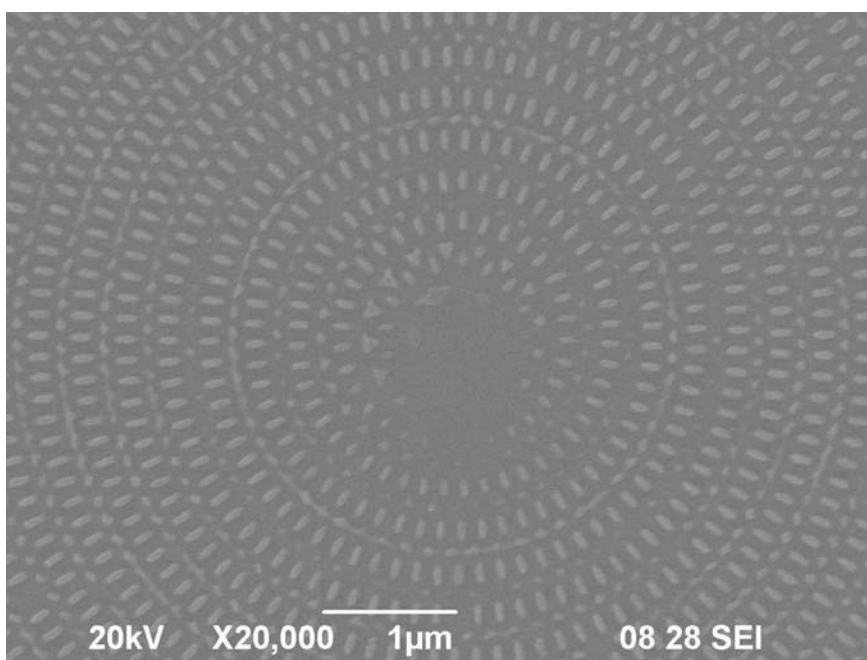


**Figure 5–2:** Ellipses arrange in a circular array

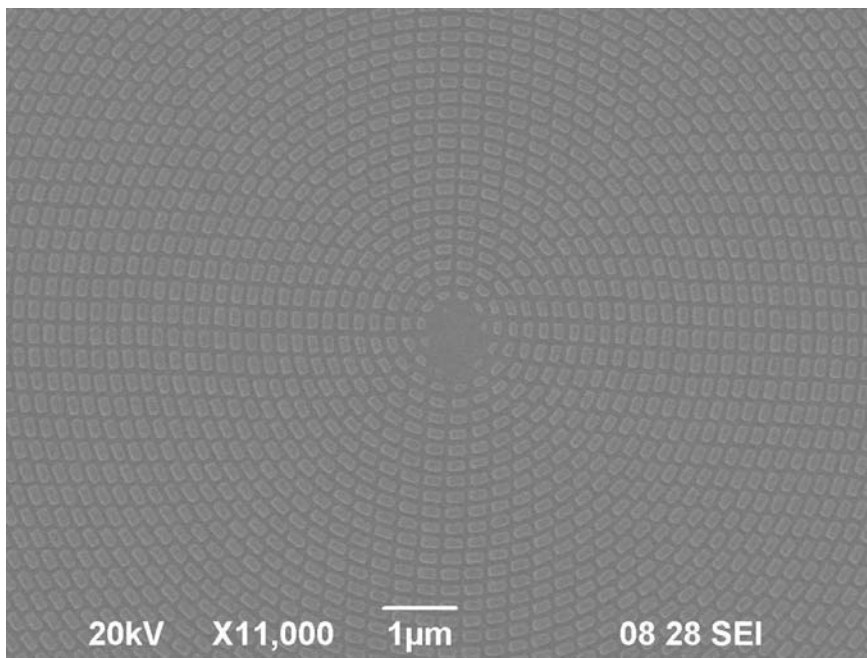


**Figure 5–3:** Rectangles arranged in a circular array

## REFERENCE LIST

- [1] C.V. Raman. A change of wave-length in light scattering. *Nature*, 121:619, 1928.
- [2] K. Kelly; E. Coronado; L. Zhao and G. Schatz. The optical properties of metal nanoparticles: The influence of size, shape and dielectric environment. *J. Phys. Chem*, 107 B:668–677, 2003.
- [3] K. Kneipp; H. Kneipp; I. Itzkan; R. Dasari and M. Feld. Surface enhanced raman scattering and biophysics. *J. Phys. Condens. Matter*, 14:597–624, 2002.
- [4] Xu H.X.; Aizpurua J; Kall M and Apell P. Electromagnetic contributions to single-molecule sensitivity in surface enhanced raman scattering. *Phys. Rev. E*, 62:4318–4324, 2000.
- [5] F. J. Garcia-Vidal and J. B. Pendry. Collective theory for surface enhanced raman scattering. *Phys. Rev. Lett.*, 77, 7:1163–1166, 1996.
- [6] A. Otto. Light scattering in solids iv. *App. Phys*, 54, Springer-Verlag, Berlin, 1984.
- [7] M. Moskovits. Surface roughness and the enhanced intensity of raman scattering by molecules absorbed on metals. *J. Chem. Phys.*, 69:4159, 1978.
- [8] Long Derek A. *The Raman Effect: A unified treatment of the theory of Raman scattering by molecules*. John Wiley & Sons. Ink; NY, 2002.
- [9] M. A. De Jesús. Development of novel substrates and sampling techniques for the analysis of drugs and model environmental pollutants via surface enhanced raman spectroscopy (sers). *Doctor of Philosophy thesis, University of Tennessee, Knoxville*, 2004.

- [10] J. R. Ferraro; Kazuo Nakamoto; and Chris W. Brown. *Introductory Raman Spectroscopy*. Elsevier, second edition, 2003.
- [11] X. Zhang; C.R. Yonzon; M.A. Young; D.A. Stuart and R.P. Van Duyne. Surface-enhanced raman spectroscopy biosensors: excitation spectroscopy for optimisation of substrates fabricated by nanosphere lithography. *IEE Proc. Nanobiotechnol.*, 152, No 6:195–206, 2005.
- [12] Skoog D. A.; Hooler F. J.; Nieman T. *Principles of Instrumental Analysis*. Saunders College Publishing, 1998.
- [13] M. Fleischmann; P.J. Hendra and A.J.Mcquillan. Raman spectra of pyridine absorbed at a silver electrode. *Chem. Phys.lett.*, 26:163–166, 1974.
- [14] Jeanmaire D. L.; Van Duyne R. P. Surface raman spectroelectrochemistry. part i. heterocyclic, aromatic, and aliphatic amines adsorbed on the anodized silver electrode. *J. Electroanal. Chem.*, 84 (1):1–20, 1977.
- [15] H. D. Ladouceur; D. E. Tevault; R. R. Smardzewski. Surface-enhanced raman scattering from vapor-deposited copper, silver, and gold. excitation profiles and temperature dependence. *J. Chem. Phys.*, 78:980, 1983.
- [16] M. Moskovits. Surface-enhanced spectroscopy. *Rev. Mod. Phys.*, 57:783–826, 985.
- [17] Xu H.X.; Kall M. Polarization-dependent surface-enhanced raman spectroscopy of isolated silver nanoaggregates. *Chem. Phys. Chem.*, 4:1001, 2003.
- [18] E. Hao and G. Schatz. electromagnetic fields around silver nanoparticles and dimers. *J. Chem. Phys.*, 120:357–366, 2003.
- [19] Norrod K. L.; Sudnik L. M.; Rousell D. ; Rowlen K. L. Quantitative comparison of five sers substrates: sensitivity and limit of detection. *Applied Spectroscopy*, 51(7):994–1001, 1997.
- [20] Vo-Dinh T. Surface-enhanced raman spectroscopy using metallic nanostructures. *TrAC, Trends in Analytical Chemistry*, 17:557–582, 1998.

- [21] McQuillan A. J.; Hendra P. J.; Fleischmann M. Raman spectroscopic investigation of silver electrodes. *Journal of Electroanalytical Chemistry and Interfacial Electrochemistry*, 65(2):933, 1997.
- [22] Ibrecht M. G.; Creighton J. A. Intense raman spectra at a roughened silver electrode. *Electrochimica Acta*, 23(10):1103, 1978.
- [23] Keir R.; Sadler D.; Smith W. E. preparation of stable, reproducible silver colloids for use as surface-enhanced resonance raman scattering substrates. *Applied Spectroscopy*, 56(5):551–559, 2002.
- [24] Tran C. D. Subnanogram detection of dyes on filter paper by surface-enhanced raman scattering spectrometry. *Analytical Chemistry*, 56(4):824, 1984.
- [25] Bello J. M.; Stokes D. L.; Vo-Dinh T. Titanium dioxide based substrate for optical monitors in surface-enhanced raman scattering analysis. *Analytical Chemistry*, 61(15):1779–1783, 1989.
- [26] Alak A. M.; Vo-Dinh T. Silver-coated fumed silica as a substrate material for surface-enhanced raman scattering. *Analytical Chemistry*, 61(7):656–660, 1989.
- [27] Meier M.; Wokaun A.; Vo-Dinh T. Silver particles on stochastic quartz substrates providing tenfold increase in raman enhancement. *Journal of Physical Chemistry*, 89(10):143–146, 1985.
- [28] Vo-Dinh T.; Meier M.; Wokaun A. Surface-enhanced raman spectrometry with silver particles on stochastic-post substrates. *Analytica Chimica Acta*, 181:139–148, 1986.
- [29] Zhang X.; Hicks E. M.; Zhao J.; Schatz G. C.; Van Duyne R. P. Electrochemical tuning of silver nanoparticles fabricated by nanosphere lithography. *Nano Lett.*, 5(7):1503–1507, 2005.
- [30] Haynes C. L.; Van Duyne R. P. Nanosphere lithography: A versatile nanofabrication tool for studies of size-dependent nanoparticle optics. *J. Phys. Chem.*, 105(24):5599–5611, 2001.

- [31] E.; Kostrewa S.; Viets C.; Hill W. Kahl M.; Voges. Periodically structured metallic substrates for sers. *Sens. Actuators, B: Chem.*, B51, (1-3):285–291, 1998.
- [32] Sackmann M.; Bom S.; Balster T.; Materny A. Nanostructured gold surfaces as reproducible substrates for surface-enhanced raman spectroscopy. *J. Raman Spectroscopy*, 38(3):277–282, 2007.
- [33] Hicks E. M.; Zou S.; Schatz G. C.; Spears K. G.; Van Duyne R. P.; Gunnarsson L.; Rindzevicius T.; Kasemo B.; Kaell M. Controlling plasmon line shapes through diffractive coupling in linear arrays of cylindrical nanoparticles fabricated by electron beam lithography. *Nano Lett.*, 5(6):1065–1070., 2005.
- [34] De Jesus; K. Giesfeldt; J. Oran; N. Abu-Hatab; N. Lavrik; and M. Spaniak. Nanofabrication of densely packed metal-polymer arrays for surface-enhanced raman spectrometry. *App. Spectrosc.*, 52:1501, 2005.
- [35] Marc J. Madou. *Fundamentals of Microfabrication*. CRC, second edition, 2002.
- [36] H. I. Smith. 100 years of x-rays: impact on micro and naofabrication. *J. Vac. Sci. and Techn.*, B13:2323, 1995.
- [37] P. Rai-Choudhury. *Handbook of microlithography, micromachining, and micro-fabrication volume 1*. SPIE, 1997.
- [38] Gemma Rius Su né. Electron beam lithography for nanofabrication. *Doctor of Philosophy thesis, Universidad Autónoma de Barcelona*, 2008.
- [39] Ampere A Tseng. *Nanofabrication Fundamentals and Applications*. World Scientific, 2008.
- [40] M. Parikh. Self-consistent proximity effect correction technique for resist exposure (spectre). *J. Vac. Sci. and Techn.*, 15:931–933, 1978.
- [41] Weilie Zhou and Zhong Lin Wang. *Scanning Microscopy for Nanotechnology*. Springer, 2006.

- [42] M. Hatzakis. Electron resists for microcircuit and mask production. *J. Electrochem. Soc.*, 116:1033–1037, 1969.
- [43] Jung Sang Suh and Jurae Kim. Three distinct geometries of surface-adsorbed carboxylate groups. *J. Raman Spectroscopy*, 29:143–148, 1998.
- [44] M. A. De Jesus; K. S. Giesfeldt and M. J. Sepaniak. Improving the analytical figures of merit of sers for the analysis of model environmental pollutants. *J. Raman Spectroscopy*, 35:895–904, 2004.